Title
Embedded Sensing and Computing Technologies for Wireless Health

Author
Xu, Wenyao

Publication Date
2013

Peer reviewed|Thesis/dissertation

UNIVERSITY OF CALIFORNIA

Los Angeles

Embedded Sensing and Computing Technologies for Wireless Health

A dissertation submitted in partial satisfaction

of the requirements for the degree

Doctor of Philosophy in Electrical Engineering

by

Wenyao Xu

2013

ABSTRACT OF THE DISSERTATION

Embedded Sensing and Computing Technologies for Wireless Health

by

Wenyao Xu

Doctor of Philosophy in Electrical Engineering

University of California, Los Angeles, 2013

Professor Majid Sarrafzadeh, Co-chair

Professor Lei He, Co-chair

Solving healthcare related problems is one of the grand challenges in the 21st century. In many nations, the need to improve existing medical and healthcare services is becoming increasingly important due primarily to the growing population and ageing society. The rapid advancement of sensors, computing and wireless communication technology has brought rise to a new research field called Wireless Health, which transforms health related services from the system based on episodic examination, disease diagnosis and treatment to one with continuous monitoring, disease prediction and prevention.

In this thesis, I will summarize the projects in the Wireless Health research. They consist of different critical healthcare applications, from pressure ulcer prevention and gait analysis to non-contact cardiopulmonary monitoring and remote rehabilitation. Each project is conducted and presented in an end-to-end manner, including identifying medical problems, proposing solutions, developing systems and clinical verification. As for the technology development part, a few novel embedded sensing and computing technologies, including sensor system design, sensor modeling and sensor signal processing, will be discussed. The ultimate goal of this interdisciplinary research is to proof the medical hypothesis, verify the feasibility of technological solutions in clinics, and finally enable Wireless Health from concept to practice.

The dissertation of Wenyao Xu is approved.

Jens Palsberg

William Kaiser

Lei He, Committee Co-chair

Majid Sarrafzadeh, Committee Co-chair

University of California, Los Angeles

2013

To my beloved family and friends.

TABLE OF CONTENTS

LIST OF FIGURES

LIST OF TABLES

ACKNOWLEDGMENTS

First, I would like to sincerely thank my co-advisors, Professor Majid Sarrafzadeh and Professor Lei He, for all the support and guidance. They have been giving me through the entire study. I learned a lot not only from their words but also from the good examples that they set with their diligence, passion and preciseness in research, all of which deeply influence me. Their tirelessness in giving helpful advice, sharing with me their knowledge and brilliant ideas, along with their friendliness and sense of humors truly inspire my enthusiasm and make this study a enjoyable experience. There is no way I would have done this work without their help and support.

I am also very grateful to Professor William Kaiser and Professor Jens Palsberg for being on my thesis committee and providing useful comments, which have helped a lot in revising the thesis.

In addition, I would like to thank our group members for their help on various aspects. I wish to thank Ming-Chun Huang, Jasson J. Liu, Nabil Alshurafa and Navid Amini, for for sharing their ideas and useful tools with me. It is an unforgotten memory to work with you guys. Fruitful discussions with other group members during group meetings are also greatly appreciated. My acknowledgements also go to my friend Fengbo Ren for his thoughtful comments and suggestions on this thesis.

Last, I wish to express my measureless gratitude towards my parents, Weifan Xu and Enxiu Wang, for their never-ending giving and loving. I also want to give great thanks to my lovely Sichen and Austin. Your appearance makes this long journey full of fun and happiness.

VITA

2006 B.S. (Electrical Engineering), Zhejiang University, China.

2008 M.S. (Electrical Engineering), Zhejiang University, China.

PUBLICATIONS

Wenyao Xu, Ming-Chun Huang, Navid Amini, Lei He, Majid Sarrafzadeh, "*eCushion: A Textile Pressure Sensor Array Design and Calibration for Sitting Posture Analysis*", IEEE Sensors Journal (**SJ**), 2013

Xinmin Xu, Yao Chen, **Wenyao Xu**, Fang Gong, "*An Efficient Algorithm for Mobile Localization in Sensor Networks*", International Journal of Automation and Computing (**IJAC**), Volume 9, Number 6, December 2012, Pages 594 - 599.

Wenyao Xu, Mi Zhang, Alexander A. Sawchuk, Majid Sarrafzadeh, "*Robust Human Activity and Sensor Location Co-Recognition via Sparse Signal Representation*", IEEE Transactions on Biomedical Engineering (**TBME**), Volume 59, Issue 11, November 2012, Pages 3169 - 3176.

Wenyao Xu, Changzhan Gu, Changzhi Li, Majid Sarrafazadeh, "*Robust Doppler Radar Demodulation via Compressed Sensing*", IET Electronics Letters (**EL**), Volume 48, Number 23, October 2012, Pages 1428 - 1430.

Lerong Cheng, Fang Gong, **Wenyao Xu**, Jinjun Xiong, Lei He, Majid Sarrafzadeh, "*Fourier Series Approximation for Max Operation in Non-Gaussian and Quadratic Statistical Static Timing Analysis*", IEEE Transactions on Very Large Scale Integration Systems (**TVLSI**), Volume 20, Issue 8, August 2012, Pages 1383 - 1391.

Lerong Cheng, **Wenyao Xu**, Fang Gong, Yan Lin, Lei He, "*Statistical Timing and Power Optimization of Architecture and Device for FPGAs*", ACM Transactions on Reconfigurable Technology and Systems (**TRTS**), Volume 5, Issue 2, Number 9, June 2012.

Fang Gong, **Wenyao Xu**, Ju-Yueh Lee, Lei He, Majid Sarrafzadeh, "*NeuroGlasses: A Neural Sensing Healthcare System for 3D Vision Technology*", IEEE Transactions on Information Technology in Biomedicine (**TITB**), Volume 16, Issue 2, March 2012, Pages 198 - 204.

Navid Amini, Alireza Vahdatpour, **Wenyao Xu**, Mario Gerla, Majid Sarradzadeh, "*Cluster Size Optimization in Sensor Networks with Decentralized Cluster-Based Protocols*", Computer Communication (**COMCOM**) - Elsevier, Volume 35, Issue 2, January 2012, Pages 207 - 220.

Navid Amini, Majid Sarradzadeh, Alireza Vahdatpour, **Wenyao Xu**, "*Accelerometer-Based On-Body Sensor Localization for Health and Medical Monitoring Applications*", Pervasive and Mobile Computing (**PMC**) - Elsevier, Volume 7, Issue 6, December 2011, Pages 740 - 760.

Wenyao Xu, Jia Wang, Yu Hu, Ju-Yueh Lee, Fang Gong, Lei He, Majid Sarrafzadeh, "*In-Place FPGA Retiming for Mitigation of Variational Single-Event Transient Faults*", IEEE Transactions on Circuits and Systems Part I (**TCAS-I**), Volume 58, Issue 6, June

2011, Pages 1372 - 1381.

Fengbo Ren, Richard Dorrace, **Wenyao Xu** and Dejan Markovic, "*A Single-Precision Compressive Sensing Signal Reconstruction Engine on Reconfigurable Platform*", IEEE International Conference on Field Programmable Logic and Applications (**FPL'13**), Porto, Protugal, Sept. 2013.

Ming-Chun Huang, **Wenyao Xu**, Jason Liu, Lei He and Majid Sarrafzadeh, "*Inconspicuous Personal Computer Protection with Touch-Mouse*", International Conference on Human Computer Interaction (**HCI'13**), Las Vegas, Nevada, USA, July 2013.

Wenyao Xu, Ming-Chun Huang, Jason J. Liu, Fengbo Ren, Xinchen Shen, Xiao Liu and Majid Sarrafzadeh, "*Microphone-based Spirometer for COPD*", International Conference on Pervasive Technologies Related to Assistive Environments (**PETRA'13**), Rhodes Island, Greece, May 2013.

Ming-Chun Huang, **Wenyao Xu**, Jason Liu, Lauren Samy and Majid Sarrafzadeh, "*Smart Bedsheet Design for Non-invasive Respiration Rate Measurement*", International Conference on Pervasive Technologies Related to Assistive Environments (**PETRA'13**), Rhodes Island, Greece, May 2013.

Jason J. Liu, Ming-Chun Huang, **Wenyao Xu**, Nabil Alshurafa, Majid Sarrafzadeh, "*On-bed Monitoring for Range of Motion Exercises with a Pressure Sensitive Bedsheet*", IEEE International Conference on Implantable and Wearable Body Sensor Networks (**BSN'13**), Boston, MA, May 2013.

Nabil Alshurafa, **Wenyao Xu**, Jason J. Liu, Ming-Chun Huang, Bobak Mortazavi, Christian Roberts, Majid Sarrafzadeh, "*Robust Human Intensity-Varying Activity*

Recognition using Stochastic Approximation in Wearable Sensors", IEEE International Conference on Implantable and Wearable Body Sensor Networks (**BSN'13**), Boston, MA, May 2013.

Jason Liu, **Wenyao Xu**, Ming-Chun Huang, Nabil Alshurafa and Majid Sarrafzadeh, "*A Dense Pressure Sensitive Bedsheet Design for Unobtrusive Sleep Posture Monitoring*", IEEE International Conference on Pervasive Computing and Communication (**PerCom'13**), San Diego, CA, USA, March 2013.

Mi Zhang, **Wenyao Xu**, Alexander A. Sawchuk and Majid Sarrafzadeh, "*Sparse Representation for Motion Primitive-Based Human Activity Modeling and Recognition*", International Conference on Pattern Recognition (**ICPR'12**), Tsukuba, Japan, November 2012.

Ming-Chun Huang, **Wenyao Xu**, Chien-Yen Chang, Belinda Lange, Yi Su and Majid Sarrafzadeh, "*Smart Glove for Upper Extremities Rehabilitative Gaming Assessment*", International Conference on Pervasive Technologies Related to Assistive Environments (**PETRA'12**), Crete Island, Greece, June 2012.

Wenyao Xu, Ming-Chun Huang, Navid Amini, Jason Liu, Lei He and Majid Sarrafzadeh, "*SmartInsole: A Wearable System for Gait Analysis*", International Conference on Pervasive Technologies Related to Assistive Environments (**PETRA'12**), Crete Island, Greece, June 2012.

Zhinan Li, **Wenyao Xu**, Anpeng Huang and Majid Sarrafzadeh, "*Dimensionality Reduction for Anomaly Detection in Electrocardiography: A Manifold Approach*", IEEE International Conference on Implantable and Wearable Body Sensor Networks (**BSN'12**), London, UK, May 2012.

Wenyao Xu, Mi Zhang, Alexander A. Sawchuk and Majid Sarrafzadeh, "*Co-Recognition of Human Activity and Sensor Location via Compressed Sensing in Wearable Body Sensor Networks*", IEEE International Conference on Implantable and Wearable Body Sensor Networks (**BSN'12**), London, UK, May 2012.

Ming-Chun Huang, Ethan Chen, **Wenyao Xu**, Majid Sarrafzadeh, Belinda Lange, Chein-Yen Chang, "*Gaming for Upper Extremities Rehabilitation*", ACM Conference on Wireless Health (**WH'11**), San Diego, CA, October 2011.

Navid Amini, **Wenyao Xu**, Zhinan Li, Ming-Chun Huang, Majid Sarrafzadeh. "*Experimental Analysis of IEEE 802.15.4 for On/Off Body Communications*", IEEE Symposium on Personal Indoor Mobile Radio Communications (**PIMRC'11**), Toronto, Canada, September 2011.

Wenyao Xu, Zhinan Li, Ming-Chun Huang, Navid Amini, Majid Sarrafzadeh. "*e-Cushion: An eTextile Device for Sitting Posture Analysis*", IEEE Conference on Body Sensor Networks (**BSN'11**), Dallas, TX, May 2011.

Wenyao Xu, Fang Gong, Lei He, Majid Sarradzadeh, "*Wearable Assistive System Design for Fall Prevention*", Joint Workshop on High Confidence Medical Devices, Software, Systems & Medical Device Plug-and-Play Interoperability (**HCMDSS/MDPnP'11**), Chicago, IL, April 2011.

CHAPTER 1

Introduction

Population ageing is a global phenomenon in out society. It is reported that the number of elderly (people aged 60 years or above) will increase from 600 million to 2 billion by 2050, when it will be the first time in human history that elderly people outnumber children (people aged 15 years). With the condition of the population ageing, the prevalence of chronic diseases, such as heart disease, stroke, COPD, and cancer, is another crisis that needs immediate action. Chronic diseases, the major cause of death in almost all countries, account for more than 60% (35 million) of all deaths currently. It is worthwhile to be pointed out that chronic diseases do not only affect old adults. Furthermore, almost half of these deaths and over 85% of the burden of these diseases were found in people less than 70 years old. Therefore, it is necessary to have an effective solution to control chronic diseases, which can monitor and modify risk factors and other possible causes leading to the development of these diseases before noticeable symptoms of illnesses have developed.

Wireless healthcare technology is seeking for new solutions to make medical resources, including medical facilities, medicines and professionals, accessible for anyone, anytime, anywhere. It enables reducing the medical cost, promoting inclusion and connectivity of individual life and the rest of the world, and increasing the engagement between patients and doctors. The ultimate goal of pervasive healthcare is to revolutionize the operation model of medical system (see Figure 1.1): ”Wireless healthcare will transform health related services from the system based on episodic examination, disease diagnosis and treatment to the one with continuous monitoring, disease predic-

tion and prevention." And these changes will make our healthcare system more effective and economic, which benefits both billions of individuals around us and the societies in which we live.

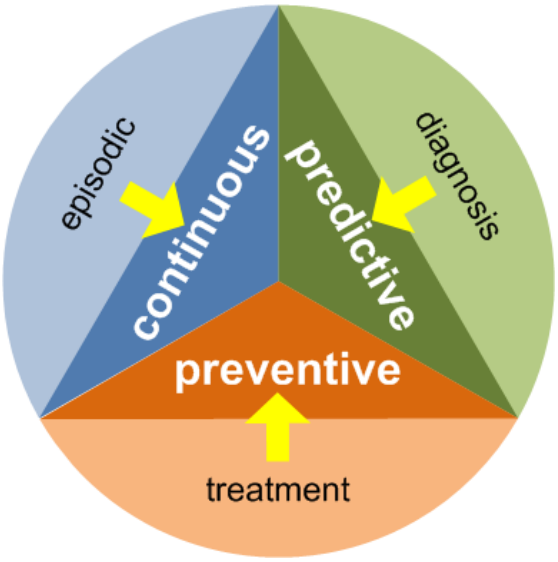

Figure 1.1: The Revolution of Public Health System Driven by Wireless Healthcare.

Wireless healthcare is at the interdisciplinary confluence of engineering, computer science and medicine. Its research work is unique and challenging in identifying real problems, developing practical solutions and evaluating feasibility and performance:

1. Problem Identification: it requires to collaborate with researchers in different domains to identify key research problems in some specific medical application;

2. Solution Development: the solution development involves sensor design, system prototype, signal processing, feedback report and visualization;

3. Performance Evaluation: the solution needs to be implemented and deployed in real application scenarios for evaluation in an uncompromised way.

Accordingly, these interdisciplinary end-to-end research requirements bring both huge challenges and impact to pervasive healthcare research works. In this thesis, I will summarize the progress on a couple of high-impact medical applications. As part

of my research vision, I have identified and developed many novel cost effective, deployable, and application-specific medical sensing systems that can be easily used in daily life by exploring, designing and building advanced sensors and signal processing technologies. In summary, my research work has successfully addressed four important medical applications: Pressure Ulcer Reduction, Cardiopulmonary Monitoring, Fall Prevention and Rehabilitation. These projects are shown in Figure 1.2, and will be elaborated in the following chapters.

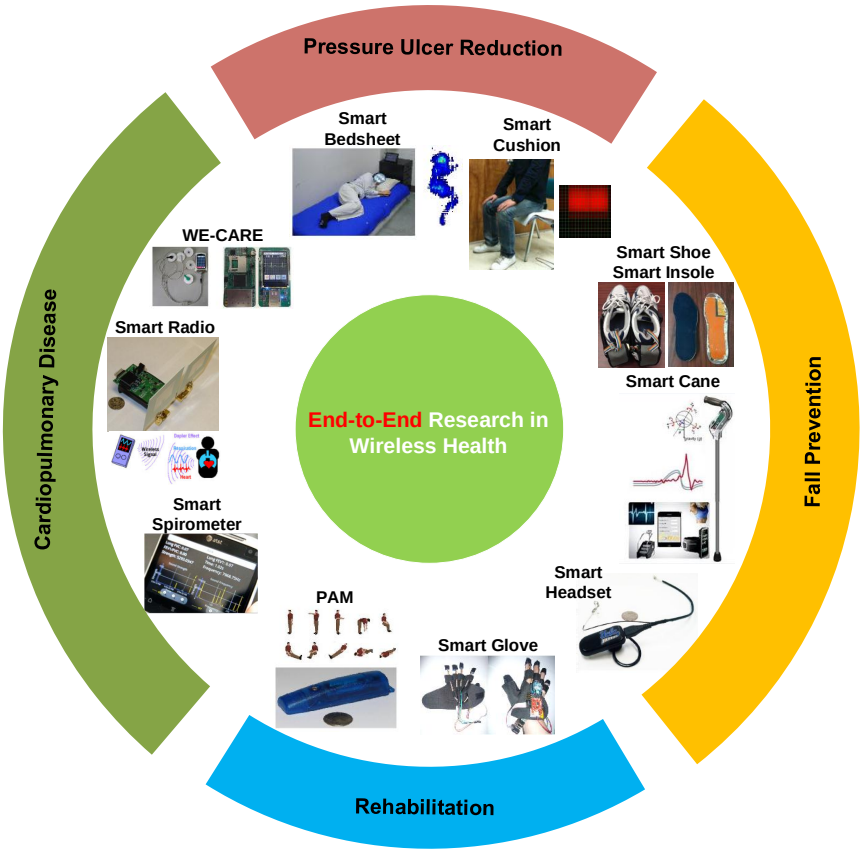

Figure 1.2: Wireless Health Projects in This Thesis.

CHAPTER 2

Pressure Ulcer Reduction

2.1 Introduction and Background

During the average 7 to 9 hours per day that we sleep, the human body heals itself and grows. Those who have poor sleeping quality are prone to stress, fatigue, attention deficit, or eating disorders [BRM89]. Sleep stage is a proven biometric in diagnosing cardiovascular disease, diabetes and obesity [Par09]. Sleep difficulty is associated with psychiatric disorders such as depression, alcoholism and bipolar disorder [Tha06].

Among the indicators of determining sleep quality (such as sleep stage and sleep difficulty), *sleep posture* is also one of the most important factors and is heavily used in performing medical diagnosis. One of the most common conditions is sleep apnea. In recent years, several research works on sleep apnea analysis with sleep postures have been investigated. Lee et al. reported that lateral (lying on side) postures can reduce sleep disorders for mild and moderate sleep apnea patients [LPH09]. In related medical conditions, Ambrogio et al. discovered the relationship between sleep postures and chronic respiratory insufficiency, which leads directly to sleep apnea [ALK]. Further work by Oksenberg and Silverberg investigated breathing disorder and sleep postures [OS06]. These authors all concluded that patients with respiratory conditions should avoid sleep in the supine (lying on back) position.

In addition to direct effects on respiratory problems, sleep posture can be important during the recovery from serious operative procedures. It has been shown that sleep quality affects the recovery times of patients in hospitals [SDH93]. More specifically,

one of the main problems for post-surgical patients and elderly patients is formation of pressure ulcers [PHR98]. Pressure ulcers, or bedsores, are localized injury to body tissue, usually near the bone, resulting from low blood circulation and lack of movement. Pressure ulcers are a serious, life-threatening disease, they develop quickly and are expensive to treat once they have progressed far enough [BMN10]. Prevention is the best way to combat this problem, and in many cases, pressure ulcers are preventable. Hospital staff need to be attentive to patients that are more susceptible to this condition, and take action to relieve pressure on the highly sensitive locations by changing their sleep postures. Current best practices in nursing involve moving patients every several hours. However, there is no guarantee that patients remain in one posture in the meantime, or even if patients are turned onto already sensitive locations.

Given these applications, autonomously monitoring patients during recovery is desired, especially when pressure ulcers can develop very quickly. The goal of any medical system that prevents the formation of pressure ulcers requires the analysis of sleeping postures, as well as notifications of susceptible and impending pressure points on the patient's body. Therefore, there is indeed a need for automatic sleep posture monitoring.

To date, researchers have proposed different ways to monitor sleep posture automatically. Video cameras and microphones have been used previously to study sleep posture patterns. For example, Nakajima et al. [NMT] prototyped a system based on visual signals to analyze sleep posture changes. However, the drawbacks of using video involve lighting issues. Low light levels at night adds noise to the images, and even when near-infrared cameras are used [LY08] the images still produced non-uniformity and artifacts. Furthermore, video and voice taping raise serious privacy concerns for users.

Inertial sensors, including accelerometers, gyroscopes and magnetometers, are another applied technique used to monitor sleep. Sadeh and Acebo attached several triaxial accelerometers on limbs of people to monitor the sleep via actigraph [SA02].

Kishimoto et al. deployed 14 wearable motion sensors on users at home for remote sleep posture analysis [KAO06]. The main downside to this technique is that sensors have to be attached to body which can be uncomfortable or burdensome to the users.

Alternatively, dispersed pressure sensors deployed in the mattress can record when changes in body posture occur. This method is unobtrusive and does not interfere in the comfort of users. Also it is a stable medium that is not affected by changes in the environment. Hoque et al. facilitated a mattress with wireless-powered accelerometers to record the movement activity [HDS10]. Jones et al. developed a bedsheet system with 24 pressure sensors [JGK06]. However, the focus was on detecting posture change rather than recognizing body posture. Similarly, Foubert et al. were able to detect changes from lying to sitting posture [FMG12].

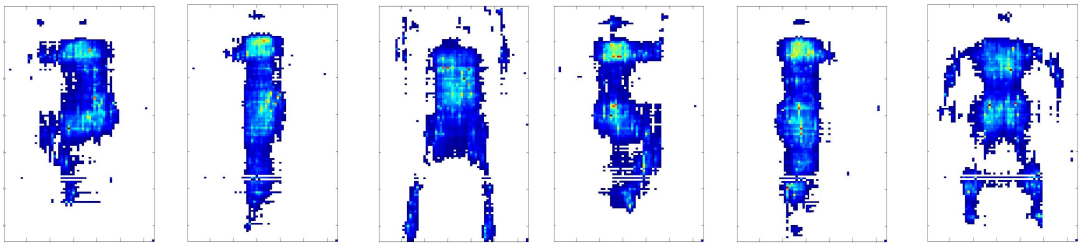

Figure 2.1: Human Body Pressure Image Samples

In this chapter, we focus on sleep posture analysis using pressure sensors. We employ a dense pressure sensitive textile bedsheet and apply pressure image analysis for sleep posture recognition. Our contribution in this work is threefold. First, we propose a framework for automatic sleep posture analysis based on a dense pressure sensitive bedsheet prototype (64×128 sensors) with e-textile material. We would like to argue that pressure image analysis is more challenging than visual imaging due to imcomplete body pressure maps and self occlusions. Second, we define and discuss a set of geometric features from pressure images for posture analysis. These features are effective to not only distinguish different postures but characterize each posture with physical meanings (the details about geometric features will be elaborated in Section

5.3). Third, we develop *three* heuristics based on sparse representation to classify sleep postures. We evaluate our proposed methods with 14 subjects for 6 common sleep postures in static evaluation trials, and 8 hour continuous monitoring trials where we use transitional information from one posture to the next. The proposed method exhibits better performance in terms of accuracy and robustness than traditional classification methods.

In contrast to previous work which have generally focussed on recognizing three postures, Left Fetus, Right Fetus, and Supine postures [HLA09, NAZ10], we describe here a classification system that includes additional harder and commonly used postures. These being Left Log, Right Log, and Prone. The log postures are positions where subjects are lying on their sides with legs almost straight. In many hospital settings, these postures are supported with pillows behind their shoulders and back. The aim of such postures is to to ameliorate the possibility of developing pressure ulcers on the hips, shoulders, and buttocks.

The remaining part of the chapter is organized as follows. Section 5.2 describes the overall design of this monitoring system that incorporates a pressure sensitive bedsheet. Section 5.3 describes the algorithmic process of sleep posture recognition by extracting pressure image features and classification using the theory of the Sparse Classifiers. Experimental set up and results are given in Section 5.4. Finally, future work and conclusion are discussed in Section 5.5.

2.2 Bedsheet Design

In this section, we present the design of the bedsheet system. The goal of this specialized bedsheet is to record the pressure distribution of the body while sleeping and then perform data analysis for medical applications. For instance, when a patient has had recent surgery around the left hip, limited pressure should be applied on that area and a left-lying posture should not be allowed. When the bedsheet system detects that the

patient is lying on his left side for a period of time, the patient or caregivers can receive an alert to change the posture. Accordingly, the bedsheet system is designed with the following consideration:

- High-resolution: The bedsheet should offer high resolution for pressure sensing. Given enough resolution, it is possible to quantify the applied pressure on body parts and enable high accuracy medical diagnosis.
- Comfort: The user should feel comfortable lying on the sheet. Also, it should be easy to deploy in the home or hospital.
- Low-cost: For widespread use, the cost for the bedsheet implementation should be low and affordable for most people.

There are some existing sensor products [Xse, Vis] that comprise of many piezo-electrical pressure sensors. However, none of them meets the above design criterions for wide applications.

Figure 2.2: Pressure Sensitive Bedsheet

Figures 2.2 and 2.3 show the prototype of our bedsheet system. The system consists of three components: a 64 $\times$ 128 pressure sensor array, a data sampling unit, and a tablet for data analysis and storage. The sensor array is based on eTextile material which is a fiber-based yarn coated with piezoelectric polymer [XLH11]. The initial

resistance between the top and bottom surfaces is high. When extra force is applied on the surface of the eTextile, the inner fibers will be squeezed together and the electrical resistance will become smaller.

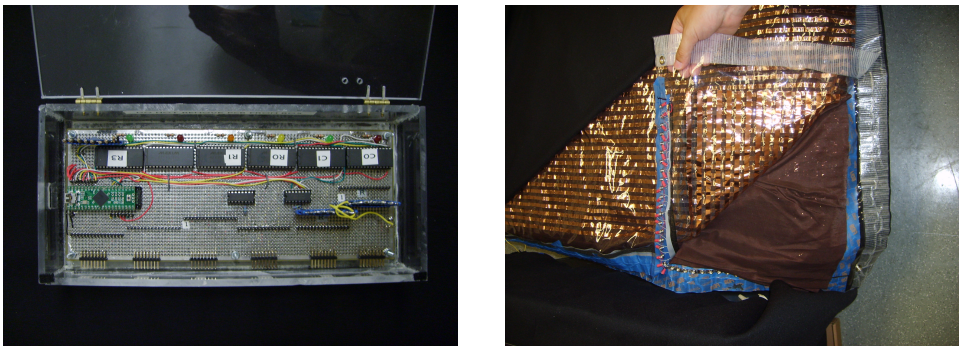

(a) Scanning module (b) E-textile between conductive lines

Figure 2.3: System Components

The textile sensor array has a three-layer sandwiched structure: the top layer is normal fabric uniformly coated with 64 parallel conductive lines; an eTextile layer in the middle; and a bottom layer with 128 conductive lines (perpendicular to the top 64 lines). Within this structure, each intersection of conductive lines becomes a pressure sensitive resistor. In total there are effectively 8192 pressure sensors.

When an electrical potential is applied between one of the vertical and horizontal conductors, the resistance at the intersection point can be measured. By scanning all of the vertical and horizontal lines in sequence, a resistance map can be created of the entire bedsheet and, after converting to digital 8 bit values, a pressure image results.

Figure 2.4(a) shows an example of a user lying on the bedsheet. The subject sleeps on the bedsheet in a right fetus posture, and the corresponding pressure image is illustrated in Figure 2.4(b). We can see that body parts (such as hip, legs) are shown clearly in the pressure image due to the dense sensors in the bedsheet. It is helpful to characterize the geometrical features of sleep postures and posture classification, which will be discussed in detail in the next section.

(a) One subject on the bedsheet system (b) Pressure image

Figure 2.4: System demonstration with one subject sleeping in a right fetus posture.

2.3 Framework for Sleep Posture Analysis

Figure 2.5 shows the sleep posture analysis process. The central three steps, Pre-processing, Feature Extraction, and Sparse Classification, will be discussed in this section.

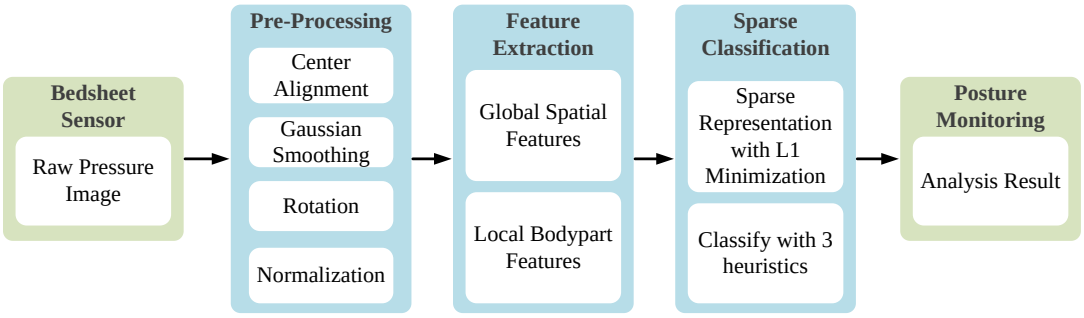

Figure 2.5: Sleep Posture Recognition Framework

2.3.1 Pre-processing

The pre-processing on the raw pressure images is required so that the images can be standardized in such a way to enable successful classification. The raw images contain

noise and artifacts that affect classification, and pre-processing mitigates the side effects as much as possible.

- Firstly, the subject can be located anywhere on the bedsheet, so to correct this, the images are aligned to a common center of mass and relocated to the center of the image.
- A smoothing filter of a symmetric 5×5 unit normal distribution is applied. This smoothing minimizes the effect of noise in the pressure map.
- The images are rotated so that the dominant axis of the body shape is aligned vertically in the image. The dominant axis is found by an eigenvector calculation by approximating the human body geometry as an ellipse. This accounts for the different lying angles for the subjects.
- The images are normalized so that the sum of pixel weights is one. This step attempts to counteract the affects for the different body mass of patients.

2.3.2 Feature Extraction

Traditional feature extraction methods on images include dimension reduction techniques. Widely popular is Principal Component Analysis [Jol] which relies on finding the dominant orthogonal axes which maximizes the statistical variances in the data. PCA is largely data dependent and is a general method to find macro structure in datasets. This method has been applied to sleep posture recognition in current literature [YOF11].

In this work, we propose a different method of feature extraction for posture classification that is based on the geometry of the pressure images. It is more attuned to the physical characteristics of the body shape and has a definite physical meaning. An advantage of using these proposed features over PCA reduction is the processing time required to extract these features; our proposed features are based on simple geometry.

In all, we propose 32 features to be extracted from each of the pressure images. The features are described as either Spatial features or Bodypart features. Spatial features are those features that describe global aspects of the image such as the proportion of the image that is covered by the subject, how symmetric is the image, and direction of any curvature in the pressure image. Bodypart features are localized features that describe location and size of expected body parts such as the hip and shoulder.

Table 2.1: Global Spatial Features

No.	**Name**	**Description**
1	Coverage	Proportion of image covered
2	Per25	Coverage of 25% of pressure
3	Per50	Coverage of 50% of pressure
4	Per75	Coverage of 75% of pressure
5-12	Reg1 - Reg8	Coverage over 8 fixed rectangular regions
13	Symmetry	Measure of pressure symmetry
14	Balance	Measure of pressure on both sides of image
15	DirCurve	Measure of curvature of pressure image

Refer to Table 2.1 for a full a listing of the global Spatial features and Table 2.2 for the localized Bodypart features. A more detailed explanation of the features follows here. Unless otherwise stated, we will assume the x axis is along the short side of the bedsheet, the y axis runs along the long side of the bedsheet.

Coverage Features (1-12)

The first feature is Coverage which is the number of pixels that have non-negative sensor values divided by the total number of pixels. The next 3 features only consider coverage for the pixels that contain 25%, 50%, 75% of the total pressure. Features 5-12 are coverage by regions. The regions are 8 equally sized subdivisions of the image as shown in Figure 2.6. Given that the original dimensions of the image are 64×128

pixels, the region sizes are 32 $\times$ 32 pixels.

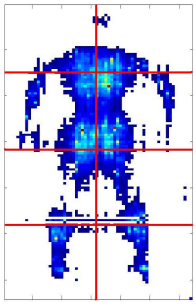

Figure 2.6: Coverage by Regions: Features 5-12

Symmetry and Balance (13, 14)

Symmetry is the sum of the absolute value of the difference of pixels on either side of the center image line. A supine posture would have more symmetry than a side posture. Balance is the sum of the difference of pixels on either side of the center image line. This is different to the Symmetry measure; we do not take the absolute value of the difference of pixels. The resulting measure describes which side of the image contains most of the pressure.

Direction of Curvature (15)

This measure detects the dominant direction of curvature of the body image. A person lying on one side will have a detected body curvature, whereas a supine position should exhibit a straighter pressure image. The steps to extract this feature metric are as follows:

- Create a binary image that contain pixels that are above a suitable threshold. The choice of threshold is obtained experimentally, although a reasonable estimate is 50% of the peak sensor value.
- Skeletonize the binary image by finding midpoints of boundary pixels (see Figure 2.7).

- Remove joint pixels from the skeleton so that each curve is separated. Remove curves that are shorter than 5 pixels.

- For all pixels along the curve, find the angle bisector. The director of curvature is taken as the sum of the y components of the angle bisectors, i.e. in the lateral axis of the bedsheet.

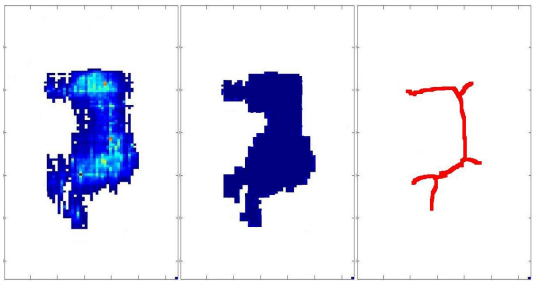

Figure 2.7: Direction of Curvature feature: Left: original image. Middle: thresholded image. Right: skeletonized image.

Table 2.2: Local Geometrical Bodypart Features

No.	**Name**	**Description**
16,17	HipPoint	(x, y) location of hip location
18-21	HipBox	(x, y, width, height) of bounding box of hip
22	HipArea	Area in pixels of bounding box of hip
23	HipPtoBox	Ratio of hip location to bounding box width
24,25	ShPoint	(x, y) location of shoulder location
26-29	ShBox	(x,y,width,height) of bounding box of shoulder
30	ShArea	Area in pixels of bounding box of shoulder
31	ShPtoBox	Ratio of shoulder location to box width
32	HipShDist	Hip to Shoulder Distance

Hip Features (16-23)

Since pre-processing of the image is done initially, we make the assumption that the hip

is located in the quarter of the image below the center of mass of the pressure image. An estimate of the hip location is taken to be the pixel that is located at the weighted center of pixels in this quarter image. The bounding box around the hip is the rectangular region of the pixels that contain 75% of the pressure value within the quarter image below the center of mass of the pressure image. The ratio of hip location to bounding box width provides a measure that shows where the hip location is in relation to the bounding box of the hip.

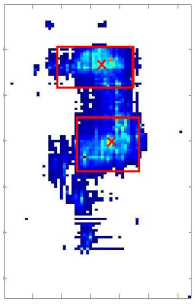

Figure 2.8: Hip and Shoulder Features

Shoulder Features (24-31)

Similar to the hip features (16-23) above, we extract the same information for the shoulder. A similar assumption applies to the quarter image above the center of mass for the shoulder location. Figure 2.8 shows a sample of the locations and bounding boxes of the hip and shoulders. Finally, Feature 32 is the pixel distance between hip and shoulder locations.

Since all the features described above are on different scales, the feature values are scaled and shifted so that the resulting values are in the range [0,+1].

2.3.3 Classification Preliminaries

Before we investigate Sparse Classfiers, we review the progression of classification basics from Nearest Neighbor to Nearest Subspace, then to Sparse Classification.

The Nearest Neighbor classifier simply finds the closest training sample in the feature space to provide a prediction for a test sample. Euclidean distance is the most common measure of closeness between the test sample and the training samples given that the feature space consists of continuous variables.

With a training data set of n samples, and each training sample having m dimensions (features), let each sample be $a_i \in R^m$. Now given a new test sample $y \in R^m$, the nearest neighbor is the training sample that minimizes the distance to the test sample:

$$\arg\min_i ||y - a_i x||_2 \tag{2.1}$$

where x is an identity vector and we assume that all features have been scaled to a common range. The prediction is the class to which the nearest sample belongs.

Nearest neighbor classifier is a popular classifier because of its simplicity, robustness to noise as long as there is sufficient training data. However it has several disadvantages such as high dimensional data reduces the effectiveness of classification. Some features (dimensions) may be more important than others in classification and Nearest Neighbor does not take this into account.

The Nearest Subspace classifier [LGL] extends Nearest Neighbor to include information about assigned class labels. Instead of finding the closest training sample, Nearest Subspace finds the closest subspace that is spanned by training samples belonging to that class. So given a training data set of n samples, and each training sample having m dimensions (features) and having a class label k, let the training samples for class k be A^k. The training samples are column vectors placed side by side. Now given a new test sample $y \in R^m$, the nearest subspace is the class that minimizes the distance of y

to the subspace spanned by all the training samples of that class:

$$\arg\min_{k} ||y - A^k x||_2 \tag{2.2}$$

where x is a vector of weight coefficients. For each class k, the test sample y can be represented by a weighted combination of the training samples in class k if we consider each of the training samples as basis vectors in the subspace spanned by the training samples. So for each class k, $A^k x$ represents a reconstructed sample similar to y. This classifier assigns the class label which minimizes the reconstruction error. The solution to Nearest Subspace can be found using convex optimization with the constraint that all weights are non-negative. Without this constraint, the solution degenerates in this overdetermined system.

The Nearest Subspace classifier finds a representation of a test sample in the subspaces spanned by class training samples. We extend this idea further using Sparse Representation. The general idea is to represent the test sample using all the training samples, initially without regard to the classes of the training samples. By imposing sparsity constraints on the representation of the sample, a different type of classifier can result. The following section describes classification using Sparse Representation of samples.

2.3.4 Classification using Sparse Representation

Sparse Classification has been used previously in other medical analysis and has been shown to have effective performance over a wide range of applications [XZS12b]. The classification method comes from the theory of Compressed Sensing [CRT06b] which proposes that data exhibits sparsity in some transformed representations. That is, a signal can be represented as a sparse signal in a transformed feature space, and can be accurately re-constructed with a lower sampling rate than the Nyquist-Shannon rate.

Given a data set of n samples, with each sample having m dimensions (features), define the data matrix $A \in R^{m \times n}$ that comprises of these m-element column vectors

arranged side by side. Now given a new sample $y \in R^m$, can a solution $x \in R^n$ be found such that x is described in terms of the data set? i.e. can we find x that satisfies:

$$y = Ax. \tag{2.3}$$

So y is a linear combination of the columns in the data set, and $x = [x_1, x_2, ..., x_n]^T$ is an unknown vector of coefficients. This linear system is underdetermined when there are more unknowns than equations, and hence there are infinitely many solutions for x. This is the case for our formulation of posture classification in this chapter. However, if certain constraints are imposed, then a unique solution for x will exists that will accurately represent the original sample. There are 3 main sparsity constraints on x that have been considered in literature.

- l_0 sparsity is defined to minimize the number of non-zero elements of x. Solving for x has been shown to be NP-hard [Nat95b].
- l_2 sparsity is the efficient least squares solution, however this is not always equivalent to the l_0 solution.
- l_1 sparsity is defined as the minimal sum of absolute values of elements of x. Candes et al. [CRT06b] have proved that l_1 sparsity is equivalent to l_0 and, moreover, can be solved as a convex optimization problem:

$$\hat{x} = \arg\min_x ||x||_1, \tag{2.4}$$
$$s.t. \quad y = Ax.$$

The sparse representation of a sample is used in classification by matching this representation to a set of class labels. The data set A is composed of training samples and each sample has been assigned a class label, C_n. Let each training sample be represented as a column vector, a_{ij}, where j is the sample number within class i. The number of samples need not be the same for each class. The data matrix A is shown here with samples grouped together in their classes:

$$A = \underbrace{\begin{bmatrix} | & | & & | & | & & | & | & \\ a_{11} & a_{12} & \dots & a_{21} & a_{22} & \dots & a_{k1} & a_{k2} & \dots \\ | & | & & | & | & & | & | & \end{bmatrix}}_{class1} \underbrace{\qquad}_{class2} \cdots \underbrace{\qquad}_{classk}.$$

Any test sample y is represented by a linear combination of the training samples:

$$y = a_{11}x_1 + a_{12}x_2 + \cdots + a_{kj}x_n, \tag{2.5}$$

where k is the number of class labels and j is the number of training samples for the k-th class.

The l_0 minimized sparse solution for x will have only a small number of non-zero elements. The training samples that correspond to the non-zero elements are those that can represent the new sample well. We propose 3 heuristics to select the class label given a sparse solution for x and the data set with training labels as follows.

- Maximum Coefficient (MC). The class label belonging to the training sample that corresponds to the largest coefficient of the sparse solution of x is the predicted class label:

$$\hat{k} = C_{\arg\max_i(x_i)}. \tag{2.6}$$

- Maximum Sum of Class Coefficients (MSCC). The predicted class label is the class whose sum of coefficients of x is maximized:

$$\hat{k} = \arg\max_k(\sum_{i \in a_{ki}} x_i). \tag{2.7}$$

  In other words, for each class k, take the sum of the coefficients of x that correspond to the training samples belonging to that class. The predicted label is the class that maximizes these sums. The training samples that are most closely represented to the test sample should correspond to the bulk of elements of the sparse solution to x.

- Minimum Class Residual (MCR). An alternate choice for a heuristic to predict the class label is to find the class that minimizes the class residual. The residual is the error between the test sample and the reconstructed sample based on the sparse solution to x:

$$residual = ||y - A\hat{x}||_2. \tag{2.8}$$

So the predicted class is

$$\hat{k} = \arg\min_k ||y - A_{ki}x_i||_2. \tag{2.9}$$

Each of these 3 heuristics are evaluated in Section 5.4.

2.3.5 Hidden Markov Model for Continuous Posture Evaluation

In our experiments on the continuous sleep posture monitoring, we investigate the use of Hidden Markov Models [Rab89, QB08] on time sequential images. The Hidden Markov Model (HMM) is a stochastic process where internal states of a system depend only on previous states and are hidden from direct observation. In our application, the hidden states are the sleep postures of the subjects and the direct observations are the pressure images from the bedsheet. Using HMMs, the sequence of postures is ascertained from the sequence of pressure images and knowledge of the state transition and observation probabilities.

The formulation of HMM is as follows (refer also to Figure 2.9). We represent N postures as N hidden states, $\{S_1, S_2, \ldots S_N\}$. Postures can change to another posture according to an assigned transition probability a_{ij}:

$$a_{ij} = Pr(s_{t+1} = S_j \mid s_t = S_i), \tag{2.10}$$

where s_t is the posture at time t. So a_{ij} is the probability that a subject who is currently sleeping in posture i changes to posture j. Sleeping postures can remain in one state for an indeterminate amount of time, i.e. the current state can transition to the same state, and this allows time-scale invariance in this model. With N postures, there are

$N \times N$ transition probabilities. In our experiments in Section 5.4, the state transition probabilities for each subject are calculated from the training data.

Although the direct observable outputs from our system are the pressure images, we apply our classification method on each image to produce predictions for postures. So for each state S_i, there is the probability b_{iq} that posture q is predicted. Let v_q be the predicted posture, then the observation probability, b_{iq}, is the probability of predicting posture v_q given the hidden posture is S_i:

$$b_{iq} = Pr(v_q \mid s_t = S_i). \tag{2.11}$$

So, for every observed pressure image at time t, the HMM calculates all the observation probabilities for the N predicted postures. The actual probability calculation is based on a confidence measure from each of our heuristics of the Sparse Classifier.

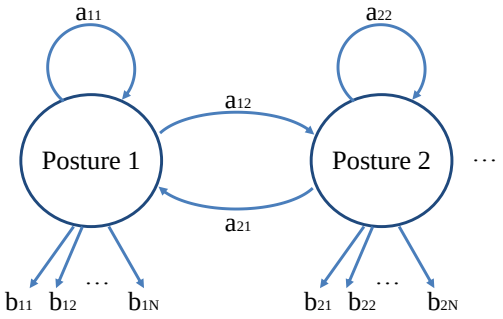

Figure 2.9: Hidden Markov Model with hidden postures. Only 2 postures are shown in this diagram.

Our proposed confidence measure is a relationship between first best match and second best match from a different posture [Low04]. For example, the Maximum Coefficient (MC) heuristic finds the posture that corresponds to the training sample with the largest coefficient of the sparse solution. Let the maximum coefficient for this predicted posture v_q be m_1. Let the second best coefficient of the sparse solution that does not have the same predicted posture v_q be m_2. Then we can calculate the observation probability as:

$$\frac{m_1}{m_1 + m_2}. \tag{2.12}$$

Since the solution of the coefficients is sparse, most of the observation probabilities are zero. The observation probability for the Maximum Sum of Class Coefficients (MSCC) heuristic is similar where the first best match m_1 is the maximum sum of the class coefficients and the second best match m_2 is the next best sum of the class coefficients of a different class. The Minimum Class Residual (MCR) is adjusted to account for the minimization:

$$1 - \frac{m_1}{m_1 + m_2}, \tag{2.13}$$

where m_1 is the minimum class residual and m_2 is the residual for the next best class. We present the HMM results for the confidence measures for our 3 heuristics in Section 2.4.3.

2.4 Experimental Results

2.4.1 Experimental Setup

We ran two sets of studies in the lab to evaluate the performance of the system for sleep posture monitoring. The first study was designed to collect training data and to evaluate short term performance over fixed intervals. The second study analysed the performance of the system for overnight continuous monitoring. The results of the second study is given in subsection 2.4.3.

This section describes the performance of the first study. There are 14 subjects in the experiment, where 9 subjects are male and 5 subjects are female. The weight of the subjects ranges from 55kg to 85kg, and height between 155cm and 185cm, as shown in Table 2.3. The bedsheet system was deployed on a standard twin-size coil spring mattress during the experiments (See Figure 2.2).

In Idzikowski's study of 1000 people [Idz03], left and right fetus postures, i.e. with

Table 2.3: Training subjects

	Gender	Age	Weight (kg)	Height (cm)
1	Female	25	57	158
2	Female	31	53	162
3	Female	27	65	168
4	Female	24	58	162
5	Female	23	60	165
6	Male	27	70	178
7	Male	26	74	172
8	Male	22	62	170
9	Male	35	70	180
10	Male	39	66	178
11	Male	28	72	184
12	Male	27	68	175
13	Male	29	63	173
14	Male	26	65	176

legs bent, are most common at 41%. The other side lying postures, i.e. with straight legs, account for 28% of positions. We refer to these as log postures. Supine (8%) and prone (7%) postures are the next most common. Therefore, for the experimental evaluation, we investigate the 6 postures including Left-Log (LL), Left-Fetus (LF), Right-Log (RL), Right-Fetus (RF), Prone (P) and Supine (S). The examples of these postures are shown in Figure 5.10.

In the data collection, 40 samples were recorded for each of the 6 postures for each subject. At fixed intervals, the pressure image of the subject's posture was recorded while the subject maintained a comfortable sleeping position. Variations in body, arm and leg positions were allowed and the system is tested on a range of positions that fall within the 6 defined postures. All postures include a standard queen size pillow for the

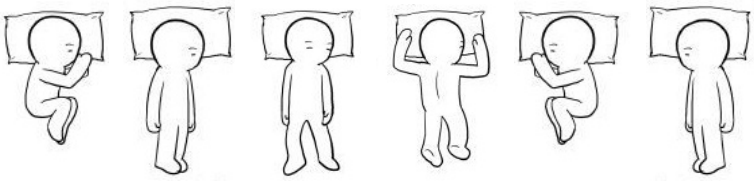

(a) Right Fetus (b) Right Log (c) Supine (d) Prone (e) Left Fetus (f) Left Log

Figure 2.10: Six Postures used in experiments.

head. Testing was carried out with Leave One Out Cross Validation by subject, i.e. test on one subject's data with the training data from all the other subjects. Repeat this for each subject. Sparse classifiers are implemented using the CVX convex optimization package [CVX12].

(a) Camera frame for overhead recording (b) Sample of overhead image

Figure 2.11: Video recording setup for ground truth labelling

The following experiments were tested against ground truth labelling. Figure 2.11 shows a video camera rigging for the ground truth visual image collection. All posture labels were marked manually from the visual images.

2.4.2 Sparse Classification Results

Table 2.4 summarizes the precision and recall results of 6 posture classification using the set of geometric features with different classifiers. The Sparse Classifiers with Maximum Sum of Class Coefficients (MSCC) heuristic and Minimum Class Residual (MCR) heuristics show a 20% improvement in accuracy over Decision Tree and Nearest Neighbor classifiers, and 6% improvement in accuracy over Nearest Subspace.

Table 2.4: Accuracy comparison to other classifiers

	Precision	Recall	f-measure*
C4.5 Decision Tree	57.0%	56.8%	56.9%
k-Nearest Neighbor	64.7%	62.1%	63.4%
Nearest Subspace	77.0%	76.5%	76.8%
Sparse Classifier (MC)	**65.4%**	**61.0%**	**63.1%**
Sparse Classifier (MSCC)	**83.1%**	**82.7%**	**82.9%**
Sparse Classifier (MCR)	**83.5%**	**82.9%**	**83.2%**

*f-measure is the harmonic mean of precision and recall

We note that the Maximum Coefficient (MC) heuristic does not show any improvement in the accuracy over Nearest Neighbor. The reason was given previously and is such that after the transformation into the sparse domain, the Maximum Coefficient (MC) is a metric similar in nature to Nearest Neighbor. It essentially finds the single training sample that maximizes its representativeness to the test sample, and does not take into account the class membership. Nearest Subspace does take into account class membership and hence exhibits a fair accuracy. The downside to Nearest Subspace is that it requires multiple optimization problems to be solved, i.e. one for each class. We note that the Sparse Classifiers only require a single run since it treats all the class samples as one sample space.

We look more closely at the results of the Spare Classifiers and note the confusion matrices given in Tables 2.5 to 2.9. Table 2.5 shows the confusion matrix for Nearest

Table 2.5: Confusion Matrix Nearest Neighbor

	LL	LF	P	RL	RF	S	Recall
LL	123	6	7	26	41	83	43%
LF	3	194	14	39	3	33	68%
P	1	27	234	0	19	5	82%
RL	46	21	0	171	6	42	60%
RF	45	9	14	25	185	12	64%
S	42	6	3	20	5	210	73%
Precision	47%	74%	86%	61%	71%	55%	

Table 2.6: Confusion Matrix Nearest Subspace

	LL	LF	P	RL	RF	S	Recall
LL	143	0	2	51	41	20	66%
LF	3	243	21	30	4	6	79%
P	10	16	253	0	20	4	83%
RL	27	17	0	183	2	9	76%
RF	44	7	10	13	262	5	77%
S	59	3	0	9	1	242	77%
Precision	50%	85%	88%	62%	90%	84%	

Neighbor classifier and we note the similarity with the Maximum Coefficient Sparse Classifier (MC) in Table 2.7.

Generally, the log postures are harder to recognize than the other postures. Recall for both Left Log and Right Log are always lower than for the other 4 postures, while the precision rates are generally lower but not always. The log postures are most similar to each other since both have legs outstretched and arm positions can vary. The next most similar posture is Supine. This is seen in all of the confusion matrices as high counts for predicted switched Left Log and Right Log, and Supine.

Table 2.7: Confusion Matrix Sparse Classifier (MC)

	LL	LF	P	RL	RF	S	Recall
LL	149	29	24	19	23	42	52%
LF	15	168	26	30	18	29	59%
P	9	24	202	6	20	25	71%
RL	40	25	5	176	22	18	61%
RF	11	22	23	19	194	21	67%
S	44	13	11	9	11	198	69%
Precision	56%	60%	69%	68%	67%	59%	

Table 2.8: Confusion Matrix Sparse Classifier (MSCC)

	LL	LF	P	RL	RF	S	Recall
LL	207	6	2	15	6	50	72%
LF	4	249	14	6	9	4	87%
P	1	22	245	1	12	5	86%
RL	14	27	1	219	12	13	77%
RF	0	9	14	3	262	2	90%
S	30	6	2	1	3	244	85%
Precision	81%	78%	88%	89%	86%	77%	

Figure 2.12 shows two examples of misclassifications of hard log postures. The left image shows Left Log posture that is incorrectly identified as Right-Log. This typical kind of error can be explained from the pressure map that is extended behind the subject's back. Hence misclassifications can occur since the pressure image now looks like a Right Log image. Similarly, the right image shows Right Log posture that is incorrectly identified this time as Supine. Visually, this image is hard to not identify as Supine.

Table 2.9: Confusion Matrix Sparse Classifier (MCR)

	LL	LF	P	RL	RF	S	Recall
LL	202	8	5	18	5	48	71%
LF	2	252	18	5	6	3	88%
P	1	22	249	1	10	3	87%
RL	12	28	2	225	10	9	79%
RF	0	11	15	5	257	2	89%
S	27	9	3	1	3	243	85%
Precision	82%	76%	85%	88%	88%	79%	

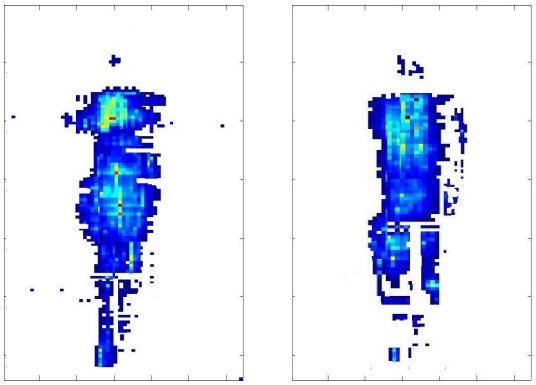

(a) Left Log posture misclassified as Right Log

(b) Right Log posture misclassified as Supine

Figure 2.12: Misclassified Postures

2.4.3 Overnight Continuous Monitoring

To further evaluate the accuracy of the pressure sensitive bedsheet system, we tested the posture analysis for continuous overnight monitoring. In this study, we monitored 3 patients over 3 nights on the bedsheet. Overhead video images of the subjects were recorded to manually extract the ground truth postures. Roughly 2600 pressure images were recorded for each overnight session lasting 7-9 hours. Since subjects do not move much while sleeping, the sampling rate was decreased to 10s per sample for the sake of

memory constraints in the tablet.

We analysed the results using the HMM framework with subject dependent testing. With three complete overnight data for each subject, we used two of the sets for subject training and tested on the third, and repeated with cross validation. The results shown in Table 2.10 compare two classification schemes: one with Hidden Markov Models and the other with plurality voting over sliding window of size 10. Both of these classification methods showed small improvements in the accuracy of posture analysis over long durations and sequential pressure imaging, compared to static posture analysis in the previous sections.

Table 2.10: Experimental results for overnight studies

	Precision	Recall	f-measure
HMM with MC	78.4%	73.6%	75.9%
HMM with MSCC	86.5%	84.7%	85.6%
HMM with MCR	86.0%	84.4%	85.2%
Sliding Window Plurality with MC	73.9%	76.5%	75.2%
Sliding Window Plurality with MSCC	83.7%	84.5%	84.1%
Sliding Window Plurality with MCR	83.8%	84.8%	84.3%

For sliding window plurality voting, the predicted posture is chosen as the posture with the relative majority compared to the other postures, and is updated with a sliding window of fixed size over the set of consecutive previous images. In each group of consecutive samples, the simple plurality vote of the predicted test sample classifications is taken as the classification for that grouping of image samples, i.e. the posture that is predicted most frequently.

Overall, the results of continuous monitoring study show that classification accuracy can be improved when sequential static images are available. The HMM based sequential methods show roughly 2-3% improvement over static image classification for the Maximum Sum of Class Coefficients (MSCC) and Minimum Class Residual

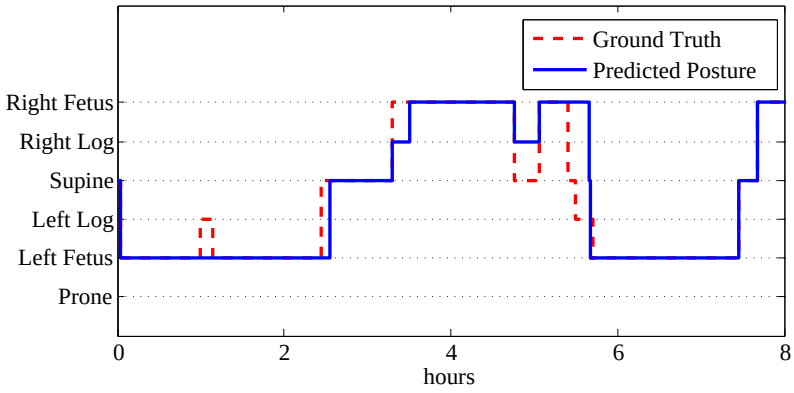

Figure 2.13: An example of one subject's 8 hour continuous monitoring study

(MCR) heuristics. Interestingly, the HMM with Maximum Coefficient method shows the largest improvement. This may be explained by the fact that Nearest Neighbor type methods benefit most by the clustering of points as more data is considered. A sliding window size of 10 improves the classification by a percentage point over static image classification, however this may not be statistically significant over a small total sample size.

Figure 2.13 shows the result of one of the test subjects for an 8 hour overnight continuous monitoring session with predicted and true postures given. The subject is a typical sample of the progression of posture sequences. Here the subject had 12 discernable posture changes.

2.4.4 Stability Analysis

We also analyse the robustness of the classification by investigating the variation during cross validation. Stability is a measure that describes how closely the classifier evaluates results if given different data. Figure 2.14 shows the classification variation for the 6 postures for each of the classifiers.

The Sparse Classifiers have smaller variation values than the other traditional classifiers. This indicates that sparse classification is a more stable classification method.

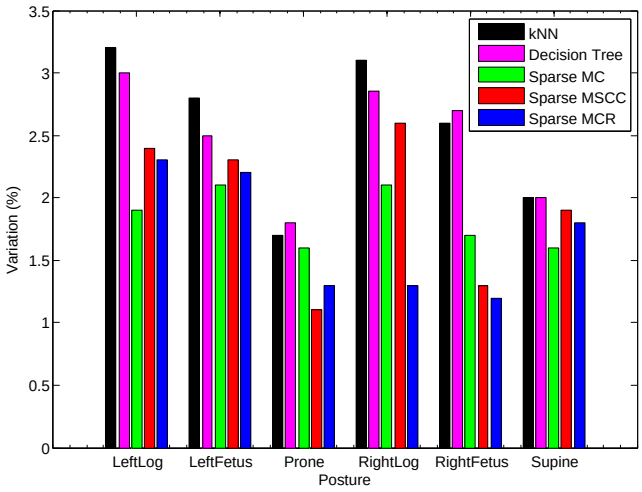

Figure 2.14: Classification variation for 6 postures

The log postures have a higher variation in classification accuracy than the other postures. This is explained by the higher variation in weight distribution for these postures. In our data, the log postures vary much between fully lying on the side and lying on the back.

Although the Maximum Coefficient (MC) Sparse Classifier achieves the same accuracy as Nearest Neighbor, it does perform better when considering its better stability.

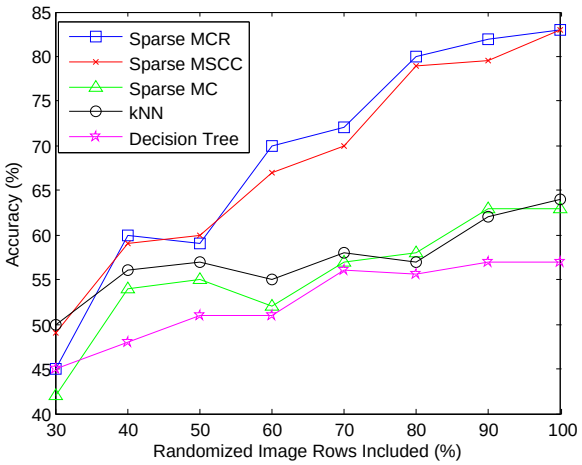

Figure 2.15: Classification robustness with random row deletions

We also consider the robustness of the algorithm with regards to input errors, such as from disconnected wires in the bedsheet. The effect of this would be missing rows or columns of data in the pressure image. Figure 2.15 shows experimentally how a random number of failures of bus lines will affect the accuracy of the classification result. Roughly 20% of the hardware connections can fail with only a 4% drop in classification accuracy.

2.4.5 Feature Selection

In this section, we examine the effect of feature selection in classification. 32 features are extracted from the pressure image set for classification. It is most certainly the case that some features are redundant or do not have any effect on classification results. We employ Sequential Forward Selection (SFS) to find subsets of features that are most descriptive of the whole feature set [JKP94]. This method is considered a wrapper method, ie the feature selection is based on using the classification results themselves and the selection process wraps around the classification.

With this method, the first feature is selected by testing each feature individually in classification. The feature with the highest accuracy performance is chosen first. In the second round of selection, each of the remaining features is used with the first feature in classification. The feature with the highest accuracy result is chosen as the second feature in the feature selected subset. This process continues as one feature is added at a time until all of the features are selected. Since the classification always uses previously selected features, redundant features are not selected until the end.

Figure 2.16 shows the relationship between number of selected features chosen using SFS and classification accuracy for each of the classifiers. Accuracy generally increases as more features are used for all of the classifiers. There is a sharp increase in accuracy using the Sparse Classifier with both Maximum Sum of Class Coefficients (MSCC) and Minimum Class Residual (MCR) heuristics, from 65% to 78% between

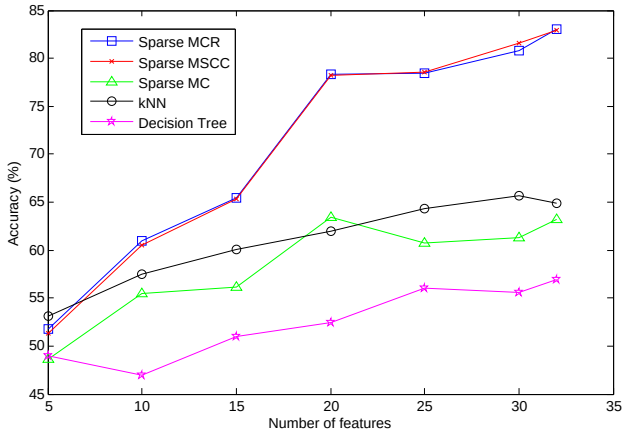

Figure 2.16: The impact of feature dimension on classification accuracy based on Sequential Feature Selection

15 features and 20 features. Moreover the three Sparse Classifiers appear to have a threshold at 20 features in the accuracy results, with a smaller rate of increase in accuracy as more features are used. The traditional kNN and Decision Tree show modest increase of about 10% throughout the whole feature selection process.

An alternative method of selecting features is based on filtering. Each of the features are evaluated based on how well they separate the data into the correct classes. Table 2.11 shows the order of features ranked by an information gain metric [CT91]. Information gain describes the reduction in information entropy caused by knowing the value of a feature. Features with high information gain allow better classification. Information gain, IG, is given by

$$IG(A, F) = Entropy(A) - \sum_{f \in F} \frac{|A_f|}{|A|} Entropy(A_f)$$

where A_f is the subset of dataset A for which feature F has value f. Entropy is given by

$$Entropy(X) = -\sum_{i=1}^{n} p(x_i) log_2 p(x_i)$$

where $p(x_i)$ is the probability of sample x_i occuring in the dataset X. The features are chosen one at a time and the classification does not include previously selected features.

Table 2.11: Alternative method of ranking features by Single Feature Selection

InfoGain	Feat #	Feature	InfoGain	Feat #	Feature
0.887577	17	HipPoint(y)	0.262988	11	Reg7
0.616256	18	HipBox(x)	0.256317	5	Reg1
0.581828	20	HipBox(w)	0.252169	24	ShPoint(x)
0.554651	16	HipPoint(x)	0.234055	32	HipShDist
0.536393	14	Balance	0.215533	23	HipPtoBox
0.497846	19	HipBox(y)	0.200476	29	ShBox(h)
0.47028	22	HipArea	0.196697	3	Per50
0.443133	6	Reg2	0.186926	4	Per75
0.435716	13	Symmetry	0.186884	28	ShBox(w)
0.400952	10	Reg6	0.171033	2	Per25
0.359848	1	Coverage	0.168928	26	ShBox(x)
0.340698	21	HipBox(h)	0.153444	15	DirCurve
0.321448	25	ShPoint(y)	0.143608	30	ShArea
0.318234	9	Reg5	0.126994	12	Reg8
0.302024	27	ShBox(y)	0.12267	8	Reg4
0.277772	31	ShPtoBox	0.117452	7	Reg3

The disadvantage of this method is that it does not take into account the redundancy in some of the features. In experiments, this method was shown not to be as accurate as the Forward Selection.

It is interesting to note, however, that the highest ranked features are those associated with hip location and bounding box. This can be expected since the diferent postures do vary much in the pressure points of the hip region. It is a strong indicator of side postures versus the supine and prone postures.

2.5 Conclusion

This work presents a sleep analysis design that monitors sleep posture using a pressure sensitive bedsheet. An application for such a system is to enable caregivers the ability to automatically identify when patients are at risk of developing pressure ulcers or when subjects experience sleep apnea. This work also presents the novel use of relevant features that can be extracted from pressure images, as well as state of the art classification methods. We developed three heuristics for sparse classification, and in our experiments, show that both Maximum Sum of Class Coefficients (MSCC) and Minimum Class Residual (MCR) heuristics produce reliable sleep posture estimation.

Pressure monitoring systems need not be limited to sleep posture recognition. In nursing home settings, evaluation of fall risk is a desirable endeavor. Advanced beds are now being developed that can re-distribute support to different regions of the bed [Hil] and also aid in the heat flow through the bed mattress. Using pressure point monitoring, the goal is to increase healing speed of patients.

Future work also involves the ability to monitor transitional states as patients move between pre-defined stable classified postures. There are more challenges here because of the large variations in different subjects' motions. 3D model reconstruction of patients from 2D pressure image is another goal that can be accomplished using the results of this research work.

CHAPTER 3

Cardiopulmonary Monitoring

3.1 Introduction

World Health Organization (WHO) reports that 63% of all deaths are from chronic diseases such as heart disease, lung disorder, cancer and chronic respiratory disease and diabetes [Wor]. Due to the long duration and generally slow progression, chronic disease is difficult to accurately diagnose and treat effectively. So far, the most reliable method for chronic disease diagnosis and treatment is *periodic* medical examinations for health status. In U.S., there are more than 100 million Americans suffering from chronic health conditions. The related cost of caring for them consume 75% of the total national health care bill, of which a significant part is from medical examinations. If there is a reliable method to automatically monitor the patients *at home* and transfer the medical data to doctor for evaluation, it will contribute a significant savings of the health care bill.

Among miscellaneous medical examinations, vital signs (i.e. heart rate and respiratory rate) are the most important measures to access body functions, monitor illness progression and perform effective treatments [DBG05]. Furthermore, vital sign measurements are helpful to predict potential clinical events. For example, the variation in respiratory rate is an important marker for cardiac arrest or admission to the intensive care unit [CCH07].

There are several off-the-shelf home devices for measuring vital signs [Omr, For]. They require users to strictly follow the instrument instructions and perform the mea-

surement under controlled conditions. For example, when the subject is using an ECG device to measure heart beat, the electrode should be attached on the correct body part and subjects should not talk during measurements. Therefore, it is difficult to always obtain the valid vital sign measurements without the assistance of medical personnel. Moreover, due to the inconvenient use of these devices, it is unlikely to periodically perform vital sign measurements by patients themselves. Further, measurements can only be done when the subjects initiate this process. Continuous monitoring is not feasible unless the sensor is attached to the subject all the time.

In recent years, the research community looks for non-invasive methods for vital sign measurement. In general, existing work can be classified into two categories. The first one is based on direct contact. During the measurement, the device needs to contact the user's body. For example, Watanabe et al. [WWT05] presented a thin, air-sealed and pressure-sensitive cushion under the bed mattress to measure heartbeat, respiration and body movements of the subject. Chi et al. [CNK10] developed a capacitive electrode to measure heart rate without direct skin contact.

The other one is based on non-contact technique. Non-contact techniques enable monitoring vital signs remotely and seems more appealing for users. Aoki et al. [ATM01] discussed a non-restrictive visual sensing method to detect the respiration pattern by using a fiber grating camera and processor unit. Zhu et al. [ZFP05] developed an infrared camera based system to monitor the respiration and infer associated heart rate. Chekmenev et al. [CRF05] used a thermal camera consisting of a focal plane array for a long-wave infra-red sensor to extract heart rate and respiration from temperature changes. However, all these existing non-contact methods suffer from the following aspects. First, these sensors are sensitive to the environmental changes such as light or temperature, and there are no robust calibration methods to compensate these changes. Second, subjects should always be within the visual range of sensors, which becomes another kind of constraint. Last, they are expensive and not affordable for home use.

In this chapter, we present a low-cost microwave Doppler radar based system com-

plementary to existing non-contact techniques. According to Doppler theory [Bla96], the reflection signal will have quantitative phase change, called Doppler shift, due to the movement of objects, and the sensitivity is high enough to measure heart beat and chest wall movement. With the Doppler radar structure and signal model, we propose a novel framework to automatically demodulate the Doppler radar signals and extract heart rate and respiratory rate without any pre-calibration. Therefore, this radar is a low-cost, reliable and easy to setup solution for non-contact vital sign monitoring.

The remainder of the chapter is organized as follows. In Section 3.2 we briefly introduce the background of Doppler radar and related work on radar signal processing. Then we describe the layered architecture of the Doppler-radar motion-sensing system in Section 5.2. In Section 5.3 we address the challenges and present the framework for vital sign detection. The experimental design, performance evaluation and analyses are discussed in Section 5.4. Finally, we outline the future work and conclude the chapter in Section 3.6.

3.2 Preliminary and Related Work

The Doppler effect was proposed by Christian Doppler in 1842 and has been widely applied in motion detection since then. Microwave Doppler radar was first applied to measure respiratory rate and detect sleep apnea in 1975 [Lin92]. Doppler radar transmits a continuous-wave signal, which is reflected by a target, then received and demodulated in a receiver. According to Doppler theory, the position-varying information will be proportionally demodulated in the reflected signal when the net velocity is zero. Therefore, the chest wall movement from volume change in respiration can be detected by the Doppler-radar motion-sensing system. With the advances of wireless transmission and electronic devices, it is feasible to use in-phase and quadrature (*I/Q*) Doppler radar for heart beat detection [DLL04, CLL08].

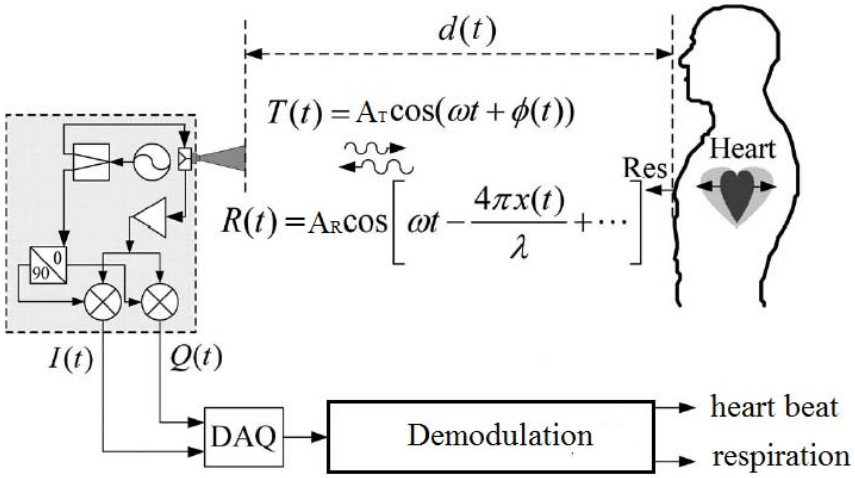

Figure 3.1: The *I/Q* Doppler radar block diagram for non-contact vital sign detection

3.2.1 *I/Q* Doppler Radar

Fig. 3.1 shows the operation theory and block diagram of an *I/Q* Doppler radar for non-contact vital sign detection. The Doppler radar system transmits the continuous-wave signal $T(t)$:

$$T(t) = A_T \cos(\omega t + \phi(t)), \tag{3.1}$$

where A_T is the amplitude of the carrier signal, $\omega = 2\pi f$ denotes the angular velocity (carrier frequency), and $\phi(t)$ represents the time-varying phase information of the transmitted signal.

The subject is at a distance d_0 from the radar and the total traversal distance of microwave signal is $d(t) = 2(d_0 + x(t))$, where $x(t)$ is the time-varying displacement caused by heart beat and respiration.

The transmission wave is reflected by the subject and received at Doppler radar with $R(t)$:

$$R(t) = A_R \cos[\omega t - \frac{4\pi d_0}{\lambda} - \frac{4\pi x(t)}{\lambda} + \phi(t - \frac{2d_0}{c})], \tag{3.2}$$

where A_R is the amplitude of the received signal, $\lambda = c/f$ is the wavelength of the carrier signal, and c is the speed of light. We can see that the time-varying displacement $x(t)$ is modulated in the phase change of the received signal. As shown in Fig. 3.1, $R(t)$ is down-converted by $T(t)$ and then generates two baseband signals. One is the in-phase signal, denoted by $I(t)$:

$$I(t) = A_I \cos[\frac{4\pi x(t)}{\lambda} + \frac{4\pi d_0}{\lambda} + \phi(t - \frac{2d_0}{c})] + DC_I, \tag{3.3}$$

and the other is the quadrature signal, denoted by $Q(t)$:

$$Q(t) = A_Q \sin[\frac{4\pi x(t)}{\lambda} + \frac{4\pi d_0}{\lambda} + \phi(t - \frac{2d_0}{c}) + \phi_0)] + DC_Q, \tag{3.4}$$

where A_I is the amplitude of in-phase signal, A_Q the amplitude of quadrature signal, and ϕ_0 is the phase offset between $I(t)$ and $Q(t)$. DC_I and DC_Q are the DC offsets in *I/Q* channels, respectively. The ratio between A_I and A_Q is called gain imbalance, and ϕ_0 is called phase imbalance. Both gain imbalance and phase imbalance are caused by circuit imperfection.

$I(t)$ and $Q(t)$ are then digitalized by the data acquisition block (DAQ), and the phase change, $x(t)$, is demodulated for heart beat and respiration detection. For the simplicity of presentation, we neglect the constant phase offset, $4\pi d_0/\lambda + \phi(t - 2d_0/c)$, in the *I/Q* receiver and use the following equations to describe the baseband signals in the following part:

$$I(t) = A_I \cos(\frac{4\pi x(t)}{\lambda}) + DC_I, \tag{3.5}$$

$$Q(t) = A_Q \sin(\frac{4\pi x(t)}{\lambda} + \phi_0) + DC_Q. \tag{3.6}$$

3.2.2 Related Work

As shown in Fig. 3.1, demodulation module processes the baseband signals, $I(t)$ and $Q(t)$, for heart beat and respiration information extraction. If the circuit in Doppler radar is perfect, there will be no gain/phase imbalance, i.e., A_I in Eq. (3.5) is equal to A_Q in Eq. (3.6), and ϕ_0 in Eq. (3.6) is equal to zero. Under these ideal-case assumptions, there are several techniques for Doppler radar signal demodulation to extract vital signs. Fletcher and Han developed a low-cost Doppler radar for vital sign monitoring [FH09]. Droitcour et al. approximated *I/Q* signals to linear formulas while the responding phase is small, and then extracted vital signs by tuning carrier frequency [DLL04]. Tao et al. converted transmission wave to a set of pulse signals and detected the phase change on its peaks [TLW09]. Lee et al. proposed a reassigned joint time-frequency transform to track the heart rate [LYK11]. Park et al. presented an arctangent demodulation method with pre-calibration of DC offsets [PLL07]. Massagram et al. assessed the Doppler radar for heart rate variability and respiratory sinus Arrhythmia [MLM09]. Li and Lin formulated *I/Q* signals into a complex vector to perform Fourier analysis, and the phase change can be calculated by iterative spectrum comparison [LL08]. Boric-Lubecke et al. employed the Doppler radar sensor for monitoring heartbeat interval [BLP09].

There are two main drawbacks in existing demodulation methods mentioned above. First, all these methods either require approximating *I/Q* signals [DLL04] [TLW09] and need accurate precalibration of DC offsets [LL08] [PLL07]. In fact, DC offset is produced not only by the electronic components, but also by multi-channel transmission and reflection which is related to the environment. Therefore, the DC offsets in *I/Q* channels have to be re-calibrated whenever the environment changes, which is not applicable in practice. Second, these methods assume circuit component are perfect such that gain/phase imbalances are tiny. In real cases, the effect of gain/phase imbalance is significant in actual radar systems. Park et al. [PYL07] measured the imbalance factors in direct-conversion quadrature radar circuit and reported that imbalance is unavoid-

able. In their experiments, the gain imbalance was 4.7 and phase imbalance was 18.5 degrees by average. Note that phase imbalance has serious negative impact on error rate in signal demodulation [ZH05]. Therefore, it is necessary to have an accurate and robust signal processing technique for signal demodulation in Doppler radar systems. In our application, the associated challenges include two aspects:

1. Accuracy: the demodulation method should take into account all parameters (i.e., A_I, A_Q, ϕ_0, DC_I and DC_Q) in signal model and directly extract the motion component $x(t)$ from *I/Q* signals;

2. Self-calibration: the environment might change and the signal model will be different during measurement. The demodulation method can self-calibrate and tolerate the parameter changes. No manual set-up is required.

3.3 System Overview

In this section, we introduce the proposed Doppler radar system for non-contact self-calibrating vital sign monitoring. Fig. 3.2 shows the overview structure of the Doppler-radar vital-sign-detection system. In our system, there are four layers, including sensor layer, pre-processing layer, modeling layer and information layer. The sensor layer and pre-processing layer are built on the hardware. The modeling layer and information layer belong to software design. The definition and function of each part will be discussed in the following.

3.3.1 Hardware Design

The radar sensor system was designed and built using commercial integrated circuits (ICs). The key building blocks used in the sensor system are shown in Table 3.1. The radar sensor system was designed with homodyne transceiver architecture integrated on Rogers 4350 laminate for enhanced RF performance. The designed hardware pro-

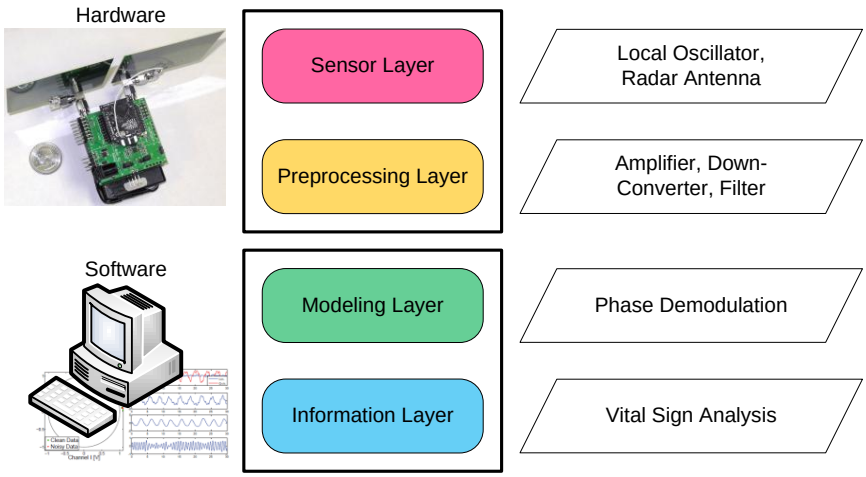

Figure 3.2: The layered structure of non-contact self-calibrating vital sign monitoring system, including sensor layer, pre-processing layer, modeling layer and information layer.

totype of the radar sensor is shown in Fig. 3.3, which illustrates different functional blocks. In our system, there are four layers, including sensor layer, pre-processing layer, modeling layer and information layer. The sensor layer and pre-processing layer are built on the hardware. The modeling layer and information layer belong to the software design. The definition and function of each part will be discussed in the following. The hardware design includes the sensor layer and the pre-processing layer. The sensor layer generates a single-tone carrier signal that is transmitted to the target to gather the desired phase information [Lin92]. In our design, the sensor layer was implemented by using a voltage controlled oscillator (VCO). The single-tone signal from VCO is divided by a balun into two parts: one is transmitted via a transmitter antenna to the target, and the other one serves as the local oscillator (LO) signal to the demodulator. If the target is moving, e.g. the chest wall of the subject, the single-tone carrier signal would be modulated in the phase with the information of the target's movement, which is called non-linear phase modulation [GIL, GLF12]. Though a free-running VCO is used in our design, coherent demodulation is realized since the transmit signal and the LO signal come from the same signal source. The phase noise of the VSO does not

affect the sensitivity in non-contact vital signal detection, owing to the range correlation effect [DBL04]. Two patch antennas have been custom designed for the use in our radar sensor system.

Table 3.1: Building Blocks of the Radar-Sensing System

Blocks	Manufacturer	Specification
VCO	Hittite	2.25-2.5GHz; Pout: 4.5dBm
Demodulator	Skyworks	RF/LO: 0.4 3GHz; Gain: 1.2dB
LNA	Hittite	2.3-2.5GHz; NF: 1.7dB; Gain: 19dB; P_{1dB}out: 6dBm
Gain Block	RFMD	Gain: 12dB; P_{1dB}out: 11dBm
BPF	Johanson	Pass band: 2400 2500 MHz
Op Amp	Maxim IC	Bias: 3V; GBW: 3 MHz
Controller	TI	Bias: 3V; 10-bit ADC

The pre-processing layer is an RF receiver that handles the signal from the sensing layer and down-converts it to baseband *I/Q* signals. A low noise amplifier (LNA) is at the front-end of the pre-processing layer, so as to ensure a good noise figure for the receiver chain. It also provides a 19 dB gain to boost the weak signal reflected from the moving target. A ceramic band pass filter, as shown in Table 3.1, follows the LNA to block the out-of-band interferences. This is important because there are a lot of strong interferences in the air, e.g. 900 MHz cellular signal and 5.8 GHz WIFI signal. The filtered signal is further boosted by a gain block to reach a sufficient power level that can drive the RF port of the demodulator. A quadrature demodulator converts the received signal to baseband *I/Q* signals, which are further amplified by the baseband operational amplifier (Op Amp). The Op Amp is configured with a differential input structure and the baseband gain is determined by the feedback of the amplifier. It should be known that the Op Amp has a gain bandwidth product (GBW) of only 3 MHz. So the Op Amp also serves as a low pass filter that preserves the low-frequency vital sign signals but blocks any other interferers. The baseband output is digitized by a 10-bit

ADC integrated in a microcontroller and further process by the modeling layer and the information layer.

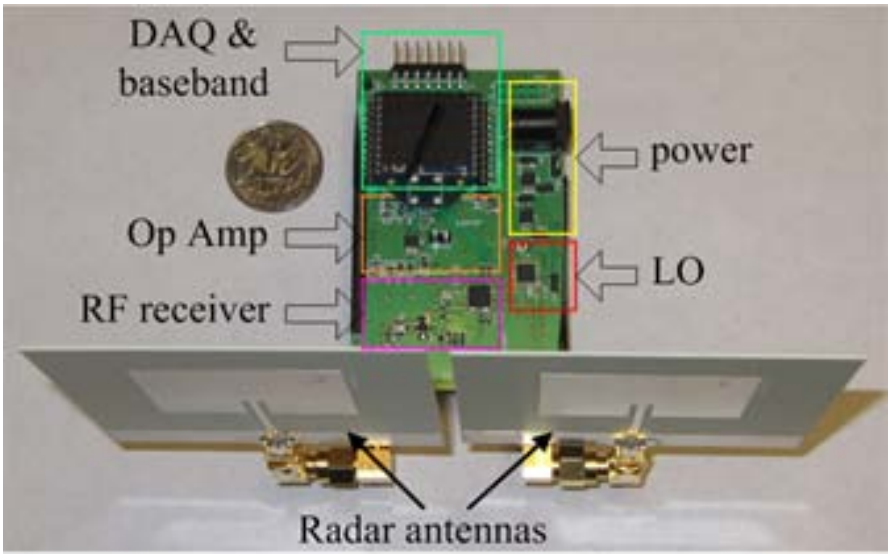

Figure 3.3: The hardware prototype of the Doppler-radar vital-sign-detection system.

3.3.2 Software Design

There are two layers in software for demodulating $I(t)/Q(t)$ and detecting vital signs that take into account the unknown parameters (i.e., A_I, A_Q, ϕ_0, DC_I and DC_Q). The first layer is the modeling layer. With the input from the physical layer, the modeling layer will reconstruct the baseband signal and demodulate phase information. Vital sign related information will be processed in the information layer. In the current prototype, the software part is implemented in Matlab running on PC. The software framework will be elaborated in the next section.

3.4 Our Framework

In this section, we will further present the framework for signal demodulation and vital sign analysis. In our framework, there are two main components, including modeling

layer and information layer (see Fig. 3.4). The input baseband signals, (i.e., $I(t)/Q(t)$), first feed into the modeling layer. After identifying the signal model with five parameters (i.e., A_I, A_Q, ϕ_0, DC_I and DC_Q), baseband signals will be reconstructed (to find $I'(t)/Q'(t)$) and demodulated (to find $x(t)$). The demodulated data will be further analyzed in the information layer.

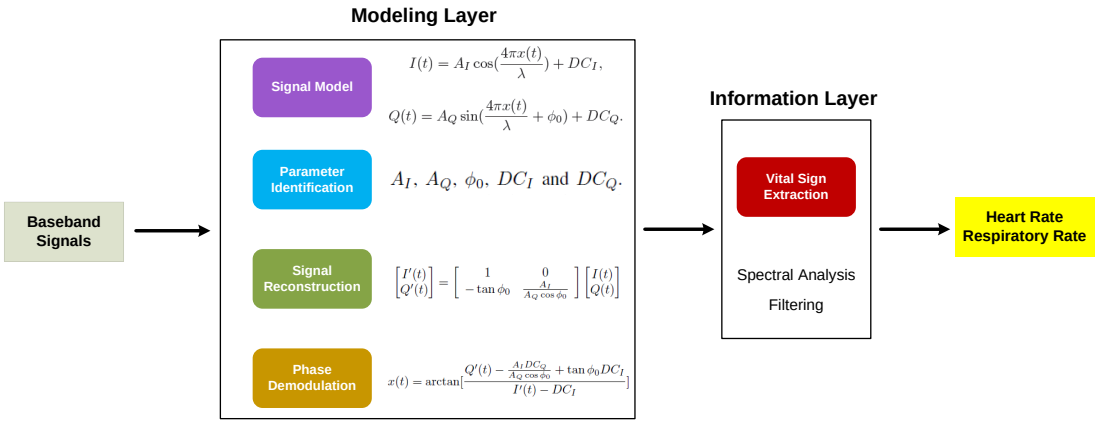

Figure 3.4: The framework of signal demodulation in non-contact vital sign monitoring systems.

3.4.1 Modeling Layer

As shown in Fig. 3.4, the modeling layer consists of building the signal model, identifying model parameters, reconstructing signals and demodulating phase information. From Eq. (3.5) and Eq. (3.6), we can see that there are five unknowns in signal model, i.e., A_I, A_Q, ϕ_0, DC_I and DC_Q. Intuitively there are two potential methods to identify these unknowns. The first one is based on statistical machine learning [Bis06] in artificial intelligence research domain. Given a set of labeled inputs, $x(t)$, statistical learning can build up the relationship between unknowns in the model and input signals. When the relation model is established, it can estimate the values of unknowns with any arbitrary input, $x(t)$. Unfortunately, this method will fail in this application because the Doppler radar signal model is time-varying and non-stationary, which conflicts with the

precondition of most of machine learning methods [RW06].

The second one is to estimate model parameters based on the signal model Eq. (3.5) and Eq. (3.6) with partial pre-calibration. It is assumed that a prior calibration can be performed on the system such that gain imbalance (the ratio of A_I and A_Q) is 1 and phase imbalance (ϕ_0) is 0. Therefore, the *I/Q* channel signals will become:

$$I(t) = A_0 \cos(\frac{4\pi x(t)}{\lambda}) + DC_I, \tag{3.7}$$

$$Q(t) = A_0 \sin(\frac{4\pi x(t)}{\lambda}) + DC_Q. \tag{3.8}$$

In this form, there are only three parameters, A_0, DC_I and DC_Q. Note that pairwise samples, $I(n)$ and $Q(n)$, will stay on a circle whose center is (DC_I, DC_Q) and radius is A_0 because:

$$(I(t) - DC_I)^2 + (Q(t) - DC_Q)^2 = {A_0}^2, \tag{3.9}$$

it is feasible to fit all samples on a circle via least squares optimization [ZRV12] and then identify these three unknowns. However, this method is not suitable for automated monitoring applications since it requires to calibration of gain/phase imbalance. It is impossible to have a pre-fixed calibration for perfect imbalance compensation in practice.

In this work, we attempt to build up the *I/Q* signal model directly from Eq. (3.5) and (3.6) and demodulate the phase accurately.

3.4.1.1 Signal Model

Before looking into the signal model, let us remember the mathematical description for the ellipse. An ellipse is a special case in conic curves which can be described by:

$$F(x, y) = Ax^2 + Bxy + Cy^2 + Dx + Ey + G = 0, \tag{3.10}$$

with one constraint:

$$B^2 - 4AC < 0, \tag{3.11}$$

where A, B, C, D, E, G[1] are six parameters to describe an ellipse. (x, y) are coordinates of points lying on the ellipse, and the formula $F(x, y, A \sim G)$ is defined as the algebraic distance of an arbitrary point (x, y) to a given ellipse.

In contrast to the second method [ZRV12] mentioned above, we build up the *I/Q* signal model without any assumptions and precalibration. With the derivation of Eq. (3.5) and (3.6), it can be proved that a pairwise sample $[I(m), Q(m)]$ from *I/Q* channels stays on an elliptical curve (See **APPENDIX** for the proof in detail). In other words, we can reformulate the signal model identification problem into an ellipse fitting problem.

Given a set of n measurements (I_1, Q_1), (I_2, Q_2), ..., (I_n, q_n), there is an ellipse F_a such that

$$\begin{aligned} \underset{A \sim G}{\arg\min} \quad & \textstyle\sum_{i=1}^{n} \|F(I_i, Q_i)\|_2^2 \\ s.t. \quad & B^2 - 4AC < 0. \end{aligned} \tag{3.12}$$

With the result from Eq. (3.12), we can use Eq. (3.31) - (3.35) in **APPENDIX** to calculate the five parameters in signal model by the values of $A \sim G$.

We can see that Eq. (3.12) is in a form of quadratically constrained least squares (min-ℓ_2) problem. In general, it is a NP-hard problem [BV04] and impossible to obtain global optimal solutions. Fitzgibbon et al. [FPF99] transferred the quadratical inequality constraint, $B^2 - 4AC < 0$, into an equality constraint, $4AC - B^2 = 1$, under the assumption that all the points, (x, y), are close to an ellipse and all distances, $F(x, y)$, are close to zeros.

[1]For simplicity, we will use $A \sim G$ to represent A, B, C, D, E, G

$$\begin{aligned} \underset{A\sim G}{\arg\min} \quad & \textstyle\sum_{i=1}^{n} \|F(I_i, Q_i)\|_2^2 \\ s.t. \quad & 4AC - B^2 = 1. \end{aligned} \tag{3.13}$$

In this way, the formulation in Eq. (3.13) is well-posed and can be solved by Lagrange regularization and eigenvalue decomposition [FPF99]. There are also some research work under the similar assumption above [HF98, SCH12]. However, this method will suffer from the actual scattered data for two reasons. First, when data is noisy and $F(x, y)$ is relatively large, the equality constraint in Eq. (3.13) will not be equivalent to the inequality constraint in Eq. (3.12). Second, it is well-known that ℓ_2 minimization based fitting is sensitive to outlier or sparse measurement errors.

According to compressed sensing theory [Don04] developed in recent years, there are miscellaneous applications indicating that min-ℓ_1 based fitting is robust to outliers or errors than min-ℓ_2 based fitting [CRT06c, WYG09a, XZS12a]. Inspired by this, we consider to use min-ℓ_1 for signal model identification as follows:

$$\begin{aligned} \underset{A\sim F}{\arg\min} \quad & \textstyle\sum_{i=1}^{n} |a_i A + b_i B + c_i C + d_i D + e_i E + G| \\ s.t. \quad & B^2 - 4AC < 0. \end{aligned} \tag{3.14}$$

Eq. (3.14) is a ℓ_1 minimization problem with a non-linear constraint and even harder than the quadratically constrained least square problems in Eq. (3.12). In the following section, we will introduce the method to solve Eq. (3.14) by lower-bound and linear matrix inequality (LMI) relaxation.

3.4.1.2 Model Identification

There are two relaxation steps to solve Eq. (3.14). First, we use the upper bound relaxation to change the objective function. By defining an upper bound distance t_i for each sample (I_i, Q_i), (i.e., $|F(I_i, Q_i)| \leq t_i$), we can have the problem with a linear objective function:

$$
\begin{aligned}
\underset{A\sim G,\mathbf{t}}{\arg\min} \quad & \textstyle\sum_{i=1}^{n} t_i \\
s.t. \quad & F(A \sim G) \leq t_i, \\
& -F(A \sim G) \leq t_i, \\
& t_i \geq 0, i = 1, \cdots, n \\
& B^2 - 4AC < 0.
\end{aligned}
\tag{3.15}
$$

By now, the new problem formulation in Eq. (3.15) is still a non-convex problem and unsolvable. Here we apply LMI relaxation by adding a couple of lifting variables and constraints. More specifically, let $v = [1, A, B, C, D, E, G]^T$ be a basis to build a moment matric, M, by $v \times v^T \succeq 0$:

$$
\begin{aligned}
M &= \begin{bmatrix}
1 & A & B & C & D & E & G \\
A & A^2 & AB & AC & AD & AE & AG \\
B & AB & B^2 & BC & BD & BE & BG \\
C & AC & BC & C^2 & CD & CE & CG \\
D & AD & BD & CD & D^2 & DE & DG \\
E & AE & BE & CE & DE & E^2 & EG \\
G & AG & BG & CF & DG & EG & G^2
\end{bmatrix} \\
&= \begin{bmatrix}
1 & y_1 & y_2 & y_3 & y_4 & y_5 & y_6 \\
y_1 & y_{11} & y_{12} & y_{13} & y_{14} & y_{15} & y_{16} \\
y_2 & y_{12} & y_{22} & y_{23} & y_{24} & y_{25} & y_{26} \\
y_3 & y_{13} & y_{23} & y_{33} & y_{32} & y_{35} & y_{36} \\
y_4 & y_{14} & y_{24} & y_{34} & y_{44} & y_{45} & y_{46} \\
y_5 & y_{15} & y_{25} & y_{35} & y_{45} & y_{55} & y_{56} \\
y_6 & y_{16} & y_{26} & y_{36} & y_{46} & y_{56} & y_{66}
\end{bmatrix} \succeq 0,
\end{aligned}
\tag{3.16}
$$

where

$$
\begin{aligned}
&y_1 = A, y_2 = B, y_3 = C, y_4 = D, y_5 = E, \\
&y_6 = G, \cdots, y_{22} = B^2, \cdots, y_{13} = AC, \cdots.
\end{aligned}
\tag{3.17}
$$

Note that a 48×1 unknown, **y**, and a linear matrix inequality constraint, $M \succeq 0$, are introduced here. As a consequence, we can rewrite the formulation in Eq. (3.15) as:

$$
\begin{aligned}
\underset{\mathbf{y},\mathbf{t}}{\arg\min} \quad & \textstyle\sum_{i=1}^{n} t_i \\
s.t. \quad & F(I_i, Q_i, y_1 \sim y_6) \leq t_i, \\
& -F(I_i, Q_i, y_1 \sim y_6) \leq -t_i, \\
& t_i \geq 0, i = 1, \cdots, n \\
& y_{22} - 4y_{13} < 0 \\
& M \succeq 0.
\end{aligned}
\tag{3.18}
$$

Note that the moment matrix M is symmetric and positive semidefinite, and the formulation in Eq. (3.18) is convex and can be solved by semi-definite programming [BV04]. Therefore, we have a feasible solution to identify the signal model with the five unknown parameters.

3.4.1.3 Signal Reconstruction and Phase Demodulation

With the information of gain imbalance (A_I/A_Q) and phase imbalance (ϕ_0) from the above, we can use Gram-Schmit procedure [Bjo67] to reconstruct $(I(t), Q(t))$ input by the following transformation:

$$
\begin{bmatrix} I'(t) \\ Q'(t) \end{bmatrix} = \begin{bmatrix} 1 & 0 \\ -\tan\phi_0 & \frac{A_I}{A_Q \cos\phi_0} \end{bmatrix} \begin{bmatrix} I(t) \\ Q(t) \end{bmatrix}. \tag{3.19}
$$

Therefore, we can have the reconstructed baseband signal $(I'(t), Q'(t))$:

$$I'(t) = A_I \cos(\frac{4\pi x(t)}{\lambda}) + DC_I, \tag{3.20}$$

$$Q'(t) = A_I \sin(\frac{4\pi x(t)}{\lambda}) + \frac{A_I DC_Q}{A_Q \cos\phi_0} - \tan\phi_0 DC_I, \tag{3.21}$$

and then we can demodulate heart beat and respiration related information, $x(t)$, by the arctangent formula directly:

$$x(t) = \arctan[\frac{Q'(t) - \frac{A_I DC_Q}{A_Q \cos\phi_0} + \tan\phi_0 DC_I}{I'(t) - DC_I}]. \tag{3.22}$$

3.4.2 Information Layer

The information layer receives the demodulated signal, $x(t)$, and performs further processing, such as spectral analysis, band-pass filter and etc. The signal processing will be shown in detail in the experimental part.

3.5 Evaluation

3.5.1 Experimental Setup

In this section, we discuss the evaluation on the proposed non-contact vital sign monitoring system. A 2.4G quadrature Doppler radar system is designed and implemented. As shown in Fig. 3.3, all the RF components, including antenna, oscillator, amplifiers and filters, are fabricated on a printed circuit board. The system is operated at 5V, and the total transmission power is -10dBm (0.1mW). After collection by an on-board DAQ acquisition module, the digital baseband signals are transmitted to a computer for phase demodulation.

For the sake of the comprehensive testing, we design *three* sets of experiments to validate the performance of the system. First, we use the simulated data as a testbench to quantify the residual of ℓ_1 minimization based demodulation algorithm. Second,

an actuator is employed as a controlled subject for the movement detection test. This experiment can examine the system performance from the end-to-end point of view. In the last experiment, we have a pilot study with 15 subjects for detecting real vital signs, including heart rate and respiratory rates, of human beings.

3.5.2 Performance Evaluation with Simulated Data

We developed a set of simulated data to quantify the performance of the proposed demodulation method. The dataset are simulated from known ellipses with noise and outliers. More specifically, the simulated dataset is divided into two classes. One class is the simulated data with outliers only, and the distance from the outlier to the ellipse is up to 50% of the semimajor axis. The other is with outliers and noise, in which signal-noise-ratio is varying from 0.01 to 0.5. In the experiment, we apply the proposed algorithm to perform ellipse fitting on the testbench. Given that the ground truth is known ahead, the performance of demodulation can be quantitatively evaluated. We use Fitzgibbon's ℓ_2 minimization method [FPF99] for comparison.

First, we evaluate the algorithm performance on the outlier dataset. Fig. 3.5(a) and Fig. 3.5(b) show an example of ellipse fitting from the traditional ℓ_2 minimization method and the proposed ℓ_1 minimization method, respectively, where the blue dots present the clean data (zero offset), the red dots present the outliers, the black curve is the fitting result, and the red dash curve is served as ground truth. From this example (15% outliers), we can see that ℓ_1 based algorithm is robust to the red outliers, and the fitting ellipse perfectly matches with the clean data (see Fig. 3.5(b)). In contrast, ℓ_2 based method is affected by the outlier points, and there is an obvious mismatch between the fitting ellipse and the ground truth (see Fig. 3.5(a)).

Furthermore, we evaluate both methods with different outlier percentages, ranging from 5% to 40%. For simplicity, we use the overlap area between fitting ellipse and ground-truth ellipse to evaluate the matching accuracy [HC11]. Fig. 3.6 illustrated two

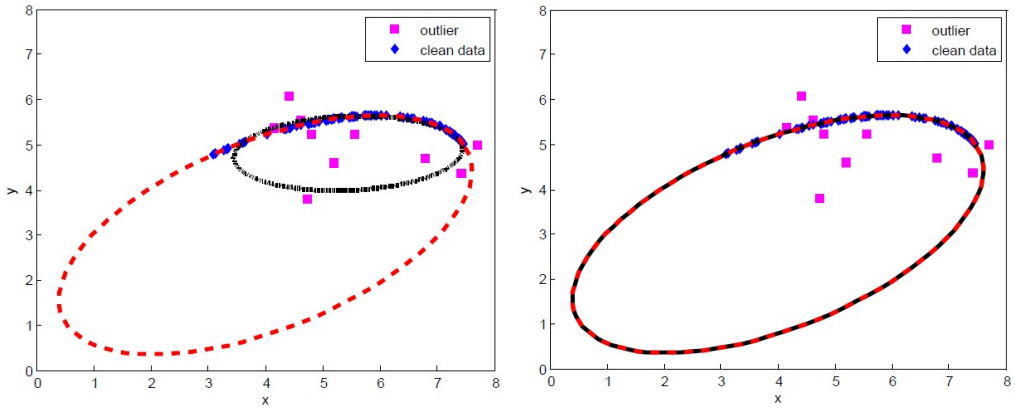

(a) SNR = 0.1 (b) SNR = 0.1

Figure 3.5: An example of fitting results on outlier dataset from two algorithms. The outlier percentage is 15%. Fig. 3.5(a) is the result of ℓ_2 based method, and Fig. 3.5(b) is the result of ℓ_1 based method.

accuracy curves corresponding to these two strategies, respectively. It shows that ℓ_2 based method is sensitive to outliers, and ℓ_1 based method can tolerate the outliers up to 20%.

Second, we test the performance on the data with Gaussian noise. Fig. 3.7 illustrates the stability of ℓ_1 and ℓ_2 algorithms against noise. The SNR is ranging from 0.05 to 0.5. We can see that, with the increase of noise level, both algorithms have more offset compared to the ground truth (the red ellipse). On the other side, ℓ_1 is still significantly better than ℓ_2 in all SNR levels.

3.5.3 End to End Testing with a Controlled Actuator

The second experiment is a real-scenario based experiment to test the performance of non-contact radar sensing system. For accuracy of the evaluation, we use a programmable actuator to obtain controlled motions. As shown in Fig. 3.8, a set of linear actuator (ZABER TNA08A50) and linear translational stage (ZABER TSB28-1) is placed 1m away from the Doppler-radar motion-sensing system. During the experiment, the actuator is programmed to perform a series of standard sinusoidal movements,

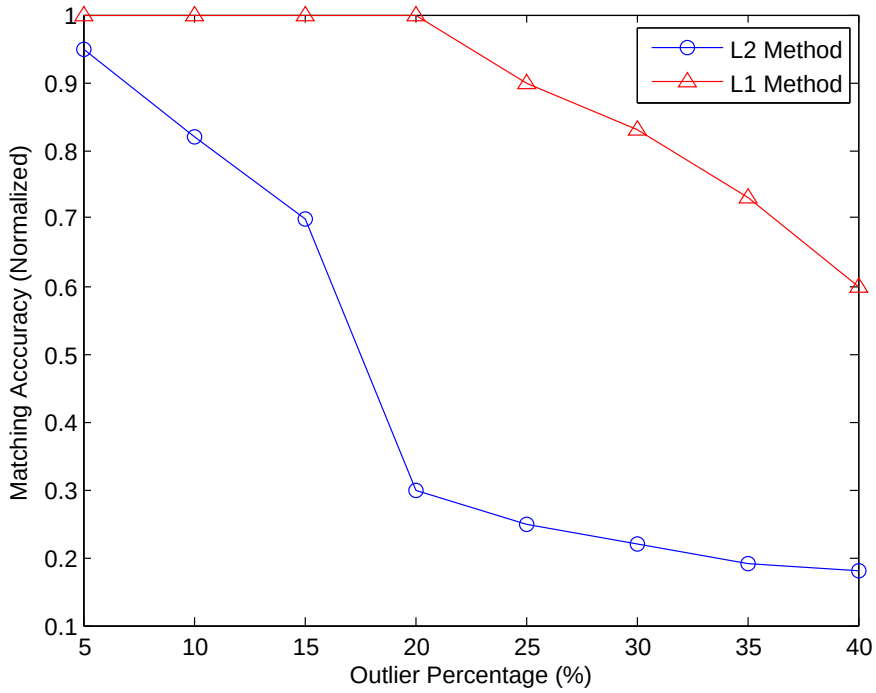

Figure 3.6: Two matching accuracy changing curves with different outlier percentages from ℓ_1 based method and ℓ_2 based method, respectively.

and the radar system will measure and demodulate the actuator motion. To mimic the chest wall movement (by respiration) and heart beat of human beings, the movement amplitude is set from 0.1 cm to 4 cm, and the movement frequency is changing from 0.2 Hz to 2Hz [GWC97, RS89]. In the end, we use the normalized root mean squared error (NRMS) to quantify the measurement error:

$$NRMS = \frac{\sum_{i=1}^{n} dist(i)}{n \cdot A}, \tag{3.23}$$

where $dist(i)$ is the distance from the measured point to the sinusoidal curve, and A is the amplitude of movements.

Fig. 3.10 shows an example of demodulation results, where where blue line denotes the setting motion, and red dots denote the measured motion of our system. Fig. 3.10 illustrates that the measured motion is coherent with the pre-setup motion of linear actuator, and the root mean squared error is less than 1%. Moreover, the residuals on

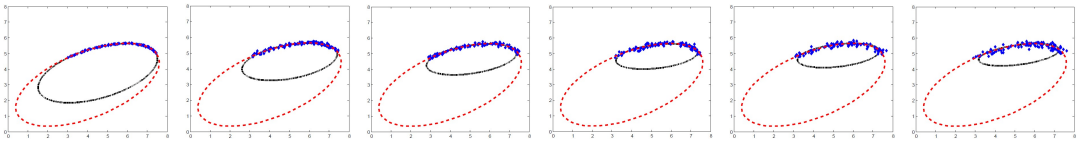

(a) SNR = 0.5 (b) SNR = 0.4 (c) SNR = 0.3 (d) SNR = 0.2 (e) SNR = 0.1 (f) SNR = 0.05

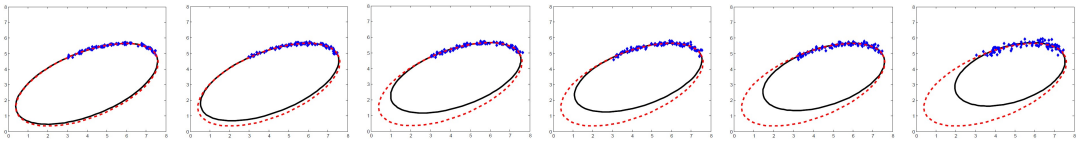

(g) SNR = 0.5 (h) SNR = 0.4 (i) SNR = 0.3 (j) SNR = 0.2 (k) SNR = 0.1 (l) SNR = 0.05

Figure 3.7: Fitting results on noisy dataset from two algorithms. SNR is changing from 0.5 to 0.05. The first row (from (a) to (f)) is the fitting results of the ℓ_2 based method, and the second row (from (g) to (l)) is the fitting results of the ℓ_1 based method. In each figure, the red dash curve is the ground truth and the black solid curve is the fitting curve.

different movement setups are listed in Table 4.2. To clearly represent the residual change with different magnifications and frequencies, we plot the results of Table 4.2 in Fig. 3.9. From this figure, we can see that the averaged measurement error of the Doppler radar sensing system is less 3% on average. In the mean while, it indicates that the measurement error is unrelated to movement frequency but strongly associated with the movement magnitude: the larger the amplitude, the smaller the measurement error.

Based on the end-to-end evaluation results in real scenario, we can safely draw the conclusion that our proposed fitting method outperforms the traditional method in motion sensing applications.

3.5.4 A Pilot Study for Detecting Human Vital Signs

Our last experiment is to detect human vital signs. There are 15 subjects participating the pilot study. As shown in Fig. 3.11, each subject sits in front of the Doppler-radar sensor. Note that the distance between the subject and the radar sensor varies according

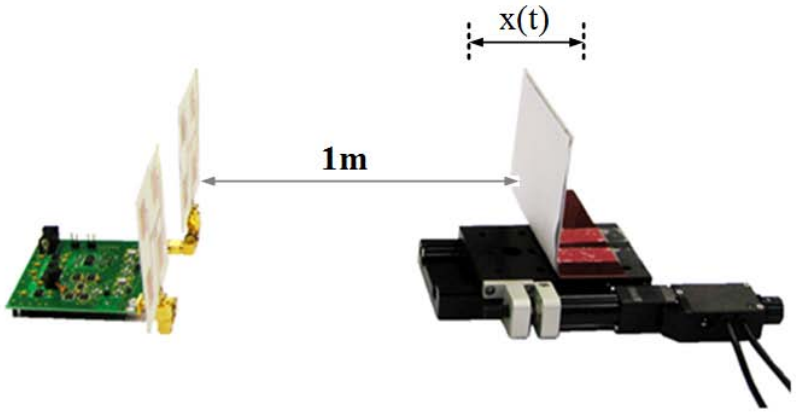

Figure 3.8: Experimental setup for measuring the movement of a controlled actuator

to the sitting position. With the self-calibrating mechanism, there is no need to tune the radar for each subject. For ease of the observation, subjects are under most natural status without talking, coughing or breath-holding. Each measurement lasts 20 seconds, and each subject is tested for 3 times. For the error analysis with ground truth, we use a video camera to record the chest wall movement and a QPS ECG sensor [Car] to record the heart beat, respectively.

Fig. 3.12 shows radar measurements and demodulation results on one subject from the non-contact vital sign monitoring system. Fig. 3.12(a) and Fig. 3.12(b) present *I/Q* and demodulation signals. Note that there is a significant gain imbalance in *I/Q* signals, and heart beat and respiration signals are included in demodulation signals. Fig. 3.12(c) is the spectral analysis result of the demodulation data. We can see that the frequency components on respiration and heart beat are prominent in the spectrum.

Furthermore, we filter the demodulation signal in Fig. 3.12(b) with two band-pass filtering to obtain vital sign signals. Fig. 3.13(a) and Fig. 3.13(b) show the respiration and heart beat signals, respectively. We compare the demodulated respiration signal with the subject's respiration movements and find that they are coherent and synchronized. Fig. 3.13(c) shows the recorded heart beats from the standard ECG device. We can see that the peaks from Fig. 3.13(c) and Fig. 3.13(b) are well aligned with each

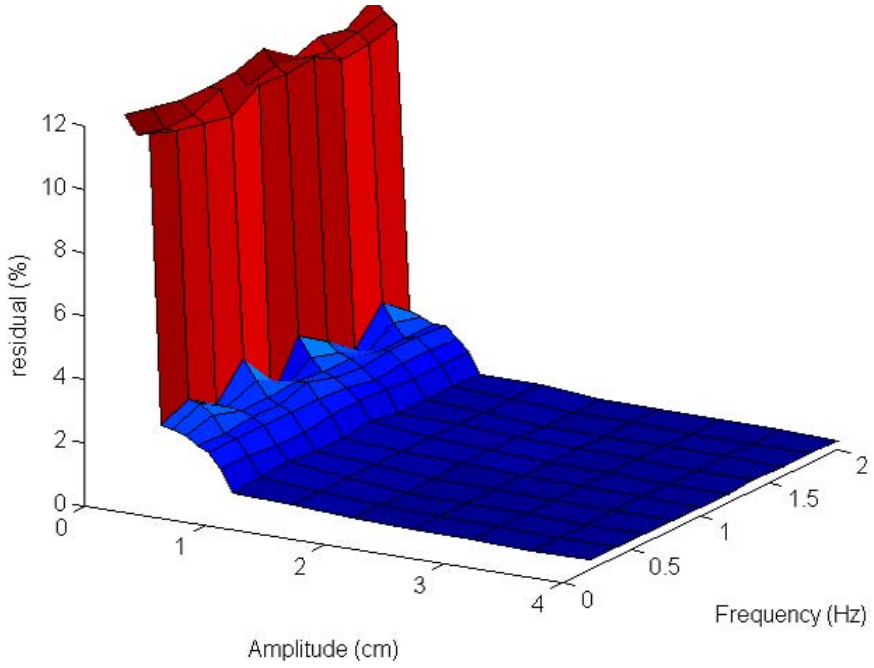

Figure 3.9: The residual surface of movement measurement with different actuator setups.

other. The same results are observed among all 15 subjects, which proves that our self-calibrating radar sensor system can effectively extract vital sign information in a non-contact approach.

3.6 Conclusion and Future Work

In this chapter, we presented a non-contact, self-calibrating vital sign monitoring system using the Doppler radar. We considered the baseband signals in quadrature microwave radar and proposed a framework to automatically analyze $I(t)/Q(t)$, including direct signal modeling, model parameter identification and demodulation. In this work, we formulated signal model identification into a quadratically constrained ℓ_1 minimization problem and solved it with the upper-bound and LMI relaxation.

We performed three sets of experiments to evaluate the performance of our system. We showed the accuracy and stability of our demodulation framework and examined

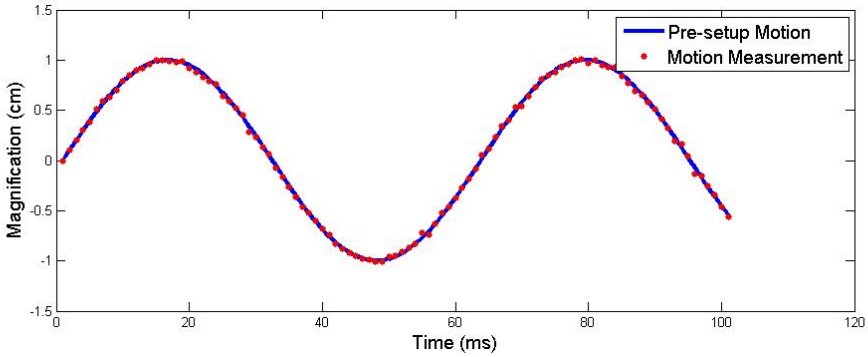

Figure 3.10: The result of sinusoidal motion measurement. The movement frequency is 10Hz, and the magnification is 1cm.

the end-to-end performance with two real-life scenarios. The results showed that our system can effectively detect human vital signs.

In future work, we will consider a pilot study of non-invasive vital sign detection with larger subject group. Moreover, we will try to further improve the demodulation method for more complicated application scenarios, such as accurate vital sign detection when the subject is fast moving.

In this section, we prove that the samples from *I/Q* channels stay on an ellipse. There is a sample [$I(n)$,$Q(n)$] such as :

$$I(n) = A_I \cos(\frac{4\pi x(n)}{\lambda}) + DC_I, \tag{3.24}$$

$$Q(n) = A_Q \sin(\frac{4\pi x(n)}{\lambda} + \phi_0) + DC_Q. \tag{3.25}$$

Based on product-to-sum/sum-to-product formulas, we can transform Eq. (3.25) can be decomposed into:

$$\frac{I(n) - DC_I}{A_I} = \cos(\frac{4\pi x(n)}{\lambda}), \tag{3.26}$$

Table 3.2: The residual of movement measurement with different actuator setups (%)

Frequency (Hz) \ Amplitude (cm)	0.1	0.5	1.0	1.5	2	2.5	3	3.5	4
0.2	12.0	2.3	0.61	0.55	0.43	0.39	0.38	0.32	0.33
0.4	11.8	2.7	0.71	0.54	0.44	0.37	0.35	0.28	0.32
0.6	11.6	2.2	0.77	0.55	0.39	0.37	0.35	0.29	0.31
0.8	11.6	2.6	0.69	0.56	0.43	0.41	0.35	0.31	0.29
1.0	11.7	1.9	0.65	0.56	0.51	0.38	0.36	0.36	0.29
1.2	12.0	2.5	0.78	0.58	0.49	0.39	0.35	0.29	0.29
1.4	11.2	2.2	0.59	0.58	0.49	0.39	0.38	0.29	0.34
1.6	11.5	1.8	0.63	0.52	0.39	0.36	0.38	0.35	0.29
1.8	11.3	2.3	0.63	0.53	0.40	0.39	0.35	0.33	0.32
2.0	11.9	2.1	0.58	0.55	0.41	0.39	0.38	0.34	0.28

$$\frac{Q(n) - DC_Q}{A_Q} = \sin(\frac{4\pi x(n)}{\lambda})\cos(\phi_0) + \cos(\frac{4\pi x(n)}{\lambda})\sin(\phi_0). \tag{3.27}$$

According to trigonometric identities such that:

$$\sin^2(\frac{4\pi x(n)}{\lambda}) + \cos^2(\frac{4\pi x(n)}{\lambda}) = 1, \tag{3.28}$$

we can eliminate $\frac{4\pi x(n)}{\lambda}$ with Eq. (3.26), Eq. (3.27) and (3.28) to get that:

$$\begin{aligned} &\frac{1}{{A_I}^2}I^2(n) - \frac{2\sin\phi_0}{A_I A_Q}I(n)Q(n) + \frac{1}{{A_Q}^2}Q^2(n) \\ &+f_1(\phi_0, DC_I, DC_Q)I(n) + f_2(\phi_0, DC_I, DC_Q)Q(n) \\ &+f_3(\phi_0, DC_I, DC_Q) = 0. \end{aligned} \tag{3.29}$$

Remember that $Ax^2 + Bxy + Cy^2 + Dx + Ey + G = 0$ is a conic curve, and it is an ellipse if and only if $B^2 - 4AC < 0$.

Figure 3.11: The Doppler radar is measuring vital signs from one subject.

From Eq. (3.29), we can get that:

$$B^2 - 4AC = -\frac{4\cos^2(\phi_0)}{A_I A_Q} \leq 0. \tag{3.30}$$

Therefore, we prove that Eq. (3.29) is an ellipse when phase imbalance ϕ_0 is not $(2k+1)\pi/2$. In the case that $\phi_0 = (2k+1)\pi/2$, Eq. (3.29) will degenerate into a line.

Furthermore, if the fitting ellipse $F(x, y) = 0$ is determined, the parameters in *I/Q* signal model can be calculated through:

$$DC_I = \frac{2CD - BE}{B^2 - 4AC}, \tag{3.31}$$

$$DC_Q = \frac{2AE - BD}{B^2 - 4AC}, \tag{3.32}$$

$$A_I = \sqrt{\frac{AE^2 + CD^2 + GB^2 - BDE - ACG}{(B^2 - 4AC)[\sqrt{(A-C)^2 + B^2} - (A+C)]}} \tag{3.33}$$

$$A_Q = \sqrt{\frac{AE^2 + CD^2 + GB^2 - BDE - ACG}{(B^2 - 4AC)[-\sqrt{(A-C)^2 + B^2} - (A+C)]}} \tag{3.34}$$

$$\phi_0 = \frac{1}{2}\cot^{-1}(\frac{A-C}{B}) \tag{3.35}$$

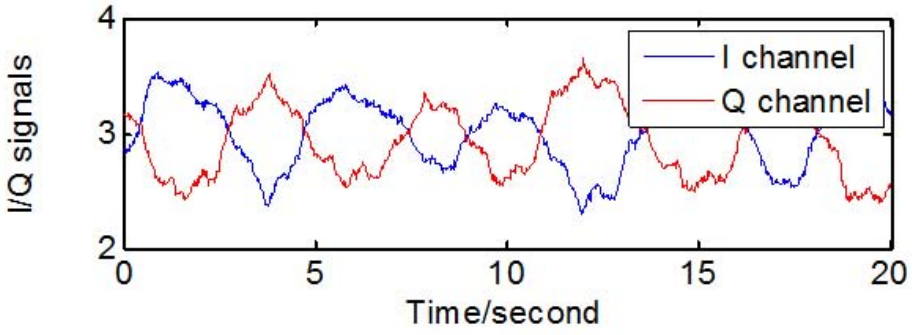

(a) Baseband I/Q Signals

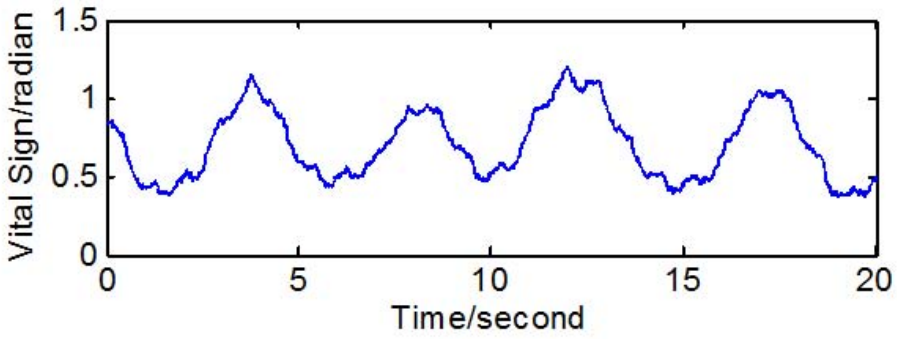

(b) Demodulation Data

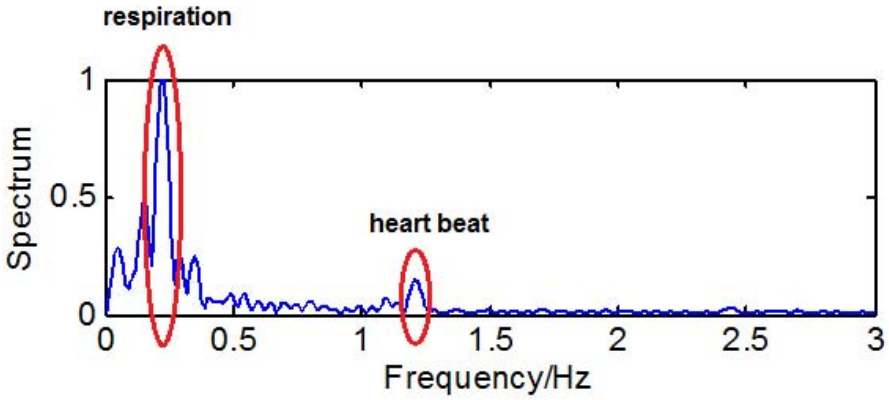

(c) Spectrum on Demodulation Data

Figure 3.12: The measurements with one subject with the non-contact vital sign monitoring system.

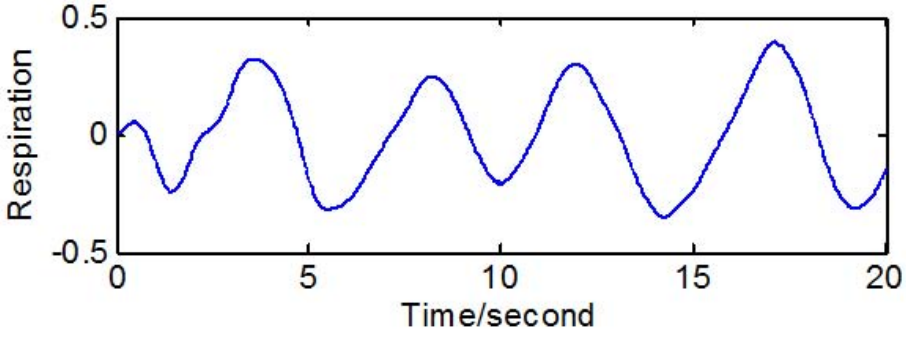

(a) Respiration

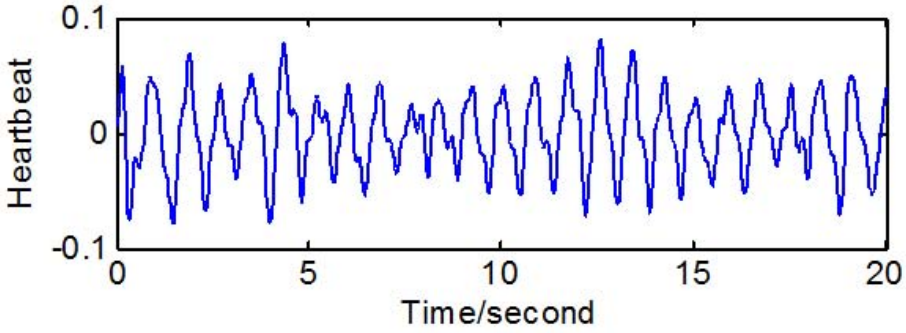

(b) Heart Beat

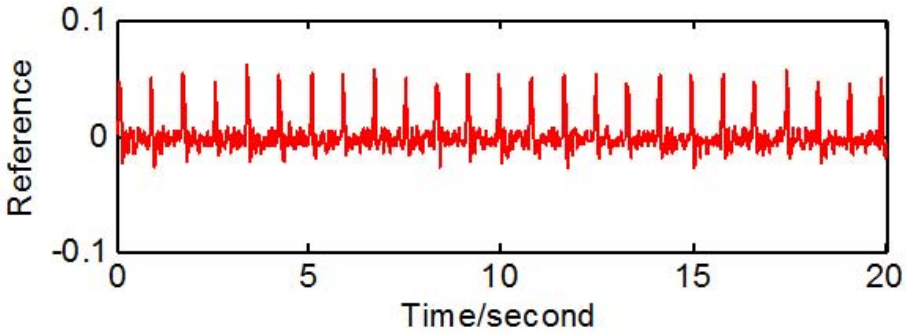

(c) Heart Beat Ground Truth

Figure 3.13: Vital sign signals from demodulated data.

CHAPTER 4

Fall Detection and Prevention

4.1 Introduction

Daily activities and behaviors is a key indicator of human health status. In recent years, a lot of clinical studies prove that human activity and behaviors is highly related to medical diseases, such as obesity [YAY05], autism [LBG00], and cerebral palsy [CCB11]. Therefore, it is important to enable accurate human activity measurements, and proven data can be used as the evidence for medical diagnosis and treatment.

Currently there are two main methods to monitor human activities. One is to deploy the remote sensors (such as camera, radar and infrared) in infrastructure such as parking lots, office buildings and airports. Park and Trivedi [PT05] presented a camera-based tracking system for human movement analysis and privacy protection. Kim and Ling [KL09] investigated the feasibility of classifying different human activities based on micro-Doppler signatures. Han and Bhanu [HB07] developed a hierarchical scheme to automatically detect human movements via infrared sensors. However, one commonly key drawback is that the sensing scope of these remote sensors is immobile and limited due to fixed deployment position. Information may be lost if people leave the field of view of the sensors. Moreover, because of the privacy issue, users will feel uncomfortable when their daily activities are under monitor.

The other method is to attach the inertial sensors (accelerometer, gyroscope and etc.) on the human body to sensor the motor of body parts. Bouten et al. [BKV97] described the development of a triaxial accelerometer and a portable data processing

unit for the assessment of daily physical activity. Najafi et al. [NAP03] introduced a gyroscope-based ambulatory system to detect body postures in elderly persons. With advances in MEMS technologies, inertial sensors have become popular in recent years for human activity sensing and tracking since they are low-cost, miniature and easy to be integrated into personal carry-on devices such as smart phones, watches, and apparel (e.g. shoes, clothes and hats). Figure 4.1 illustrates a number of examples of on-body sensing devices integrated with inertial sensors. We can see that different devices will be deployed on different locations on the human body accordingly. Therefore, the activity signals captured by inertial sensors are highly dependent on both the human activity and the location where the sensors are worn. In other words, it is highly possible that the signals may be totally different when a person performs the same activity with sensors on different locations. Therefore, any misplacement or displacement might lose the sensing accuracy and make the analysis completely incorrect [ASV11].

Figure 4.1: Examples of on-body inertial sensing devices for human activity monitoring and recognition: 1) Nike+; 2) BodyMedia; 3) Healthset; 4) Basis Band; 5) Fitbit.

Based on this observation, it is difficult to understand the inertial sensor signal without any *priori* information. In fact, researchers have been developing techniques to either extract location information from the captured activity signals or take advantage of

the sensor location information as a *priori* information to achieve better activity recognition performance. For example, Vahdatpour et al. [VAS11] developed a SVM-based approach to identify the sensor location on the human body when people walk. Long et al. [LYA09] customized the activity recognition algorithm to specific sensor locations to improve the performance of the recognizer. Among all these existing techniques, the common point is that they treat sensor localization and activity recognition as two separate problems assuming the other part information is known. Unfortunately, either of them will be available in practical applications. In this chapter, we argue that the sensor location information and the activity signals are intertwined and can be solved as one problem.

We proposed the solution to co-recognize human activity and sensor location in a single framework, which is not necessary to have any priori information about sensor and human activity. Specifically, our framework uses sparse signal theory, which enables to reconstruct the signal with limited or incomplete samples if the signal has *sparsity* in some transformation domain [Don06]. Here, we prove that human activity signals captured by wearable inertial sensors are indeed sparse, and then take advantage of this sparsity information to classify activity signals and recognize where the sensor is located on the human body simultaneously. Based on our experiments, our method can recognize 14 activities and 7 on-body locations with 87.72% recognition accuracy on average.

The remainder of this chapter is organized as follows. In Section 4.2 we briefly introduce the theory of sparse signals and review some existing work on human activity recognition based on the theory. Then, we describe our human activity and sensor location co-recognition framework in Section 4.3. The experimental results and analysis are presented in Section 5.4. Finally, we outline the future work and conclude the chapter in Section 4.5.

4.2 Preliminary and Related Work

4.2.1 Sparse Signals and ℓ_1 Minimization

Sparse signal processing (or compressed sensing) [Don06] is a ground-breaking signal processing procedure developed recent years. It has been widely applied in many research domains such as communications, medical image processing and computer graphics due to its capability of accurate signal reconstruction with lower sampling rate claimed by Nyquist-Shannon sampling theorem [CRT06a].

Suppose that $x \in \mathbb{R}^n$ is a vector of unknown variables, $y \in \mathbb{R}^m$ is the available measurements, and $A \in \mathbb{R}^{m \times n}$ is the data matrix to describe the relation between x and y. Then, we have:

$$y = Ax. \tag{4.1}$$

In many real-world applications, the number of unknowns, n, is more than the number of measurements, m, i.e. $n > m$. In such cases, Eq. (4.1) represents an underdetermined system, and x can not be uniquely reconstructed from the data matrix A and the measurements y. However, in situations where x is sparse enough, we can reconstruct x with the ℓ_0 sparsity formulation from:

$$\begin{aligned} &\min_{x \in \mathbb{R}^n} \| x \|_{\ell_0} \\ s.t. \quad &y = Ax. \end{aligned} \tag{4.2}$$

Eq. (4.2) is a determined system and has stable solution. However, Eq. (4.2) is intractable because it is an NP-hard problem [Nat95a]. The traditional heuristic to approximate the sparsity ℓ_0 is to use the minimal energy ℓ_2:

$$\begin{aligned} &\min_{x \in \mathbb{R}^n} \| x \|_{\ell_2} \\ s.t. \quad &y = Ax. \end{aligned} \tag{4.3}$$

It is well-known that ℓ_2 is a least square formation and can be efficiently solved. However, the energy minimization ℓ_2 is not necessarily equivalent to the sparsity ℓ_0 in

most cases. In 2006, the authors of [CRT06a] proved that the solution of Eq. (4.2) is highly the same as the solution with the ℓ_1 minimization.

$$\begin{aligned} & \min_{x \in \mathbb{R}^n} \| x \|_{\ell_1} \\ s.t. \quad & y = Ax. \end{aligned} \tag{4.4}$$

It has been proved that this ℓ_1 minimization can be formulated as a convex problem [Don06]. In such case, the optimization problem is well-posed and can be solved in polynomial time.

4.2.2 Sparse Signals for Pattern Recognition

One important application of sparse signals is pattern recognition and classification. In recent years, it has been applied successfully to many pattern recognition problems including face recognition [WYG09b], speech recognition [GVH07], and iris recognition [PPC11]. The formulation of sparse signal based classification strategy is relatively straight forward. Consider a pattern recognition problem with K different classes. Each class k has n_k training samples, each having m attributes. In total, there are $n = \sum_{i=1}^{K} n_i$ training samples. We can collect all these training samples to form a matrix A with m rows and n columns as follows:

$$\begin{aligned} A &= [\underline{A_1}, \underline{A_2}, \cdots, \underline{A_i}, \cdots, \underline{A_k}] \\ &= [\underline{a_{11}, a_{12}, ..., a_{1n_1}}, \underline{a_{21}, a_{22}, ..., a_{2n_2}}, \cdots, \\ &\quad , \cdots, \underline{a_{i1}, a_{i2}, ..., a_{in_i}}, \cdots, \underline{a_{k1}, a_{k2}, ..., a_{kn_k}}], \end{aligned} \tag{4.5}$$

where a_{ij} is the j-th training sample from class i.

Following Eq. (4.1), any given unknown input $y \in \mathbb{R}^m$ can be represented as a linear span of training sample matrix $A \in \mathbb{R}^{m \times n}$ as:

$$y = x_1 a_{11} + x_2 a_{12} + \cdots + x_n a_{kn_k}, \tag{4.6}$$

where $x_1, x_2, \cdots, x_n$ are a sparse set of weights.

Under this formulation, the class membership of y, which is encoded as the sparsest solution of the underdetermined system given in Eq. (4.1) can be found by solving Eq. (4.4).

4.2.3 Related Work

There are some existing research work on using sparse representation for human activity analysis. Yang et al. [YJS09] used 8 motion sensing motes distributed on the human body to recognize 12 different human activities. Liu et al. [LYC09] adopted a similar strategy to recognize human activities captured by camera videos. Compared to these existing studies, our work differs in the following aspects:

1. Sensing technology: Instead of using video cameras [LYC09], we use inertial sensors (accelerometer and gyroscope) attached on the human body to collect human activity signals;

2. Sensing strategy: Rather than distributing multiple sensor nodes to cover the entire body as in [YJS09], we use only one single sensor node on the body to recognize human activity. We believe this sensing strategy is less intrusive and can be applied to a much wider range of real-world applications;

3. Sensor location: The work in [YJS09] requires that the sensor nodes are fixed in some specific locations. Any misplacement of the sensor nodes will make the recognition fail. In comparison, our method does not have this limitation and enables the co-recognition of human activity and sensor location in one single step.

A preliminary version of this work has appeared [XZS12d]. Compared to previous work, we include a further study and discussion of the algorithm performance in this chapter. Specifically, there are two new contributions. First, we investigated algorithm *robustness* on feature dimension reduction. In this chapter, we evaluate the algorithm

robustness from two aspects: classification *accuracy* and classification *stability*. The detailed analysis of this part is addressed in Section 4.4.4. Second, we compared our algorithm with two most used classification methods, nearest neighbor (NN) and nearest subspace (NS), to justify its advantage. The comparison study includes three aspects: classification accuracy, classification stability and robustness on feature dimension reduction. The experimental results proved the advantage of our method and discussed the applicable conditions (see Section 4.4.6). Note that we use the same dataset on evaluation for the sake of consistency with previous work.

Figure 4.2: The three important components of our sparse signal based framework

4.3 Our Framework

In this section, we present our proposed framework for co-recognizing human activity and on-body sensor location. As shown in Figure 4.2, our framework consists of three important components: feature extraction, sparse representation via ℓ_1 minimization, and Bayesian sparse signal based classification. We will describe the details of all these components in this section.

4.3.1 Feature Extraction

There are many existing studies focusing on exploring the best features that can be extracted from human activity signals. Following previous work [ZS12], we extract statistical features in motion signals, such as mean, standard deviation and nonnegative entropy, to represent human activities. These parameters index a family of probability distribution and describe the characteristics of a population. In this chapter, we use

Table 4.1: Selected Features and Their Definitions

No.	Statistical Feature	Definition
1	Arithmetic Mean	The DC component (average value) of the signal
2	Median	The median signal value
3	Stand Deviation	Measure of the distribution of the signal
4	Variance	The square of the standard deviation
5	Root Mean Square	The quadratic mean value of the signal
6	Mean Derivatives	The average value of the first order derivatives of the signal over the window
7	Skewness	The degree of asymmetry of the sensor signal distribution
8	Kurtosis	the degree of peakedness of the sensor signal distribution
9	Interquartile Range	Measure of the statistical dispersion, being equal to the difference between the 75th and the 25the percentiles of the signal over the window
10	Zero Crossing Rate	The total number of times the signal changes from positive to negative or vice versa
11	Mean Crossing Rate	The total number of times the signal change from below average to above average or vice versa
12	Pairwise Correlation	Correlation between two axes of each sensor and different sensors

12 statistical features listed in Table 4.1 because they these features been proven to be useful in classifying human activities and other related pattern recognition problems by existing studies [ZS11b]. All these features are extracted from both accelerometer and gyroscope signals. In total, 64 features for each segment are extracted and denoted as $x \in \mathbb{R}^{64}$. Also, note that every feature in the vector is independent of others.

4.3.2 Sparse Representation via ℓ_1 Minimization

We follow the formulation described in Section 4.2 to construct the data matrix A. Specifically, we collect n samples from activity i and sensor location j. For each sample, we extract features described in the previous subsection to form a feature vector a. Then a feature matrix A_{ij} can be constructed as:

$$A_{ij} = [a_1, a_2, \cdots, a_n]. \tag{4.7}$$

In this way, we build the data matrix A covering all K activities and L locations as:

$$A = [A_{11}, A_{12}, \cdots, A_{KL}]. \tag{4.8}$$

As described in Section 4.2, any given test sample y from unknown activity and

location can be represented in terms of the matrix A as

$$y = A_{11}x_{11} + A_{12}x_{12} + \cdots + A_{KL}x_{kl}, \tag{4.9}$$

where $x = [x_{11}, x_{12}, \cdots, x_{kl}]$ is the sparse representation of y w.r.t. matrix A, and the coefficient x_{ij} is referred as feature index for feature matrix A_{ij}. In such case, x can be found via the ℓ_1 minimization formulated in Eq. (4.4).

4.3.3 Bayesian Sparse Signal Based Classification

Given the sparse representation x of the test sample y, we can identify its activity class membership i and location class membership j altogether by computing the residual values between y and each feature matrix A_{ij} defined as:

$$\mathbf{residual}_{ij} = \|y - A_{ij}x_{ij}\|_2, \tag{4.10}$$

the lower the residual value is, the more similar y is to feature matrix A_{ij}. Therefore, y is classified as the activity class C and sensor location class S that produces the smallest residual:

$$\{C, S\} = \mathbf{arg}\min_{ij} \ \mathbf{residual}_{ij}. \tag{4.11}$$

Let $P(i, j|C, S)$ be the probability that the test sample y is classified as activity i and sensor location j when the true activity class is C and true sensor location class is S. Since the residual value is a measure of the similarity between y and the feature matrix A_{ij}, the lower the residual is, the higher the probability that the classified activity class i and location class j will be the same as the true activity class C and true location class S. Therefore, we can model the probability $P(i, j|C, S)$ using the residual values as:

$$P\left(i,j|C,S\right)=1-\frac{residual_{ij}}{\sum_{i=1}^{K}\sum_{j=1}^{L}residual_{ij}}. \tag{4.12}$$

Based on the sum rule of probability theory, the probability of y classified as activity i when the true activity class is C can be derived by summing up the probability at each sensor location from

$$P\left(i|C\right)=1-\frac{\sum_{j=1}^{L}residual_{ij}}{\sum_{i=1}^{K}\sum_{j=1}^{L}residual_{ij}}, \tag{4.13}$$

and the test sample y is classified as activity class C^* that has the highest probability:

$$C^*=\mathbf{arg}\max_{i}\ P\left(i|C\right). \tag{4.14}$$

Similarly, the probability of y classified as location j when the true location class is S is calculated by summing up the probability over all activity classes from

$$P\left(j|S\right)=1-\frac{\sum_{i=1}^{K}residual_{ij}}{\sum_{i=1}^{K}\sum_{j=1}^{L}residual_{ij}}, \tag{4.15}$$

and the test sample y is classified as sensor location class S^* that has the highest probability

$$S^*=\mathbf{arg}\max_{j}\ P\left(j|S\right). \tag{4.16}$$

4.4 Experiments and Evaluation

4.4.1 Experimental Setup and Dataset

We ran a pilot study in a laboratory environment to evaluate the performance of our proposed approach. The dataset is collected using an customized human motion sensing node, called a TelosB mote [GLJ09]. As shown in Figure 4.3, the size of the TelosB mote is 1.267 inch by 2.580 inch, and it includes a tri-axial accelerometer and a bi-axial

gyroscope (i.e. *five* data channels). For each channel, the signal sampling rate is 50 Hz, and all the samples are stored in an on-board SD card.

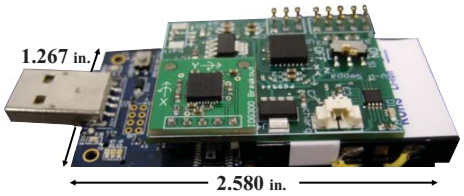

Figure 4.3: TelosB mote for human motion sensing

We collected the data from 3 male subjects whose ages are 25, 28, and 33 respectively. Each subject performed 14 different activities including: 1) stand to sit ; 2) sit to stand ; 3) sit to lie ; 4) lie to sit ; 5) bend to grasp ; 6) rising from bending; 7) kneeling right; 8) rising from kneeling; 9) look back; 10) return from look back; 11) turn clockwise; 12) step forward; 13) step backward; and 14) jumping. Meanwhile, the subjects were asked to wear the sensing device at 7 different locations during their performance. These locations are: a) waist; b) right wrist; c) left wrist; d) right arm; e) left thigh; f) right ankle; and g) left ankle. Therefore, we have 98 combinations of activity and sensor location in total. For each location, each subject performed each activity for 10 trials.

After data collection, we extract features listed in Table 4.1 from each data unit. Our sensor node has *five* data channels, and we can extract 64 features from each data unit.

4.4.2 Sparsity of Human Activity

Based on the discussion in Section 4.2.1, sparse representation can perform accurate recognition and classification based on one important prerequisite: *the representation x of y should be a sparse vector in the space spanned by the training samples A.* Unfortunately, few works prove the sparsity of their problems before using this principle,

either theoretically or empirically. For the sake of avoiding blind decisions, we did the preliminary experiments to investigate the sparsity of human activities.

Without the loss of generality, we randomly selected 30 samples from a single activity, and each sample has 30 randomly selected features. In this way, we can form a sample matrix $A_1 \in \mathbb{R}^{30\times30}$. We also built $A_2 \in \mathbb{R}^{30\times30}$ with 3 human activities and $A_3 \in \mathbb{R}^{30\times30}$ with 9 activities. Note that in all these sample matrixes, column space consists of samples, and the row space is based on the features. Similar to [SEH11], we generated a Gaussian random matrix $G \in \mathbb{R}^{30\times30}$ and performed SVD [GR70] on A_1, A_2, A_3 and G respectively to evaluate the sparsity of human activity. All their singular value profiles are illustrated in Figure 4.4. It indicates that compared to G, A_1, A_2 and A_3 are low-rank since their SVD profiles have significant downtrend compared to G. Knowing that all features are statistically independent (see Section 4.3.1), low-rank should be caused by column space, which means that the sample space is overcomplete. This is an experimental indiction that the training samples A are a sparse set. Specifically, comparing A_1 with A_2 and A_3, we can see that the sample space from the same activity class (i.e. A_1) has a higher degree of sparsity.

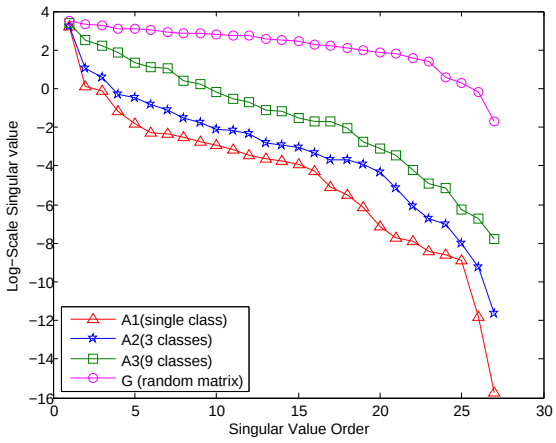

Figure 4.4: The log-scale singular values of the sample matrix A_1, A_2 and A_3. We also use Gaussian random matrix G for comparison.

4.4.3 Classification Performance Evaluation

For this part, we evaluate the classification performance of our framework. Our evaluation is based on three metrics: (1) the classification accuracy of co-recognition of activity and sensor location based on Eq. (4.11); (2) the classification accuracy of activity based on Eq. (4.14); and (3) the classification accuracy of sensor location based on Eq. (4.16). For evaluation, we adopt a 10-fold cross validation strategy. Specifically, we divide the whole dataset into 10 sets. At one time, 5 sets are used to build the data matrix A and the remaining 5 sets for testing. The whole procedure iterates 10 times.

There are two important aspects in algorithm evaluation. One is the classification *accuracy*. Given large number of testing inquiries, the algorithm should offer the correct responses with high probability. The other aspect is the classification *stability*. If the training and testing datasets are changed, the recognition result should vary slightly from the average rate.

Table 4.2 shows the evaluation results in terms of the above three metrics. As shown, metric (1) achieves an 87.42% precision value and an 87.93% recall value. For metric (2) and (3), it is interesting to see that with Bayesian fusion, the classification accuracy is improved. Specifically, for activity recognition, the precision and recall reach 88.79% and 89.21%. For location recognition, both the precision and the recall are higher than 96%. For *stability*, we observe that the standard deviation of metric (1) is as low as 1.26% (the mean of precision and recall variation). After Bayesian fusion, both metric (2) and matric (3) have better robustness. As shown in Table 4.2, the variation of metric (2) is 1.25% and 1.02% for precision and recall variation. For metric (3), the variation is always less than 0.5% in general.

To take a closer look at the classification results, Table 4.3 and 4.4 show two confusion tables with respect to activity classification (metric (2)) and sensor location classification (metric (3)), respectively. In Table 4.3, we notice that activity 7) *kneeling right* and activity 8) *rising from kneeling* are most often confused. Although these two ac-

Table 4.2: Classification performance evaluated by three metrics

	Activity&Location (%) metric (1)	Activity (%) metric (2)	Location (%) metric (3)
Precision	87.42 ± 1.43	88.79 ± 1.25	96.02 ± 0.43
Recall	87.93 ± 1.10	89.21 ± 1.02	96.24 ± 0.38

Table 4.3: Confusion Table of Recognition on 14 Human Activities

	1	**2**	**3**	**4**	**5**	**6**	**7**	**8**	**9**	**10**	**11**	**12**	**13**	**14**	**Total**	**Recall**
1	79	1	0	1	0	0	0	0	0	0	0	1	0	2	84	94%
2	3	79	0	0	0	0	0	0	0	2	0	0	0	0	84	94%
3	1	1	74	8	0	0	0	0	0	0	0	0	0	0	84	88%
4	2	2	3	72	0	1	2	0	0	0	2	0	0	0	84	86%
5	0	0	0	1	78	0	0	0	0	1	0	0	1	2	84	93%
6	0	0	0	0	0	78	0	0	1	1	2	1	0	1	84	93%
7	0	0	0	0	0	0	72	8	0	0	2	1	1	0	84	86%
8	0	0	0	0	1	0	8	67	0	0	1	4	2	1	84	80%
9	0	0	0	0	1	0	0	0	78	2	3	0	0	0	84	93%
10	1	0	0	0	0	2	0	0	4	76	1	0	0	0	84	90%
11	1	0	0	0	0	0	2	0	1	2	71	2	5	0	84	85%
12	0	0	0	2	0	0	4	0	0	0	1	74	3	0	84	88%
13	0	0	0	0	0	0	2	4	1	2	0	9	66	0	84	79%
14	0	0	0	0	0	0	0	0	0	0	0	0	0	84	84	100%
Total	87	83	77	84	80	81	100	79	85	86	83	92	78	90		
Precision	91%	95%	96%	86%	98%	96%	72%	85%	92%	88%	86%	80%	85%	93%		

tivities are a pair of complementary processes and visibly different from each other in the *time domain*, our algorithm describes the human activity signal in a statistical way and removes the temporal information in the data. Therefore, complementary processes should share many features in the *space domain*. As for sensor location classification, as illustrated in Table 4.4, most precision and recall values are more than 98%. However, location e) *Left Thigh* and location f) *Right Ankle* are confused with each other the most. Specifically, the corresponding accuracy is around 92%. It indicates that the selected features described in Section 4.3 can not reliably distinguish the two cases. We could consider this issue to enhance the algorithm performance in future work.

Table 4.4: Confusion Table of Recognition on 7 On-Body Sensor Locations

	a	**b**	**c**	**d**	**e**	**f**	**g**	**Total**	**Recall**
a	166	1	0	0	1	0	0	168	99%
b	0	163	2	1	1	1	0	168	97%
c	2	1	158	0	4	1	2	168	94%
d	0	0	1	163	3	1	0	168	97%
e	4	0	0	0	154	10	0	168	92%
f	2	1	1	0	5	157	2	168	93%
g	0	0	0	0	0	0	168	168	100%
Total	174	166	162	164	168	170	172		
Precision	95%	98%	98%	99%	92%	92%	98%		

4.4.4 Robustness on Feature Dimension Reduction

In this experiment, we investigate the impact of feature dimension on performance of our framework. As mentioned before, in total we extract 64 features. We start from 60 features and reduce the number of features by the decrement 5. Figure 4.5 shows the averaged misclassification rates for each feature dimension in terms of the three classification metrics. We can see that the misclassification rate of co-recognition increases from 13% to 39% while the feature dimension decreasing from 64 to 30. Furthermore, it indicates that 55 is the significant turning point, where the misclassification rates increase greatly (more than 10%) when the feature dimension is less than 55 (from 55 to 50).

In addition to the classification accuracy (see Fig. 4.5), we also examined the classification stability of our framework with feature dimension. For simplicity of the presentation, we investigated the performance on co-recognition of human activity and sensor location (metric (1)). As shown in Fig. 4.6 (the blue error bar), we observe the variation of the misclassification rate also increases with a decrease of the number of features. This implies that the feature number has significant impact not only on

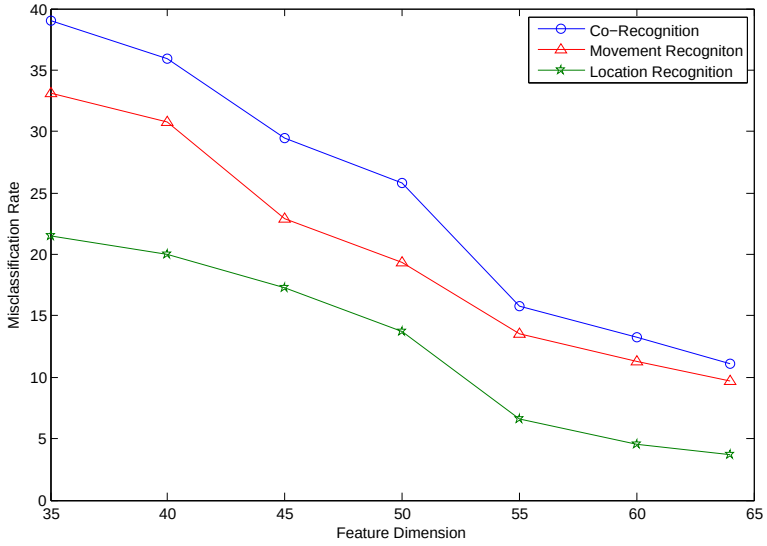

Figure 4.5: Impact of Feature Dimension on Classification Accuracy

the classification accuracy, but on the classification stability. Specifically, the variation increases to 5% when the feature number drops to 35.

More specifically, to examine the robustness of our framework in terms of different features, we randomly selected 55 features out of 64 as an example and evaluated the framework for 10 times. Table 4.5 shows the results. As shown, it is interesting to see that our compressed sensing-based framework is not sensitive to the specific features selected, with the standard deviation of the performance less than 1.41% for all cases.

Table 4.5: Impact of Features on Classification Performance

	Activity&Location (%)	Activity (%)	Location (%)
Precision	83.14 ± 1.41	86.01 ± 1.15	92.73 ± 0.53
Recall	83.78 ± 1.27	87.15 ± 0.94	93.24 ± 0.47

4.4.5 Comparison Between ℓ_1 and ℓ_2

As stated in Section 4.2, ℓ_1 is a better heuristic for sparsity optimization than ℓ_2. In this section, we empirically validate this point and compare the classification perfor-

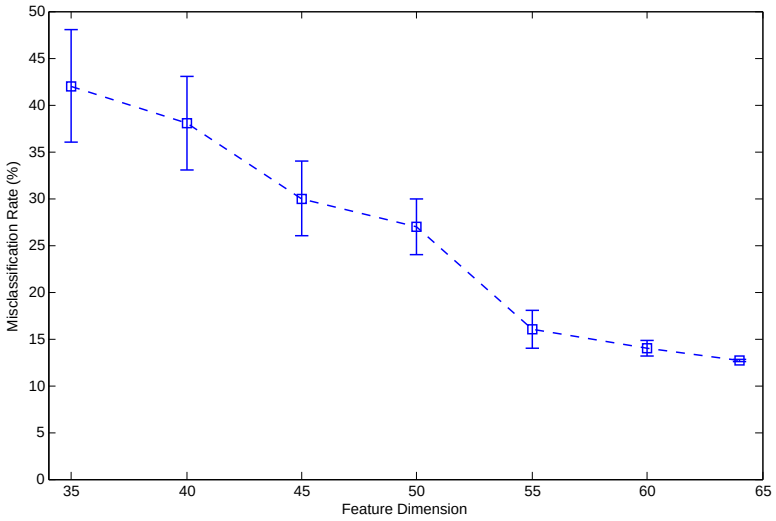

Figure 4.6: Impact of Feature Selection on Classification Stability of metric (1)

mance between ℓ_1 and ℓ_2 optimization strategies. As an example, Figure 4.7 shows the solutions from both ℓ_1 and ℓ_2 optimization with one test sample from activity 7 (kneeling right) at location d (right arm). As illustrated, the solution from ℓ_1 is quite sparse has few significantly large components. Moreover, the maximal spike marked by the red circle is associated with the training samples belonging to the same activity class and sensor location class. In comparison, the solution from ℓ_2 has few significant components and many small components. The spikes are dense and distributed over all activity and sensor location classes (see Figure 4.7).

For clarity of the presentation, we augment this result in the residual computation. Figure 4.8 illustrates the corresponding residual values between the test sample and all 98 classes defined by Eq. (4.10) for both ℓ_1 and ℓ_2. As shown in the figure, the class membership of the test sample can be easily found by the minimal residual (pointed by the red arrow) for the ℓ_1 optimization strategy. For ℓ_2, although the minimal residual also corresponds to the true class, the difference between the minimal residual and the residual values of other classes is not significant in this example.

Also, we compare the classification performance between ℓ_1 and ℓ_2. Table 4.6 shows the results in terms of the recognition rates. As shown, ℓ_1 outperforms ℓ_2 across

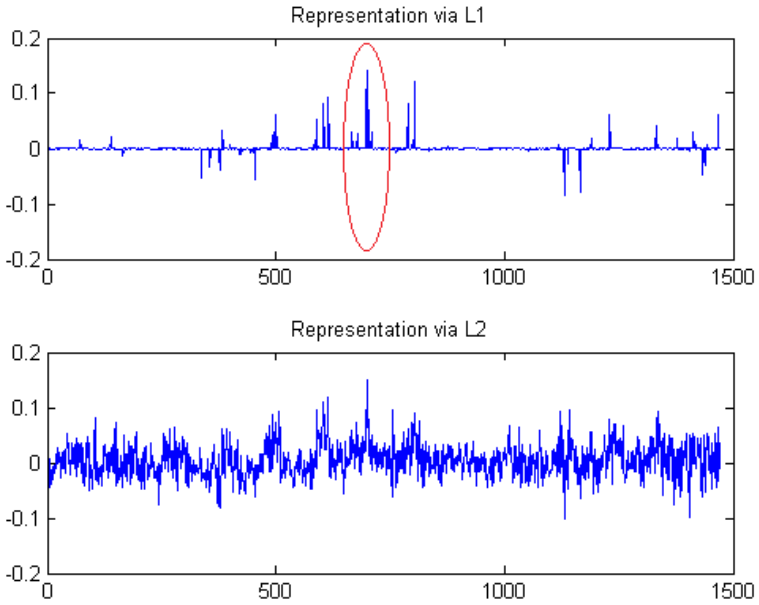

Figure 4.7: Solutions of ℓ_1 and ℓ_2 Optimization Strategies

all three metrics consistently in terms of both recognition accuracy and stability. It is worth emphasizing that the enhancement from ℓ_1 compared to ℓ_2 has stronger scalability: the larger the scale, the greater is the benefit. Based on the indication in Figure 4.7, it is not surprised that ℓ_1 outperforms ℓ_2 overwhelmingly in terms of both accuracy and stability. Specifically, the co-recognition classification accuracy could be improved by 20.75% with ℓ_1 optimization. Correspondingly, the gain of stability from ℓ_1 optimization is $3.17X$ on average.

Table 4.6: Classification performance comparison of ℓ_1 and ℓ_2

	Activity&Location metric (1)		Activity metric (2)		Location metric (3)	
	mean	std	mean	std	mean	std
$\ell_1(\%)$	87.72	1.26	89.00	1.13	96.13	0.41
$\ell_2(\%)$	72.65	5.46	80.94	4.28	85.32	1.31
$\frac{\ell_1-\ell_2}{\ell_1}$	20.75%	3.17X	9.95%	2.78X	11.25%	2.20X

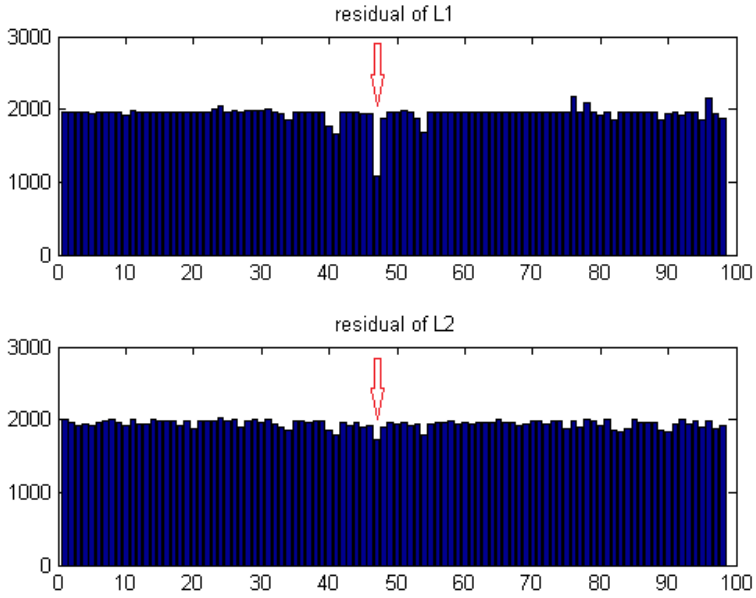

Figure 4.8: Residuals of 98 Classes of ℓ_1 and ℓ_2 Optimization Strategies

4.4.6 Sparse Representation (SR) Based Classifier v.s. Two Classical Methods

As a last experiment, we show the advantage of our method with respect to different feature dimensions compared to two classical classification methods: Nearest-Neighbor (NN) based classifier [CH67] and Nearest-Subspace (NS) based Classifier [BHK97]. For simplicity of the presentation, we only show the results on classification accuracy (the mean of precision and recall) here. Figure 4.9 illustrates the average classification accuracy rates as a function of feature dimension. Each curve represents one classification method respectively. Similar to Section 4.4.4, features at each dimension are sequentially selected, and the performance is based on the average.

As shown in the figure, all methods have better performance with feature dimension scaling-up. We can see that the performance of NN and NS are close, which follow the similar trend, and the SR-based classifier is different from them. More specifically, when the feature dimension is less than 40, NN and NS are better than SR; when the feature dimension is more than 40, the SR-based classifier outperforms the other two methods. This observation indicates that using only 40 features is not sufficient

to recover the human activity signal via ℓ_1 minimization. However, when the feature dimension is equal or more than 45, the SR-based method can achieves a steady performance and beats the other two classical classification methods, achieving a maximum recognition rate of 87.72%.

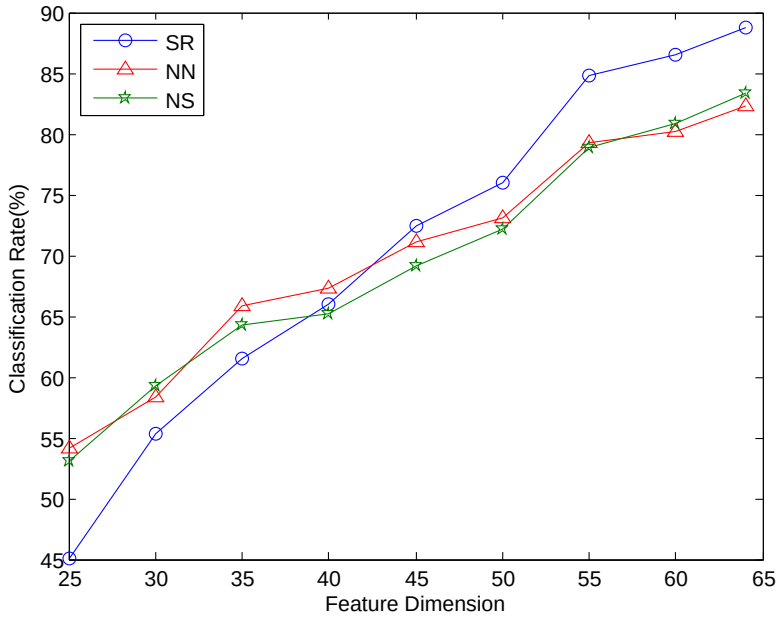

Figure 4.9: Classification Performance Comparison Between SR, NN and NS

4.5 Conclusion

Inspired by the sparsity of human activity signals, we adopted and described a sparse signal representation technique to co-recognize human activity and sensor location in wearable sensor networks. The experimental results showed that our method can achieve greater than 87% recognition accuracy with 14 different activities and 7 on-body locations. We also showed that using the ℓ_1 norm is better than the ℓ_2 norm in terms of both accuracy and stability. Moreover, we compared a SR-based framework to two classical methods, NN-based method and NS-based method, respectively. The results showed that SR outperforms both of them when feature dimension is more than a threshold. Considering the promising results in the pilot study, we intend to run ad-

ditional experiments with a larger-scale group and evaluate more activities and sensor location in future work.

CHAPTER 5

Remote Rehabilitation

5.1 Introduction

In traditional medicine, physical rehabilitation programs are performed in hospitals or outpatient treatment centers, where therapists trained in rehabilitation provide guidance as well as monitor patient recovery. Rehabilitation exercise programs help patients return to regular health after surgical procedures or illness.

Physical rehabilitation is well recognized to provide accelerated and long lasting benefits to patients [BH07, FCE01]. Johns Hopkins Hospital implemented physical rehabilitation programs in early post-surgical stages, and found up to 22% reduction in ICU stays and clear reductions in net financial costs [LMK13]. The aim of such rehabilitation regimens is to improve muscular strength and specific body range of motion. Patients undergoing physical rehabilitation follow the exercises assigned by physical therapists on a regular or semi-regular basis. There is a need for physical therapists to manually monitor and evaluate the rehabilitation process in order to check the patients' recovery progresses according to plan. With manual monitoring, there is not only a large cost in tracking rehabilitation progress, but also the measurement of progress is difficult to quantize. Automated monitoring of rehabilitation exercises is proposed here as a solution.

5.1.1 Related Work

In this section, we describe the current literature in the field of automated physical rehabilitation monitoring then with a focus on on-bed exercises. Zhou and Hu's survey [ZH08] of human motion tracking systems for rehabilitation targeted primarily stroke sufferers, but this list of technological approaches can be applied to rehabilitation in general. Specialized exercise equipment, such as treadmills, or even robotic guidance devices [KVA00] have been investigated for strength building applications. In addition, visual tracking of body posture has undergone much research, however many relied on marker systems placed on the body [TH03]. Furthermore, marker-free systems try to overcome these limitations by building 2-D [FB02] or 3-D models of the human body [DF01]. Other non-visual methods have been research, such as using inertial sensors [JMO05]. Combination of sensors are also described, such as Huang's et al. work with inertial sensors and visual camera that tracked both (fine-grain) finger and (course-grain) hand movements for upper extremities rehabilitation [HXS12].

More specific to patients who are bed-ridden or restricted to motions on bed, are current research approaches that focus on posture change detection. Posture change analysis by Nakajima et al. used real-time video image sequences to extract optical flow information [NMT01]. Jones et al. used a 24 pressure sensor array to identify posture movement times and then evaluated sleep restlessness [JGK06], while Adami et al. used 4 load cell sensors with 200Hz sampling rates to analyze time varying waveforms as patients move on bed [APH10].

Accurate detection of posture movement are shown in these previous methods. They are able to show the existence of posture changes, but they do not target the recognition of actual posture. A system to detect transitions between sitting and lying postures using large pressure sensor arrays placed under the mattress was developed by Foubert et al. [FMG12]. Yousefi et al. were successful in recognizing sleep posture using principle component analysis (PCA) [YOF11], while Hsia et al. used statisti-

Figure 5.1: Bedsheet Prototype

cal feature extraction [HHC08]. Harada et al. investigated body posture tracking and used generative models of human body pressure to match the patient's pressure distribution [HSM00]. Similarly, our previous work in this field investigated static posture recognition [LXH13], however, this current project will focus toward the transitional and dynamic nature of body motion as seen in pressure image sequences.

The remainder of the chapter is organized as follows. Section 5.2 describes the overall design to recognize on bed rehabilitation exercises as well as a description of the pressure sensitive bedsheet. Section 5.3 details the algorithmic process using a dimension reduction methods on body pressure image sequences and subsequent exercise recognition. Experimental set up and results are given in Section 5.4. Finally, future work and conclusion are discussed in Section 5.5.

5.2 System Overview

Our system design consists of a high density sensor bedsheet and a connected tablet which collects the pressure image sequences. The tablet analyses the data and transmits the results through wireless communication to a monitoring station. A subject lies on

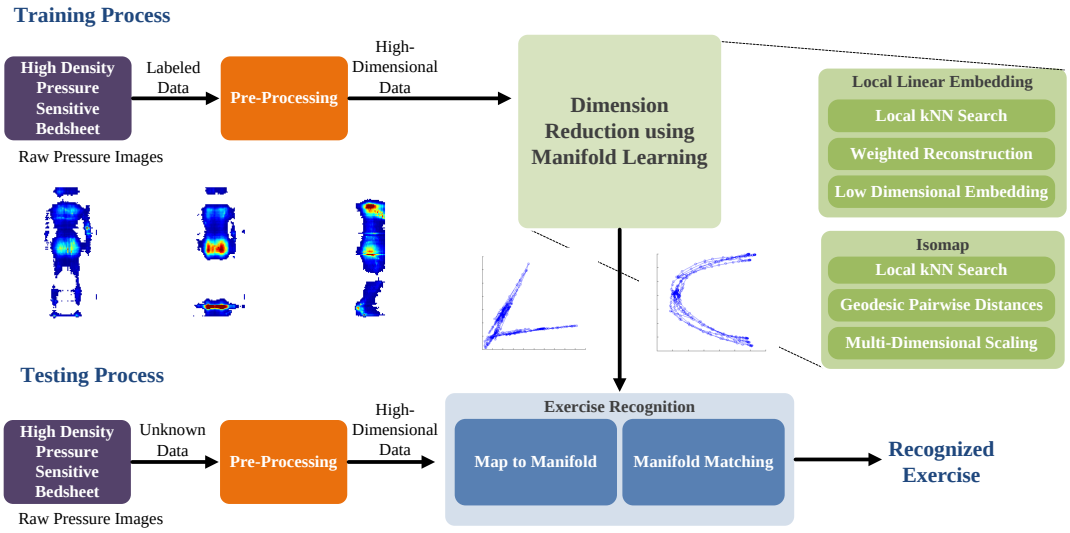

Figure 5.2: Process Flow for On-bed Exercise Monitoring

the bedsheet and follows the instruction given by physical therapists. The tablet along with the bed sheet can pre-store the treatment scripts in its persistent storage and play the scripted text visually and vocally.

5.2.1 Bedsheet design

Figure 5.1 shows the prototype of the bedsheet system. The system consists of three components: a 64×128 pressure sensor array, an embedded data sampling unit, and a tablet for data analysis and storage. The sensor array is based on eTextile material which is fiber-based yarn coated with piezoelectric polymer [XLH11,XHA12]. Without pressure, the resistance of the eTextile material is high. As external force is applied to the surfaces of the material, the eTextile fibers are squeezed together and, due to its pressure sensitive characteristics, the electrical resistance decreases in that region.

The bedsheet itself has a three-layer structure. The top layer is regular fabric that is coated with 64 parallel conductive lines. The middle layer is the eTextile material and the bottom layer has 128 conductive lines arranged perpendicular to the top 64 lines. At

each intersection of conductive lines, the structure forms a pressure sensitive resistor. There are effectively 8192 pressure sensors in total.

5.2.2 Algorithm Overview

Figure 5.2 introduces the three main steps, and this process is described in more detail in the following section.

- *Step 1: Pre-processing of the pressure image*
- *Step 2: Dimension reduction via manifold learning*
- *Step 3: Activity recognition using manifold matching.*

Exercise recognition uses a subject's pre-recorded training data to match exercises under test. The training data consists of samples of on-bed exercises that are analyzed to produce a low dimensional representation, i.e. a manifold, from the original high resolution pressure images. When new exercise data is recorded, it is mapped to the same low dimensional manifold representation and matched to the closest training exercise manifold.

5.3 Algorithmic Framework for Exercise Monitoring

This section details the algorithmic framework of the on-bed patient exercise recognition.

• *Step 1: Pre-processing*

The pre-processing of the raw pressure images is required so that the image sequences can be standardized in such a way to enable successful recognition. The raw images contain noise and artifacts that affect recognition, and pre-processing mitigates

the side effects as much as possible.

Firstly, the subject can be located anywhere on the bedsheet, so to correct this, the images are aligned to a common center of mass and relocated to the center of the image. A smoothing filter of a symmetric 5×5 unit normal distribution is applied. This smoothing minimizes the effect of noise in the pressure map. The images are normalized so that the sum of pixel weights is one. This step attempts to counteract the affects for the differing body mass.

• *Step 2: Dimension Reduction using Manifold Learning*

In this work, we compare two methods of manifold learning: Local Linear Embedding (LLE) and Isomap.

5.3.1 Local Linear Embedding

The first method to map the image sequence X to a low dimensional space is based on the Local Linear Embedding (LLE) framework by Saul and Roweis [SR03], which has various applications in machine learning systems [LXH12]. LLE is an unsupervised algorithm that reconstructs the global data non-linearly while preserving local linearity. After the computation, similar images will be clustered within the low dimensional manifold. In general, there are three steps in the algorithm, which will be described in the following.

5.3.1.1 k-Nearest Neighbor Searching

The first step is to search k-nearest neighbors for each image. In the searching process, we use Euclidean distance to evaluate the similarity between images. Normally the topology of embedding will be well-preserved over a range of neighborhood sizes. For this work, we searched for the 30 nearest neighbors of each image. Alternatively, a

threshold distance can also be used to select the local nearest neighbors.

5.3.1.2 Weighted Reconstruction With Nearest Neighbors

The second step is to reconstruct a sample image using its nearest neighbors. Assume that an arbitrary image x has k-nearest neighbors x_i. Then x can ideally be represented as a linear combination of its neighbors. In general, an exact reconstruction will not be found, so a reconstruction error e can be formulated as:

$$e = \|x - \sum_{i=1}^{k} w_i x_i\|, \tag{5.1}$$

where w_i denotes the reconstruction weight for the neighbor x_i. The optimization process minimizes the reconstruction error of all images by setting the weight w_i values. There are two attributes of the problem to ensure it is well-imposed: (1) exclusiveness: the weight w_i of x is zero if x_i is not in the nearest neighbor list of x; (2) normalization: the sum of the weights of nearest neighbors should be 1. Therefore, we can rewrite the problem for all images:

$$E = \sum_{j=1}^{N} \|x_j - \sum_{i=i}^{N} w_{ij} x_{ij}\|. \tag{5.2}$$

We can see that Equation (5.2) represents the reconstruction problem and has a closed least square solution, where the weights w_{ij} can be solved efficiently [SR03].

5.3.1.3 Low Dimensional Embedding Construction

The third step is to construct the corresponding embedding in a low dimensional space. Based on the calculation results from the second step, the intrinsic geometrical structure of each local cluster is characterized by w_{ij}. We assume that the neighborhood relation in high dimensional space should be preserved in low dimensional space, i.e. within a manifold. Based on this assumption, the embedding process is to search for the low

dimensional representation y of x by minimizing the following error E':

$$E' = \sum_{j=1}^{N} \|y_j - \sum_{i=i}^{N} w_{ij} y_{ij}\|, \tag{5.3}$$

where y_j are the corresponding points in the low dimensional manifold. We note that Equation (5.3) is in a quadratic form and the embedding optimization process is efficiently solvable. Furthermore, all the manifold points y_i will be computed globally and simultaneously, and no local optima will affect the construction result.

Equation (5.2) indicates that the low dimensional construction is only based on the locality of the high dimension data. This means that the computed manifold y_i can be translated with an arbitrary displacement without affecting Equation (5.3). Moreover, LLE states the computed manifold y_i can be rotated by an arbitrary angle without affecting Equation (5.3) too. This geometric attribute can be represented and formulated in the following two equations:

$$\sum_{i=1}^{N} y_i = 0, \tag{5.4}$$

$$\frac{1}{N} \sum_{i=1}^{N} y_i \cdot y_i = 1. \tag{5.5}$$

Therefore, manifold construction problem becomes an eigenvalue problem [SR03], in which we select the matrix rank to have the desired manifold dimension.

5.3.2 Isomap

The second method to map the image sequence X to a low dimensional space is based on the Isomap framework by Tenenbaum et al. [TSL00]. Isomap also performs nonlinear dimension reduction and extends the classical linear Multi-dimensional Scaling (MDS) [KW78]. The task of MDS is to find a set of co-ordinates that satisfies the given pairwise distances between the points. However, given that the points may lie on a

manifold inside a high dimensional space, linear pairwise distances may not represent the true structure.

5.3.2.1 k-Nearest Neighbor Searching

This stage is similar to LLE where k-Nearest Neighbors for each original image are selected using the Euclidean distance in high dimensions.

5.3.2.2 Computation of Geodesic Pairwise Distance

The distances between all pairs of images are estimated given the distances between local sets of images. This results in the geodesic pairwise distances, i.e. the shortest path distances D_{ij}^X along a curved surface. Floyd's algorithm can be used to find the shortest paths between every pair of images in a graph, or other faster methods [KGG94].

5.3.2.3 Low Dimensional Embedding via Multi-Dimensional Scaling

The final stage of Isomap applies the regular MDS algorithm to the geodesic distances. MDS finds points Y that minimize the total error between pairwise distances in high dimensional space and pairwise distances in low dimensional space:

$$\min_Y \sum_{i=1}^{N} \sum_{j=1}^{N} (D_{ij}^X - D_{ij}^Y)^2, \tag{5.6}$$

where D_{ij}^Y is the pairwise distance between points in the low d-dimensional space Y. The low dimensional embedding is solved by taking the co-ordinates of the top d eigenvectors of the inner-product matrix of the geodesic pairwise distances [KW78].

Contrasting with LLE, Isomap preserves pairwise distances within the manifold, while LLE preserves the local linear structure within the manifold.

• *Step 3: Exercise Recognition using Manifold Matching*

5.3.2.1 Map input to manifold

Once the training data has been reduced in dimensionality to its corresponding low dimensional form, we can evaluate the process using new test data against the training data. The testing data needs to be converted into manifold form. Note that it is possible to run the whole LLE or Isomap algorithm again on the combined testing data and training data in order to find the low dimensional representation of the test data, however this is not necessary.

Instead, a portion of the algorithm need only be executed [SR03, ZS11a]. Given a new test image $\hat{x}$, we wish to find its low dimensional representation, $\hat{y}$. To do so, the weights w_i are computed from the k nearest neighbors of $\hat{x}$ in the training set, x_i. This is again the least squares solution to minimize

$$\|\hat{x} - \sum_{i=1}^{k} w_i x_i\|, \tag{5.7}$$

with the constraint $\sum_{i=1}^{k} w_i = 1$. Since the corresponding low dimensional co-ordinates of x_i are known during the training phase, we can construct the resultant embedded co-ordinates for $\hat{y}$ using the same weights:

$$\hat{y} = \sum_{i=1}^{k} w_i y_i, \tag{5.8}$$

where y_i are the corresponding embedded points of x_i.

5.3.2.2 Manifold Matching

Exercise tracking involves checking how well the test testing data follows the trajectory of a given exercise manifold. We can compare trajectories using a similar idea to the Hausdorff distance. The distance of a point to a manifold is equal to the shortest Euclidean distance to any point in the manifold. The similarity of two manifolds is the mean of the point distances of all the points of one manifold, M_1 to the other manifold,

Table 5.1: Confusion Matrix LLE

	Leg Lift	Head Lift	Heel Slide	Lateral Roll	Sit Up	Total	Recall
Leg Lift	42	4	6	0	0	52	80.8%
Head Lift	9	42	2	0	0	53	79.2%
Heel Slide	7	0	54	0	0	61	88.5%
Lateral Roll	0	0	0	50	0	50	100%
Sit Up	0	0	0	1	56	57	98.2%
Total	58	46	62	51	56	273	
Precision	72.4%	91.3%	87.1%	98.0%	100%		

Table 5.2: Confusion Matrix Isomap

	Leg Lift	Head Lift	Heel Slide	Lateral Roll	Sit Up	Total	Recall
Leg Lift	45	3	4	0	0	52	86.5%
Head Lift	7	44	2	0	0	53	83.0%
Heel Slide	6	1	54	0	0	61	88.5%
Lateral Roll	0	0	0	49	1	50	98.0%
Sit Up	0	0	0	3	54	57	94.7%
Total	58	48	60	52	55	273	
Precision	77.6%	91.7%	90.0%	94.2%	98.2%		

M_2. This is expressed as

$$s(M_1, M_2) = \frac{1}{T_{M_1}} \sum_{i=1}^{T_{M_1}} \min_{1 \le j \le T_{M_2}} \|M_1(i) - M_2(j)\|, \tag{5.9}$$

where T_{M_1} and T_{M_2} are the number of points in each manifold. This metric allows manifolds of different lengths to be compared since different subjects take different times to perform each activity. Since the Hausdorff metric is not symmetric, we can take the following sum as the manifold matching metric,

$$d(M_1, M_2) = s(M_1, M_2) + s(M_2, M_1). \tag{5.10}$$

So, to measure how well a subject adheres to the prescribed exercise, the testing data is mapped to corresponding low dimensional embedding points that defines a manifold, then the manifold is measured against the expected exercise manifold.

Figure 5.3: Example of Leg Lift Exercise

5.4 Experimental Results

5.4.1 Experimental Setup

We evaluated this framework for exercise monitoring on 10 subjects, 7 male subjects and 3 female subjects. The weight of the subjects ranged from 50kg to 85kg, and height between 155cm and 188cm. There were 5 selected on-bed exercises: alternating Leg Lifts, Head Lifts, alternating Heel Slides, alternating Lateral Rolls (lying on back to lying on side), and Sit-Ups. These exercises have been selected as being appropriate for on-bed monitoring [NW06]. In the training data collection, at least 5 sets of image sequences were recorded for each of the 5 on-bed exercises for each subject, so there were more than 250 exercise sequences under test. Each image sequence comprises one *exercise activity*, e.g. one Leg Lift exercise activity includes lifting of the right leg

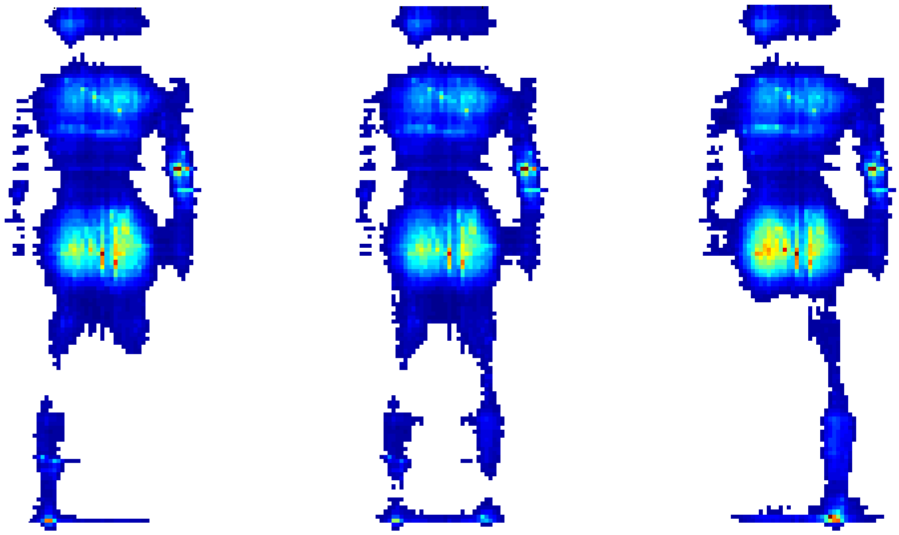

Figure 5.4: Left and Right Leg Lift

followed by the left leg. The order of left and right does not matter in this system. Each image sequence of exercise activity contained at least 40 individual images. Variations in body, arm and leg positions were allowed.

The training data for each subject was combined and manifold learning was applied to generate the training manifolds for the exercises. Testing was carried out by exercise activity and repeated for each of the exercise activities.

5.4.2 Experimental Evaluation

Tables 5.1 and 5.2 show recognition results for the 5 exercises in 10 subject dependent testing. Notably, the highest recognition rates are Lateral Rolls and Sit Ups. This can be expected since these exercises involve the greatest physical exertion and hence the greatest pressure image differences. The other three exercises exhibit a comparably lower rate of recognition due to more of a fine grain difference in the pressure image sequences. The confusion matrix shows that there are the most misclassifications

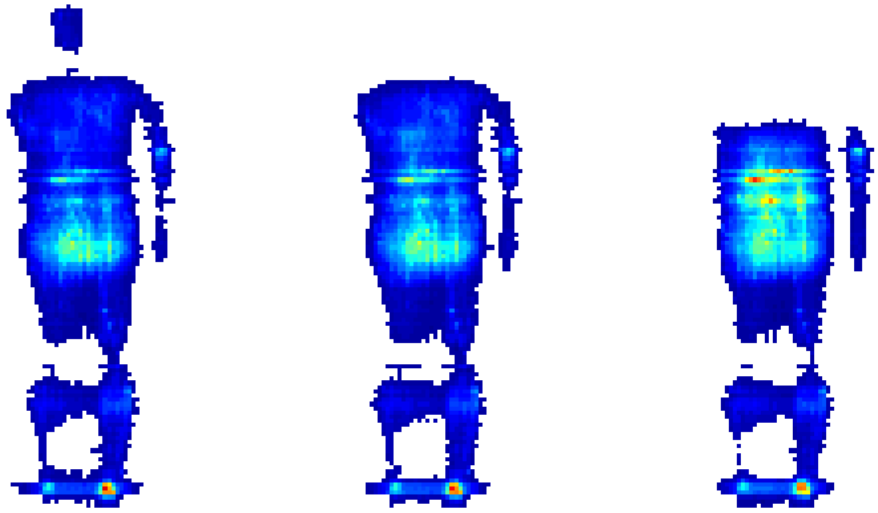

Figure 5.5: Head Lift

between Left Lifts and Heel Slides. By observing Figures 5.4 and 5.7, there are clear similarities in the pressure images and the leg positions only constitute minor variations in the overall pressure maps.

Figure 5.10 shows samples of the low dimensional visualization of manifolds for some of the exercises. Generally the shapes of the manifolds give an indication of the differences between the exercises. It is interesting to note in Figure 5.10(d) that the variations in Sit Ups can be seen. Using the Manifold Matching method, a quantified measurement of exercise recognition is performed.

5.4.3 Comparing LLE and Isomap

The accuracy results between LLE and Isomap are somewhat similar as shown in Tables 5.1 and 5.2. LLE has higher accuracy for the Lateral Rolls and Sit Ups, while Isomap shows higher accuracy for Left Lifts, Head Lifts and Heel Slides.

Figure 5.11 shows samples of how head-lifts appear on a leg-lift manifold under

Figure 5.6: Example of Heel Slide Exercise

LLE, and sit-up compared to lateral rolls. Figure 5.12 shows the same results for I-somap. It is evident that the sample exercises can be discerned from each other. It is interesting to note that the manifold shapes produced by Isomap tend to be more variable, which may contribute to the slight variation in accuracy levels.

The dimension reduction algorithm requires the data to be non-sparse, i.e. there must be sufficient sampling of pressure images to track motions. The current state of technology for pressure images of this resolution are 2-5 samples per second. Higher sampling rates can be achieved with the loss of image resolution.

Figure 5.13 suggests that the intrinsic dimension of the rehabilitation exercise data is 2 and is seen at the knee point of the dimensionality graph.

5.4.4 Sequential Evaluation

As a further evaluation of this framework for exercise recognition, we investigated a longitudinal study of continuous monitoring through a number of set exercise activity programs. More specifically, each of the 5 exercises were performed sequentially to analyze whether the algorithm can separate and recognize the exercises. Figure 5.14

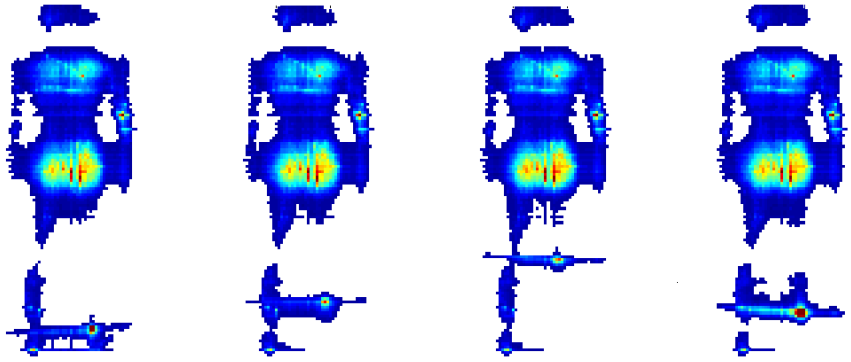

Figure 5.7: Right Heel Slide

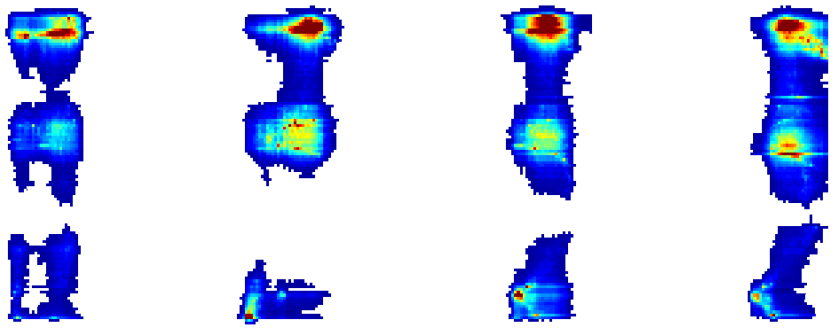

Figure 5.8: Lateral Rolls

shows the evaluation results of this experiment, where red dash line represents the ground truth, and blue line represents the classification results. We can see that 3 sets of 5 different exercises are performed sequentially in this evaluation, and finally 13 out of the 15 exercises are recognized correctly.

5.5 Conclusion

In this work, an on-bed exercise monitoring system design, that allows care-givers to track compliance to physical rehabilitation programs, is presented. We employ the

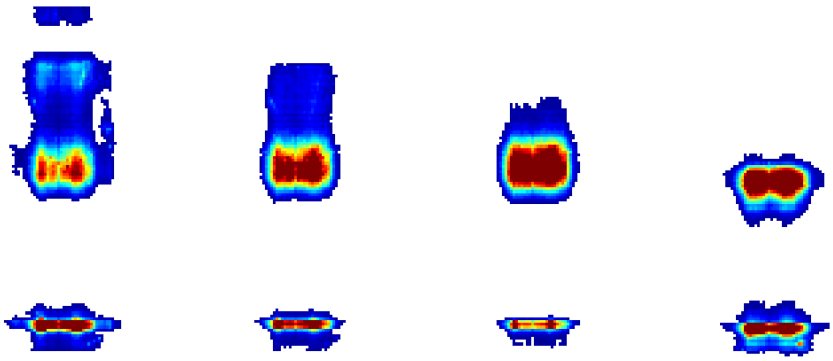

Figure 5.9: Sit Up

novel use of dimension reduction techniques from pressure images to find intrinsic subspace representations of the data. We also evaluated a metric to match manifolds to enable quantified measurement of adherence to prescribed exercises.

Future work involves quantifying the performance of a given exercise with respect to standard exercise models, i.e. how closely is the patient following the exercise patterns such as angle of Leg Lifts and length of Heel Slide. Other future endeavors includes facilitating a system to work on chairs for sitting rehabilitative exercise, not only in clinical rooms or home-base care but also for cars or wheelchairs. 3D model reconstruction of patients from 2D pressure image is another goal that can be accomplished using the results of this research work.

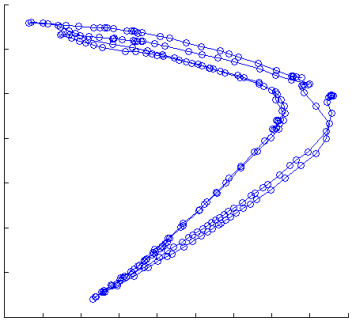

(a) Leg Lift

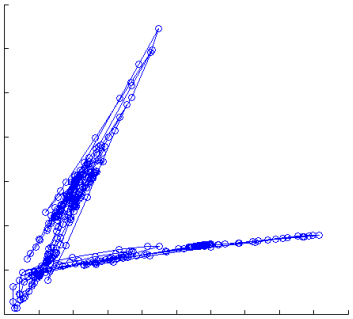

(b) Heel Slide

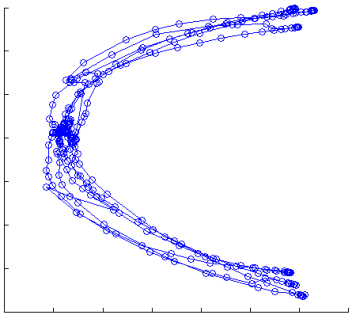

(c) Lateral Roll

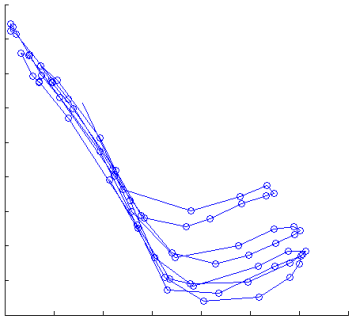

(d) Sit Up

Figure 5.10: Samples of Exercise Manifolds LLE

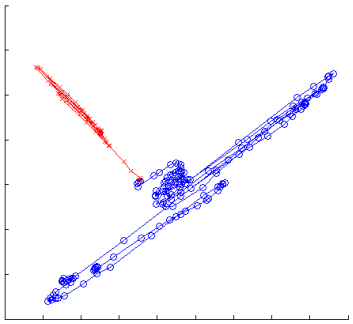

(a) Leg Lift (blue) vs Head Lift (red)

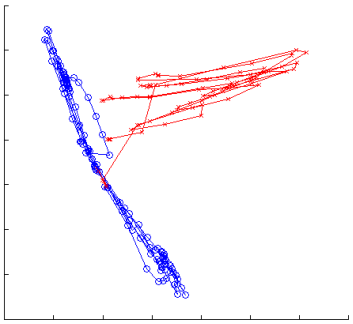

(b) Roll (blue) vs Sit up (red)

Figure 5.11: Samples of Exercise Manifolds LLE

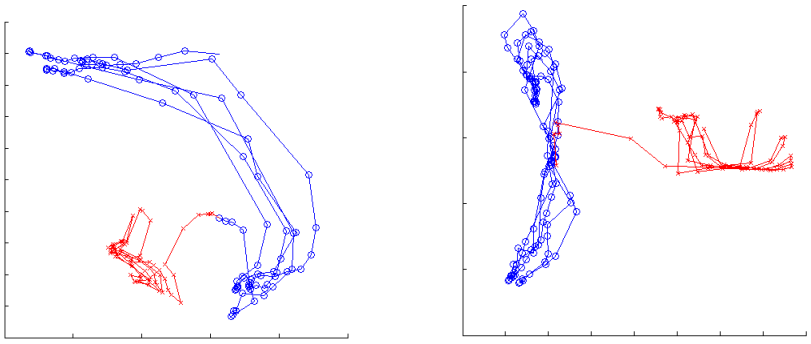

(a) Leg Lift (blue) vs Head Lift (red) (b) Roll (blue) vs Sit up (red)

Figure 5.12: Samples of Exercise Manifolds Isomap

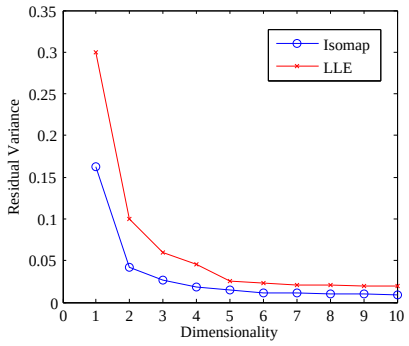

Figure 5.13: Intrinsic Dimensionality of the manifolds are found at the knee points of the graph.

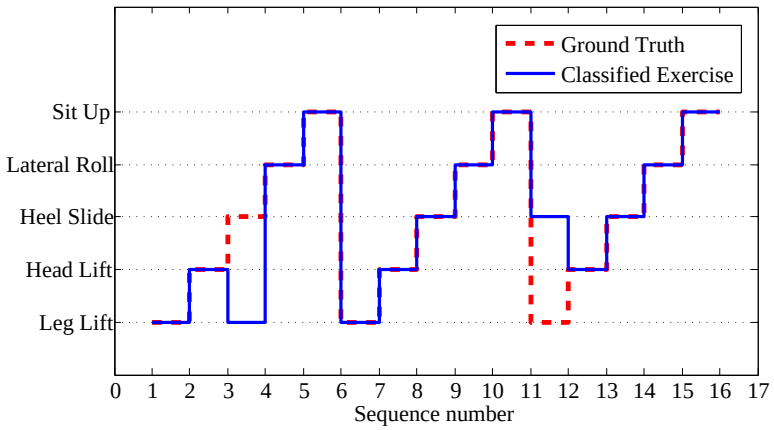

Figure 5.14: A set of 15 exercise activities performed sequentially against ground truth

CHAPTER 6

Summary

In summary, this thesis introduces embedded sensing and computing technologies in four high-impacted healthcare fields, including pressure ulcer reduction, cardiopulmonary monitoring, fall prevention and rehabilitation. More specifically, Chapter 2 discussed the technologies based e-Textile materials for non-invasive pressure measurement and pressure ulcer reduction [LXH13]. Chapter 3 introduced a non-contact vital sign detection and measurement system based on the Doppler radar. Its related self-calibration algorithm is also addressed [Xa13]. Chapter 4 presented a framework of inertial sensor based human activity analysis. This framework is based on statistical feature extraction and sparse representation [XZS12c]. Chapter 5 demonstrated a remote rehabilitation system based on the Smart Bedsheet platform [LHX13].

REFERENCES

[ALK] Cristina Ambrogio, Xazmin Lowman, Ming Kuo, Joshua Malo, Anil Prasad, and Sairam Parthasarathy. "Sleep and non-invasive ventilation in patients with chronic respiratory insufficiency." *Intensive Care Medicine*, **35**:306–313.

[APH10] Adriana M. Adami, Misha Pavel, Tamara L. Hayes, and Clifford M. Singer. "Detection of movement in bed using unobtrusive load cell sensors." *Transactions on Infomation Technology in Biomedicine*, **14**(2):481–490, March 2010.

[ASV11] Navid Amini, Majid Sarrafzadeh, Alireza Vahdatpour, and Wenyao Xu. "Accelerometer-Based On-Body Sensor Localization for Health and Medical Monitoring Applications." *Pervasive and Mobile Computing*, **7**(41):746–760, August 2011.

[ATM01] H. Aoki, Y. Takemura, K. Mimura, and M. Nakajima. "Development of non-restrictive ensing system for sleeping person using fibre grating vision sensor." In *International Symposium on Micromechatronics and Human Science*, pp. 155–160. Nagoya, Japan, October 2001.

[BH07] Andrea L. Behrman and Susan J. Harkema. "Physical Rehabilitation as an Agent for Recovery After Spinal Cord Injury." *Physical Medicine and Rehab Clinics of North America*, **18**(2):183–202, 2007.

[BHK97] P. Belhumeur, J. Hespanha, and D. Kriegman. "Eigenfaces vs. Fisherfaces: recognition using class specific linear projection ." *IEEE Transactions on Pattern Analysis and Machine Intelligence (PAMI)*, **19**(7):711–720, July 1997.

[Bis06] Christopher Bishop. *Pattern Recognition and Machine Learning*. Springer, New York, 2006.

[Bjo67] Ake Bjorck. "Solving Linear Least Squares Problems by Gram-Schmidt Orthogonalization." *BIT Numerical Mathematics*, **7**(1):1–21, January 1967.

[BKV97] C. Bouten, K. Koekkoek, M. Verduim, R. Kodde, and J. Janssen. "A Triaxial Accelerometer and Portable Data Processing Unit for the Assessment of Daily Physical Activity." *IEEE Transactions on Biomedical Engineering*, **44**(1):136–147, March 1997.

[Bla96] A. Blaugrund. "Notes on Doppler-Shift Lifetime Measurements." *Nuclear Physics*, **88**(3):501–512, November 1996.

[BLP09] O. Boric-Lukecke, V. Lubecke, B. Park, W. Massagram, and B. Jokanovic. "Heartbeat interval extraction using doppler radar for health monitoring." In *International Conference on Telecommunication in Modern Satellite, Cable, and Broadcasting Services*, pp. 139–142. Nis, Berbia, October 2009.

[BMN10] Harold Brem, Jason Maggi, David Nierman, Linda Rolnitzky, David Bell, Robert Rennert, Michael Golinko, Alan Yan, Courtney Lyder, and Bruce Vladeck. "High cost of stage IV pressure ulcers." *American Journal of Surgery*, **200**:473–477, Oct 2010.

[BRM89] Daniel J. Buysse, Charles F. Reynolds, Timothy H. Monk, Susan R. Berman, and David J. Kupfer. "The Pittsburgh sleep quality index: A new instrument for psychiatric practice and research." *Psychiatry Research*, **28**(2):193–213, 1989.

[BV04] S Boyd and L. Vandenberghe. *Convex Optimization*. Cambridge, New York, 2004.

[Car] Cardiac Direct. `http://www.cardiacdirect.com/`.

[CCB11] Shanshan Chen, Christopher Cunningham, Bradford Bennett, and John Lach. "Enabling Longitudinal Assessment of Ankle Foot Orthosis for Childeren with Cerebral Palsy." In *ACM International conference on Wireless Health*, pp. 1–10, San Deigo, CA, USA, October 2011.

[CCH07] M. Cretikos, J. Chen, K. Hillman, R. Bellomo, S. Finfer, and A. Flabouris. "The objective medical emergency team activation criteria: a case-control study." *Resuscitation*, **73**(1):62–72, January 2007.

[CH67] T. Cover and P. Hart. "Nearest Neighbor Pattern Classification." *IEEE Transactions on Information Theory*, **13**(1):21–27, January 1967.

[CLL08] Mingqi Chen, O. Lubecke, and V. Lubecke. "0.5-um CMOS Implementation of Analog Heart-Rate Extraction With a Robust Peak Detector." *IEEE Transactions on Instrumentation and Measurement*, **57**(4):690–698, April 2008.

[CNK10] Yu Chi, Patrick Ng, Eric Kang, Joseph Kang, Jennifer Fang, and Gert Cauwenberghs. "Wireless non-contact cardiac and neural monitoring." In *ACM Conference on Wireless Health*, pp. 15–23. San Diego, October 2010.

[CRF05] Y. Chekmenev, H. Rara, and A. Farag. "Non-contact, wavelet-based measurement of vital signs using thermal imaging." In *ICGST International Conference on Graph, Vision and Image Processing*, pp. 25–30. Cairo, Egypt, December 2005.

[CRT06a] E. Candes, J. Romberg, and T. Tao. "Robust Uncertainty Principles: Exact Signal Reconstruction from Highly Incomplete Frequency Information." *IEEE Transactions on Information Theory*, **52**(1):489–509, December 2006.

[CRT06b] E.J. Candes, J. Romberg, and T. Tao. "Robust uncertainty principles: exact signal reconstruction from highly incomplete frequency information." *Information Theory, IEEE Transactions*, **52**(2):489–509, Feb. 2006.

[CRT06c] Emmanuel Candes, Justin Romberg, and Terence Tao. "Stable Signal Recovery from Incomplete and Inaccurate Measurements." *Communications in Pure Applied Math*, **59**(4):1207–1223, April 2006.

[CT91] Thomas M. Cover and Joy A. Thomas. *Elements of information theory*. Wiley-Interscience, New York, NY, USA, 1991.

[CVX12] CVX Research Inc. "CVX: Matlab Software for Disciplined Convex Programming, version 2.0." `http://cvxr.com/cvx`, August 2012.

[DBG05] Ariel Diaz, Martial Bourassa, Marie Guertin, and Jean Tardif. "Long-term prognostic value of resting heart rate in patients with suspected or proven coronary artery disease." *European Heart Journal*, **26**(10):967–974, March 2005.

[DBL04] A. D. Droitcour, O. Boric-Lubecke, V. M. Lubecke, J. Lin, and G. T. A. Kovac. "Range correlation and I/Q performance benefits in single-chip silicon Doppler radars for noncontact cardiopulmonary monitoring." *IEEE Transactions on Microwave Theory and Techniques*, **52**(3):838–848, March 2004.

[DF01] Quentin Delamarre and Olivier Faugeras. "3D Articulated Models and Multiview Tracking with Physical Forces." *Computer Vision and Image Understanding*, **81**(3):328–357, 2001.

[DLL04] A. D. Droitcour, Olga Lubecke, Victor Lubecke, Jenshan Lin, and Gregory Kovacs. "Range correlation and I/Q performance benefits in single-chip silicon Doppler radars for noncontact cardiopulmonary monitoring." *IEEE Transactions on Microwave Theory and Techniques*, **52**(3):557–565, March 2004.

[Don04] D. Donoho. "Compressed Sensing." *IEEE Transactions on Information Theory*, **52**(4):1289–1306, April 2004.

[Don06] D. Donoho. "Compressed Sensing." *IEEE Transactions on Information Theory*, **52**(1):1289–1306, May 2006.

[FB02] Ronan Fablet and Michael J. Black. "Automatic Detection and Tracking of Human Motion with a View-Based Representation." In *Proceedings of the 7th European Conference on Computer Vision-Part I*, pp. 476–491, 2002.

[FCE01] M Fransen, J Crosbie, and J Edmonds. "Physical therapy is effective for patients with osteoarthritis of the knee: a randomized controlled clinical trial." *The Journal of Rheumatology*, **28**(1):156–164, 2001.

[FH09] R. Fletcher and J. Han. "Low-cost differential front-end for Doppler radar vital sign monitoring." In *International Microwave Symposium Digest*, pp. 7–12. Boston, USA, June 2009.

[FMG12] N. Foubert, A.M. McKee, R.A. Goubran, and F. Knoefel. "Lying and sitting posture recognition and transition detection using a pressure sensor array." In *Medical Measurements and Applications Proceedings (MeMeA), 2012 IEEE International Symposium*, pp. 1–6, 2012.

[For] ForaCare. `http://www.foracare.com/`.

[FPF99] Andrew Fitzgibbon, Maurizio Pilu, and Robert Fisher. "Direct Least Square Fitting of Ellipses." *IEEE Transactions on Pattern Recognition and Machine Intelligence*, **21**(5):476–480, May 1999.

[GIL] C. Gu, T. Inoue, and C. Li. "Analysis and Experiment on the Modulation Sensitivity of Doppler Radar Vibration Measurement." In *IEEE Microwave and Wireless Components Letters*, p. in print.

[GLF12] C. Gu, R. Li, R. Fung, C. Torres, S. Jiang, , and C. Li. "Accurate Respiration Measurement using DC-Coupled Continuous-Wave Radar Sensor for Motion-adaptive Cancer Radiotherapy." *IEEE Transactions on Biomedical Engineering*, **59**(11):3117–3123, November 2012.

[GLJ09] Hassan Ghasemzadeh, Vitali Loseu, and Roozbeh Jafari. "Wearable coach for sport training: A quantitative model to evaluate wrist-rotation in golf." *Journal of Ambient Intelligence and Smart Environments (JAISE)*, **1**(2):173–184, April 2009.

[GR70] G. Golub and C. Reinsch. "Singular Value Decomposition and Least Squares Solutions." *Numeriche Mathematic*, **14**(7):403–420, November 1970.

[GVH07] J. Gemmeke, T. Virtanen, and A. Hurmalainen. "Exemplar-Based Sparse Representations for Noise Robust Automatic Speech Recognition." *IEEE Transactions on Pattern Analysis and Machine Intelligence (PAMI)*, **19**(15):2067–2080, April 2007.

[GWC97] A. Groote, M. Wantier, G. Cheron, M. Estenne, and M. Paiva. "Chest Wall Motion During Tidal Breathing." *Journal of Applied Physiology*, **83**(1):1531–1537, June 1997.

[HB07] Ju Han and Bir Bhanu. "Fusion of Color and Infrared Video for Moving Human Detection." *Pattern Recognition*, **40**(6):1771–1784, May 2007.

[HC11] G. Hughes and M. Chraibi. "Calculating ellipse overlap areas." *ArXiv eprints 1106.37.87*, pp. 1–49, 2011.

[HDS10] Enamul Hoque, Robert F. Dickerson, and John A. Stankovic. "Monitoring body positions and movements during sleep using WISPs." In *Wireless Health 2010*, WH '10, pp. 44–53, 2010.

[HF98] Radim Halir and Jan Flusser. "Numerically Stable Direct Least Squares Fitting Of Ellipses.", 1998.

[HHC08] Chi-Chun Hsia, Yu-Wei Hung, Yu-Hsien Chiu, and Chia-Hao Kang. "Bayesian classification for bed posture detection based on kurtosis and skewness estimation." In *e-health Networking, Applications and Services, 2008. HealthCom 2008. 10th International Conference on*, pp. 165–168, July 2008.

[Hil] Hillrom. `http://www.hill-rom.com`.

[HLA09] C.C. Hsia, K.J. Liou, A.P.W. Aung, V. Foo, W. Huang, and J. Biswas. "Analysis and comparison of sleeping posture classification methods using pressure sensitive bed system." In *Engineering in Medicine and Biology Society, 2009. EMBC 2009. Annual International Conference of the IEEE*, pp. 6131–6134, Sept. 2009.

[HSM00] T. Harada, T. Sato, and T. Mori. "Human motion tracking system based on skeleton and surface integration model using pressure sensors distribution bed." In *Proc. Workshop on Human Motion*, p. 99, 2000.

[HXS12] Ming-Chun Huang, Wenyao Xu, Yi Su, Belinda Lange, Chien-Yen Chang, and Majid Sarrafzadeh. "SmartGlove for upper extremities rehabilitative gaming assessment." In *Proceedings of the 5th International Conference on Pervasive Technologies Related to Assistive Environments*, pp. 20:1–20:4, 2012.

[Idz03] C. Idzikowski. *Beating Insomnia: How to Get a Good Night's Sleep*. Gill & MacMillan, 2003.

[JGK06] M.H. Jones, R. Goubran, and F. Knoefel. "Identifying Movement Onset Times for a Bed-Based Pressure Sensor Array." In *Medical Measurement and Applications. MeMea IEEE International Workshop*, pp. 111–114, April 2006.

[JKP94] George H. John, Ron Kohavi, and Karl Pfleger. "Irrelevant Features and the Subset Selection Problem." In *Machine Learning: Procs. 11th International Conference*, pp. 121–129. Morgan Kaufmann, 1994.

[JMO05] E. Jovanov, A. Milenkovic, C. Otto, P. de Groen, B. Johnson, S. Warren, and G. Taibi. "A WBAN System for Ambulatory Monitoring of Physical Activity and Health Status: Applications and Challenges." In *27th Annual International Conference of the Engineering in Medicine and Biology Society*, pp. 3810–3813, Jan. 2005.

[Jol] I.T. Jolliffe. *Principal Component Analysis*. Springer Series in Statistics.

[KAO06] Y. Kishimoto, A. Akahori, and K. Oguri. "Estimation of sleeping posture for M-Health by a wearable tri-axis accelerometer." In *Medical Devices and Biosensors. 3rd IEEE/EMBS International Summer School*, pp. 45–48, Sept. 2006.

[KGG94] Vipin Kumar, Ananth Grama, Anshul Gupta, and George Karypis. *Introduction to parallel computing: design and analysis of algorithms*. Benjamin-Cummings Publishing Co., Inc., Redwood City, CA, USA, 1994.

[KL09] Youngwook Kim and Hao Ling. "Human Activity Classification Based on Micro-Doppler Signatures Using a Support Vector Machine." *IEEE Transactions on Geoscience and Remote Sensing*, **47**(2):1328–1337, December 2009.

[KVA00] H. I. Krebs, B. T. Volpe, M. L. Aisen, and N. Hogan. "Increasing productivity and quality of care : Robot-aided neuro-rehabilitation." *Rehabilitation Research & Development*, **37**:639, Nov 2000.

[KW78] J.B. Kruskal and M. Wish. *Multidimensional Scaling*. Sage University Paper series on Quantitative Applications in the Social Sciences, 07-011, Beverly Hills and London: Sage Publications, 1978.

[LBG00] Kiang Liu, Erin Brien, Jack Guralnik, Michael Criqui, Gary Martin, Philip Greenland, and Mary McDermott. "Measuring Physical Activity in Peripheral Arterial Disease: A Comparison of Two Physical Activity Questionnaires with an Accelerometer." *Angiology*, **51**(12):91–100, December 2000.

[LGL] Yiguang Liu, Shuzhi Sam Ge, Chunguang Li, and Zhisheng You. "k-NS: A Classifier by the Distance to the Nearest Subspace." *Trans. Neural Networks*.

[LHX13] Jason Liu, Mingchun Huang, Wenyao Xu, Nabil Alshurafa, and Majid Sarrafzadeh. "On-Bed Monitoring for Range of Motion Exercises with

a Pressure Sensitive Bedsheet." In *IEEE International Conference on Implantable and Wearable Body Sensor Networks*, BSN'13, 2013.

[Lin92] J.C. Lin. "Microwave sensing of physiological movement and volume changes: a review." *Bioelectromagnetics*, **13**(3):557–565, November 1992.

[LL08] Changzhi Li and Jenshan Lin. "Random Body Movement Cancellation in Doppler Radar Vital Sign Detection." *IEEE Transactions on Microwave Theory and Techniques*, **56**(12):3143–3152, December 2008.

[LMK13] RK Lord, CR Mayhew, R Korupolu, EC Mantheiy, MA Friedman, JB Palmer, and DM Needham. "ICU Early Physical Rehabilitation Programs: Financial Modeling of Cost Savings." *Critical Care Medicine*, Jan. 2013.

[Low04] David G. Lowe. "Distinctive Image Features from Scale-Invariant Keypoints." *Int. J. Comput. Vision*, **60**(2):91–110, November 2004.

[LPH09] J. B. Lee, Y. H. Park, J. H. Hong, S. H. Lee, K. H. Jung, J. H. Kim, H. Yi, and C. Shin. "Determining optimal sleep position in patients with positional sleep-disordered breathing using response surface analysis." *Journal of Sleep Research*, **18**(1):26–35, 2009.

[LXH12] Zhinan Li, Wenyao Xu, Anpeng Huang, and M. Sarrafzadeh. "Dimensionality Reduction for Anomaly Detection in Electrocardiography: A Manifold Approach." In *Wearable and Implantable Body Sensor Networks (BSN), 2012 Ninth International Conference*, pp. 161–165, 2012.

[LXH13] Jason J. Liu, Wenyao Xu, Ming-Chun Huang, Nabil Alshurafa, and Majid Sarrafzadeh. "A Dense Pressure Sensitive Bedsheet Design for Unobtrusive Sleep Posture Monitoring." In *IEEE International Conference on Pervasive Computing and Communications*, Mar 2013.

[LY08] Wen-Hung Liao and Chien-Ming Yang. "Video-based activity and movement pattern analysis in overnight sleep studies." In *Pattern Recognition, 2008. ICPR 2008. 19th International Conference*, pp. 1–4, Dec. 2008.

[LYA09] Xi Long, Bin Yin, and R. Aarts. "Single-Accelerometer-Based Daily Physical Activity Classification." In *IEEE International conference on Engineering in Medicine and Biology Society*, pp. 6107–6110, Minneapolis, MN, USA, June 2009.

[LYC09] Changhong Liu, Yang Yang, and Yong Chen. "Human Action Recognition using Sparse Representation." In *IEEE International conference on Intelligent Computing and Intelligent Systems*, pp. 184–188, Beijiang, China, August 2009.

[LYK11] Choonghee Lee, Chiyul Yoon, H. Kong, Hee Chan Kim, and Youngwook Kim. "Heart Rate Tracking Using a Doppler Radar With the Reassigned Joint Time-Frequency Transform." *IEEE Antennas and Wirelss Propagation Letters*, **10**(5):1096–1099, May 2011.

[MLM09] W. Massagram, V. Lubecke, A. Madsen, and O. Boric-Lubecke. "Assessment of Heart Rate Variability and Respiratory Sinus Arrhythmia via Doppler Radar." *IEEE Transactions on Microwave Theory and Techniques*, **57**(10):2542–2549, October 2009.

[NAP03] B. Najafi, K. Aminian, A. Paraschiv, F. Loew, C. Bula, and P. Robert. "Ambulatory System for Human Motion Analysis using a Kinematic Sensor: Monitoring of Daily Physical Activity in the Elderly." *IEEE Transactions on Biomedical Engineering*, **50**(5):711–723, June 2003.

[Nat95a] B. Natarajan. "Sparse Approximate Solutions to Linear Systems." *SIAM Journal on Computing*, **24**(10):227–234, May 1995.

[Nat95b] B. K. Natarajan. "Sparse Approximate Solutions to Linear Systems." *SIAM J. Comput.*, **24**(2):227–234, April 1995.

[NAZ10] Hongbo Ni, Bessam Abdulrazak, Daqing Zhang, and Shu Wu. "Unobtrusive sleep posture detection for elder-care in smart home." In *Proceedings of the Aging friendly technology for health and independence, and 8th international conference on Smart homes and health telematics*, ICOST'10, pp. 67–75, 2010.

[NMT] K. Nakajima, Y. Matsumoto, and T. Tamura. "A monitor for posture changes and respiration in bed using real time image sequence analysis." In *Engineering in Medicine and Biology Society, 2000. Proc. 22nd IEEE*, volume 1, pp. 51–54.

[NMT01] Kazuki Nakajima, Yoshiaki Matsumoto, and Toshiyo Tamura. "Development of real-time image sequence analysis for evaluating posture change and respiratory rate of subject in bed." *Physiological Measurement*, **22**(3):N21, 2001.

[NW06] S.M. Nettina and Lippincott Williams & Wilkins. *The Lippincott Manual of Nursing Practice*. Lippincott Williams & Wilkins, 2006.

[Omr] Omron Inc. `http://www.omronhealthcare.com/`.

[OS06] Arie Oksenberg and Donald Silverberg. "The Effect of Body Posture on Sleep-Related Breathing Disorders: Facts and Therapeutic Implications." *Sleep Medicine Reviews*, **2**(3):139–162, 2006.

[Par09] James Parish. "Sleep-Related Problems in Common Medical Conditions." *Chest Journal*, **135**(2):563–572, 2009.

[PHR98] Thomas Perneger, Celiane Heliot, Anne-Claire Rae, Francois Borst, and Jean-Michel Gaspoz. "Hospital-acquired pressure ulcers: Risk factors and use of preventive devices." *Archives of Internal Medicine*, **158**(17):1940–1945, 1998.

[PLL07] B. Park, O. Lubecke, and V. Lubecke. "Arctangent Demodulation With DC Offset Compensation in Quadrature Doppler Radar Receiver Systems." *IEEE Transactions on Microwave Theory and Techniques*, **55**(5):1073–1079, May 2007.

[PPC11] Jaishanker Pillai, Vishal Patel, Rama Chellappa, and Nalini Ratha. "Secure and Robust Iris Recognition Using Random Projections and Sparse Representations." *IEEE Transactions on Pattern Analysis and Machine Intelligence (PAMI)*, **33**(8):1–14, October 2011.

[PT05] Sangho Park and M. Trivedi. "A Track-Based Human Movement Analysis and Privacy Protection System Adaptive to Environmental Contexts." In *IEEE conference on Advanced Video and Signal Based Verveillance*, pp. 171–176, Los Alamitos, CA, USA, September 2005.

[PYL07] B. Park, S. Yamada, and V. Lubecke. "Measurement Method for Imbalance Factors in Direct-Conversion Quadrature Radar Systems." *IEEE Microwave and Wirelss Components Letters*, **17**(5):403–405, May 2007.

[QB08] Muhannad Quwaider and Subir Biswas. "Body posture identification using hidden Markov model with a wearable sensor network." In *Proceedings of the ICST 3rd international conference on Body area networks*, BodyNets '08, pp. 19:1–19:8, 2008.

[Rab89] Lawrence R. Rabiner. "A tutorial on hidden markov models and selected applications in speech recognition." In *Proceedings of the IEEE*, pp. 257–286, 1989.

[RS89] G. Ramachandran and M. Singh. "Three-dimensional reconstruction of cardiac displacement patterns on the chest wall during the P, QRS, and T-segments of the ECG by laser speckle interferometry." *Medical Bioengineering Computing*, **27**(1):525–530, June 1989.

[RW06] C. Rasmussen and K. Williams. *Gaussian Processes for Machine Learning*. MIT Press, Cambridge, MA, USA, 2006.

[SA02] A. Sadeh and C. Acebo. "The Role of Actigraphy in Sleep Medicine." *Sleep Medicine Reviews*, **135**(2):217–226, 2002.

[SCH12] Zygmunt Szpak, Wojciech Chojnachi, and Anton Hegel. "Guaranteed Ellipse Fitting with the Sampson Distance." In *12th European Conference on Computer Vision*, pp. 18–23. Firenze, Italy, October 2012.

[SDH93] C M Shapiro, G M Devins, and M R Hussain. "ABC of sleep disorders. Sleep problems in patients with medical illness." *BMJ*, **306**(6891):1532–1535, 6 1993.

[SEH11] Qinfeng Shi, A. Eriksson, A. Van Den Hengel, and Chunhua Shen. "Is Face Recognition really a Compressive Sensing Problem?" In *IEEE International conference on Computer Vision and Pattern Recognition*, pp. 1063–6919, Colorado Spring, June 2011.

[SR03] Lawrence Saul and Sam Roweis. "Think globally, fit locally: unsupervised learning of low dimensional manifolds." *Journal of Machine Learning Research*, **4**:119–155, Dec. 2003.

[TH03] Yaqing Tao and Huosheng Hu. "Buiding a Visual Tracking System for Home-Based Rehabilitation." In *In Proceedings of the 9th Chinese Automation and Computing Society Conference In the UK*, pp. 343–348, 2003.

[Tha06] Michael Thase. "Depression and Sleep: Pathophysiology and Treatment." *Dialogues in Clinical Neurosciences*, **135**(2):217–226, 2006.

[TLW09] Y. Tao, J. Long, J. Wang, W. Cui, W. Ma, J. Huangfu, and L. Ran. "A Novel Non-contact Vital Sign Detection System Based on Phase-Coded Pulse Radar." In *IET Conference on Wireless Mobile and Computing*, pp. 421–424. Hangzhou, China, December 2009.

[TSL00] Joshua B. Tenenbaum, Vin de Silva, and John C. Langford. "A Global Geometric Framework for Nonlinear Dimensionality Reduction." **290**(5500):2319–2323, 2000.

[VAS11] Alireza Vahdatpour, Navid Amini, and Majid Sarrafzadeh. "On-body device localization for health and medical monitoring applications." In *PerCom*, pp. 37–44, San Deigo, CA, January 2011.

[Vis] VistaMedical. `http://www.pressuremapping.com`.

[Wor] World Health Organization. `http://www.who.int/topics/chronic_diseases/en/`.

[WWT05] K. Watanabe, T. Watanabe, H Tatanabe, H. Ando, and T. Ishikawa. "Noninvasive measurement of heartbeat, respiration, snoring and body movements of a subject in bed via a pneumatic method." *IEEE Transactions on Biomedical Engineering*, **52**(12):2100–2107, December 2005.

[WYG09a] J. Wright, Y. Yang, A. Ganesh, S. Sastry, and Y. Ma. "Robust Face Recognition via Sparse Representation." *IEEE Transactions on Pattern Recognition and Machine Intelligence*, **31**(2):210–227, Feb. 2009.

[WYG09b] John Wright, Allen Yang, Arvind Ganesh, Shankar Sastry, and Yi Ma. "Robust Face Recognition via Sparse Representation." *IEEE Transactions on Pattern Analysis and Machine Intelligence (PAMI)*, **31**(13):746–760, Febuary 2009.

[Xa13] Wenyao Xu and et al. "A Self-Calibrating Radar Sensor System for Measuring Vital Signs." In *IEEE Transactions on Biomedical Engineering*, TBME'13, 2013.

[XHA12] Wenyao Xu, Ming-Chun Huang, Navid Amini, Jason J. Liu, Lei He, and Majid Sarrafzadeh. "Smart insole: a wearable system for gait analysis." In *Proceedings of the 5th International Conference on PErvasive Technologies Related to Assistive Environments*, PETRA '12, pp. 18:1–18:4, 2012.

[XLH11] Wenyao Xu, Zhinan Li, Ming-Chun Huang, N. Amini, and M. Sarrafzadeh. "eCushion: An eTextile Device for Sitting Posture Monitoring." In *IEEE Conference on Body Sensor Networks (BSN)*, pp. 194–199, May 2011.

[Xse] Xsensor. `http://www.xsensor.com`.

[XZS12a] W. Xu, M. Zhang, A. Sawchuk, and M. Sarrafzadeh. "Robust Human Activity and Sensor Location Co-Recognition via Sparse Signal Representation." *IEEE Transactions on Biomedical Engineering*, **58**(11):1–10, Nov. 2012.

[XZS12b] Wenyao Xu, Mi Zhang, A.A. Sawchuk, and M. Sarrafzadeh. "Co-recognition of Human Activity and Sensor Location via Compressed Sensing in Wearable Body Sensor Networks." In *Wearable and Implantable Body Sensor Networks (BSN)*, pp. 124–129, May 2012.

[XZS12c] Wenyao Xu, Mi Zhang, Alexander Sawchuk, and Majid Sarrafzadeh. "Robust Human Activity and Sensor Location Co-Recognition via Sparse Signal Representation." In *IEEE Transactions on Biomedical Engineering*, TBME '12, pp. 3169–3176, 2012.

[XZS12d] Wenyao Xu, Mi Zhang, Alexander A. Sawchuk, and Majid Sarrafzadeh. "Co-Recognition of Human Activity and Sensor Location via Compressed Sensing in Wearable Body Sensor Networks." In *IEEE International conference on Wearable and Implantable Body Sensor Networks (BSN)*, pp. 124–129, London, UK, May 2012.

[YAY05] M. Yoshioka, M Ayabe, T. Yahiro, H. Higuchi, Y Higaki, J Amand, H. Miyazaki, Y. Yoshitake, M. Shindo, and H. Tanaka. "Long-period accelerometer monitoring shows the role of physical activity in overweight and obesity." *International Journal of Obesity*, **29**(11):502–508, June 2005.

[YJS09] Allen Yang, Roozbeh Jafari, Shankar Sastry, and Ruzena Bajcsy. "Distributed Recognition of Human Actions Using Wearable Motion Sensor Networks." *Journal of Ambient Intelligence and Smart Environments*, **1**(2):103–115, June 2009.

[YOF11] R. Yousefi, S. Ostadabbas, M. Faezipour, M. Farshbaf, M. Nourani, L. Tamil, and M. Pompeo. "Bed posture classification for pressure ulcer prevention." In *Engineering in Medicine and Biology Society*, pp. 7175–7178, Sept. 2011.

[ZFP05] Z. Zhu, J. Fei, and I. Pavlidis. "Tracking Humane Breath in Infrared Imaging." In *IEEE Symposium on Bioinformatics and Bioengineering*, pp. 227–231. Washington DC, July 2005.

[ZH05] Z. Zhu and X. Huang. "Bias Analysis of A Gain/Phase/DC-offset Estimation Technique for Direct Frequency Conversion Modulators." In *IEEE International Conference on Acoustics, Speech, Signal Processing*, pp. 18–23. Ottawa, Canada, March 2005.

[ZH08] Huiyu Zhou and Huosheng Hu. "Human motion tracking for rehabilitation - A survey." *Biomedical Signal Proc. and Control*, **3**:1–18, 2008.

[ZRV12] M. Zakrzewski, H. Raittinen, and J. Vanhala. "Comparison of Center Estimation Algorithms for Heart and Respiration Monitoring With Microwave Doppler Radar." *IEEE Sensors Journal*, **12**(3):627–634, March 2012.

[ZS11a] Mi Zhang and A.A. Sawchuk. "Manifold Learning and Recognition of Human Activity Using Body-Area Sensors." In *Machine Learning and Applications and Workshops (ICMLA), 10th International Conference*, volume 2, pp. 7–13, Dec. 2011.

[ZS11b] Mi Zhang and Alexander A. Sawchuk. "A Feature Selection-Based Framework for Human Activity Recognition Using Wearable Multimodal Sensors." In *International Conference on Body Area Networks (BodyNets)*, pp. 1–7, Beijing, China, November 2011.

[ZS12] Mi Zhang and Alexander A. Sawchuk. "Motion Primitive-Based Human Activity Recognition Using a Bag-of-Features Approach." In *ACM SIGHIT International Health Informatics Symposium (IHI)*, pp. 1–10, Miami, Florida, USA, January 2012.